THE TECTONIC EVOLUTION OF THE CAPE FOLD BELT:

CONSTRAINTS FROM FLUID INCLUSION CHARACTERISTICS IN SYNTECTONIC QUARTZ VEINS

A thesis submitted in fulfilment of the requirements for the degree of

MASTER OF SCIENCE

at
RHODES UNIVERSITY
Grahamstown

By BRIONY PROCTOR
March 2017

Supervised by PROFESSOR S. H. BÜTTNER

Department of Geology, Rhodes University, Grahamstown, South Africa

TABLE OF CONTENTS

ACKNOWLEDGEMENTS

Thank you to the Mining Qualifications Authority for providing funds for my studies. I am also very grateful to the Rhodes University Research Council for the grants which provided funding for analytical work. Thank you to Professors Arnold Gucsik and Axel Hoffman for their direction and the use of the University of Johannesburg Raman spectroscopy lab.

Thank you to all my fellow staff and researchers at Rhodes University Geology Department, all of whom contributed to this project in some small way.

Specifically, thank you to Professor Steve Prevec for your guidance and encouragement, and for allowing me the opportunity to work for the geology department. Thank you to Wesson Reid for sharing your knowledge and allowing me to learn from your mistakes. Thank you to John Hepple, Andrea King, and the technical team for time spent on sample preparation.

Thank you to Bantu Nstaluba for being the voice of reason when I lost my way.

Most importantly, thank you to my supervisor, Professor Steffen Büttner, for your invaluable guidance and never-ending patience. Thank you for always pushing me to achieve, and seeing my potential even when I couldn't see it myself.

Finally, thank you to my mom, Kathy, my dad, Rick, my sister, Laura, and my brother-in-law Alex. Your unconditional love and support means the world to me. I am so grateful.

ABSTRACT

Syn-tectonic quartz veins formed along faults, folds and tension gashes in rocks of the Cape Supergroup (CSG) of the central Cape Fold Belt (CFB) comprise mainly hydrous saline fluids. These veins may also contain CO_2, or CH_4 and CO_2, or neither CO_2 nor CH_4. The majority of inclusions are two-phase and fluid rich, and the most common fluid composition is H_2O-NaCl. The final melting temperature, and therefore salinity, differs very little across different structures (fluids in all structures show maximum salinities between 2.5 and 6 wt% NaCl equivalent).

Thrusts, reverse faults, strike- and oblique-slip faults, and folds all have similar homogenization temperatures (T_h). Primary H2O-NaCl inclusions show T_h between ~130 and 200 °C, and H2O-NaCl-CO2 inclusions have slightly higher T_h, between ~140 and 240 °C. Secondary inclusions in all structures have a similar T_h range to primary inclusions, but have a lower maximum T_h (~130-180 °C). Inclusions containing CH_4 have the highest T_h (~210 – 300 °C).

Microthermobarometry indicates that fluids associated with contractional structures, such as thrust faults or folds, from the Ordovician lower Table Mountain Group (TMG) show lower greenschist facies trapping conditions (~170-175 MPa and ~240-300 °C). These veins also show a plastic deformation overprint (recrystallization of quartz and foam textures), at temperatures higher than the trapping conditions (~ ≥300 °C), indicating that temperatures increased subsequent to hydraulic fracturing, quartz precipitation and thrust slip. These structures formed on a prograde path, at approximately 335 Ma, at a time when the overlying CSG rock column was approximately 6800 m thick. This event pre-dated the thermal peak of the Cape Orogeny at ~276-261 Ma by ~60 million years.

Further up in the stratigraphy of the CFB, in the Devonian upper Bokkeveld Group, fluid inclusions in quartz veins associated with a thrust fault show similar trapping pressure (~200 MPa) to the structures in the lower CFB. At 335 Ma, the stratigraphic overburden on this sample locality would not have been sufficiently thick to exert the calculated pressure. This fault may have formed at a later time. The observed pressure of ~200 MPa may have been created either by the higher Bokkeveld Group, the entire Witteberg Group, and further CSG rocks that were eroded prior to the deposition of the Permo-Triassic Karoo Supergroup, or by tectonic thickening of the CSG by prograde thrusting.

Still further up in the CSG, fluids from a fold sample from the Witteberg Group record quartz precipitation at lower greenschist facies conditions and subsequent plastic deformation during folding. The formation of this fold postdates the thrusting in the lower TMG, and may correlate in time with deformation during the thermal peak in Middle Permian time (~276-261 Ma).

LIST OF RELEVANT TERMS

1. **Fluid inclusion (FI)**: A defect structure in a crystal, containing entrapped solid, liquid and/or gas phases (Mumm, 2008).

2. **Microthermometry**: A non-destructive technique of observing various phase changes in fluid inclusions under controlled heating (Roedder, 1984). The instrument used in this study is the "heating – cooling stage", attached to a microscope.

3. **Primary inclusion**: An inclusion that was trapped while the host crystal was still growing (Diamond, 2003).

4. **Secondary inclusion**: A fluid inclusion that has been trapped subsequent to any growth of the host crystal, typically located within healed fractures that intersect crystal boundaries (Diamond, 2003).

5. **Pseudosecondary inclusion:** A fluid inclusion that was trapped after an early phase of host crystal growth had finished, but before all crystal growth was completed (Diamond, 2003).

6. **Fluid Inclusion Assemblage (FIA):** A group of cogenetic fluid inclusions within one petrographic feature (e.g. a healed fracture or crystal growth horizon) (Diamond, 2003).

7. **Secondary Assemblage (SA):** A group of cogenetic secondary fluid inclusions within one petrographic feature.

8. **Homogeneous entrapment**: The formation of fluid inclusions from a one-phase parent fluid (Diamond, 2003).

9. **Heterogeneous entrapment**: The formation of fluid inclusions from a multi-phase state (Diamond, 2003).

10. **Temperature of homogenization (T_h)**: The temperature at which total homogenization of the inclusion occurs, and only one phase is present.

11. **Temperature of trapping (T_t):** The temperature of formation of the inclusion. If no pressure correction is needed, then $T_t=T_h$ (Roedder, 1984).

12. **Temperature of initial melting (T_i)**: The temperature at which a liquid first appears during heating of a solid-bearing fluid inclusion (Diamond, 2003).

13. **Temperature of final melting (T_m):** The temperature at which a solid completely melts on heating of a fluid inclusion (Diamond, 2003).

14. **Temperature of nucleation (T_n)**: The temperature at which a phase first appears in an inclusion. This generally refers to nucleation on cooling, such as the formation of a bubble in a previously homogenised liquid-vapour inclusion (Roedder, 1984), or where initial ice or clathrate forms on cooling (Mumm, 2008).

1. INTRODUCTION

1.1 Aim of the study

Irrespective of numerous studies investigating the structures and the structural relationships in the Cape Fold Belt (CFB), the tectonic setting and evolution of the Cape Orogen remains a matter of controversial debate (e.g. Booth, 2011). Previous work has focused on deformation styles and metamorphism of the rocks of the CFB, and recent work by Hansma et al. (2016) has provided further constraints on the timing of deformation. Few studies exist that have investigated the physical conditions of deformation in the CFB (e.g. Fagareng, 2012). However, beyond the finding of maximum deformation temperatures not exceeding the greenschist facies (Frimmel et al., 2001), the physical-chemical conditions at which the various deformation episodes in the CFB have taken place are largely unknown.

Fractures in rocks can act as fluid conduits, and can be filled with precipitated minerals in which samples of the fluid can be trapped as fluid inclusions (Parry, 1998). Measurements of the temperatures at which phase changes occur in such fluid inclusions can provide constraints on the conditions of formation of that particular fracture. If that fracture can be associated with a specific structure, such as a fold or fault, then the conditions of formation of that structure can be inferred. In this study this relationship has been applied to identify the conditions of formation of hydraulic fractures and faults, all of which contain synkinematic vein quartz rich in fluid inclusions.

This study aims at contributing to the better understanding of the deformation conditions of some structure types in the CFB. The investigated structures contain vein quartz that can be associated with the formation of specific structures, such as tension gashes, thrust faults, strike-slip faults and, to a lesser extent, fold structures. Fluid inclusions captured during the growth of syngenetic quartz record the physical and chemical characteristics of the fluid present at the time. Accordingly, fluid inclusion analysis from quartz veins can contribute to the reconstruction of the tectonic history of the Cape Orogen. Fluid inclusion petrography, analysis of the physical characteristics using a heating-cooling stage, and compositional fluids analysis by Raman spectrometry gives insight to the association of specific fluids with specific structures in the CFB. Some fluid types are advantageous in the determination of deformation conditions in terms of pressure and temperature.

This study presents results from quartz veins collected from four roughly north-south transects throughout the Southern CFB. Twenty-four samples were taken from road cuttings along the Outeniqua Pass, Meiringspoort, the Swartberg Pass, and a transect between de Vlugt and Uniondale (Figure 2.1). From these, syntectonic quartz veins from nineteen faults, one fold and four tension gashes were selected for detailed fluid inclusion analysis. The data suggest that vein formation in all these different structures, and hence the related tectonic activity in the central CFB, formed in a narrow temperature range within the lower greenschist facies.

1.2 Geological setting of the Cape Fold Belt and context of the study

The CFB is a series of folds and thrusts stretching about 1300 km along the South African coast (Frimmel et al., 2001), which affected the formations of the Cape Supergroup. At around 275 million years ago (Newton et al., 2006), the development of a subduction zone along the

southern margin of Gondwana led to contraction of the interior, resulting in the folding and faulting of the Cape Supergroup rocks. The CFB forms part of a Gondwanide orogen that can be traced across South America, Africa, Antarctica and eastern Australia (Figure 1.1; Thomas et al., 1993).

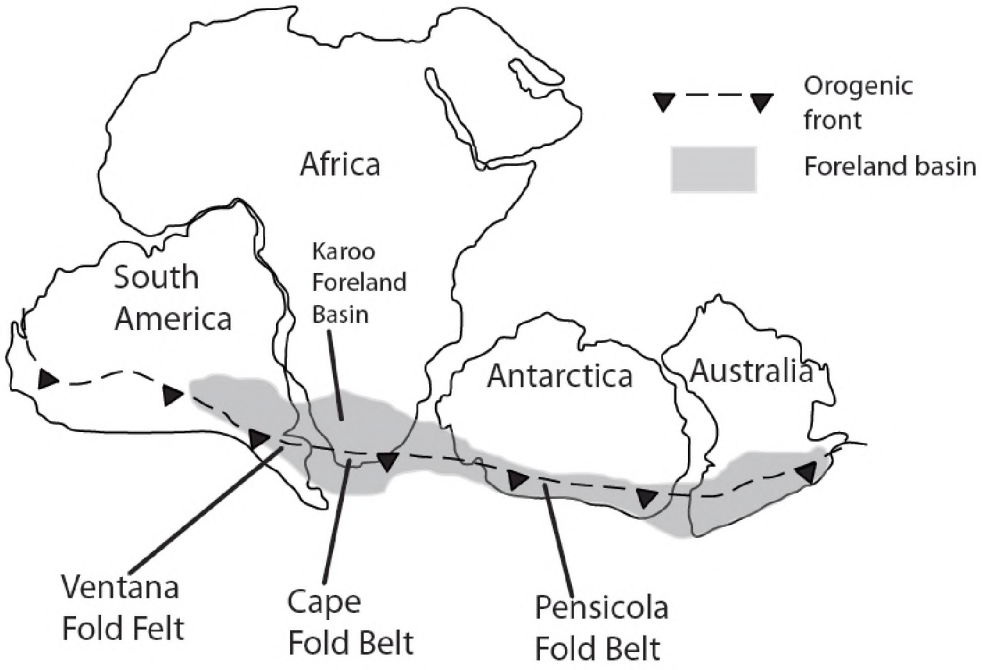

***Figure 1.1**: The Cape Fold Belt in context of the Gondwanide orogen, which can be traced across South America, Africa, Antarctica and Australia (modified after Frimmel et al., 2001).*

1.2.1 Stratigraphy

The Cape Supergroup is divided into three lithologically distinct groups: the sandstone dominated Table Mountain Group; the argillaceous Bokkeveld Group; and the interlayered quartz sandstones and mudstones of the Witteberg Group (Thamm & Johnson, 2006). The undeformed thickness of the Cape Supergroup is unknown, but it is estimated to represent about 8 to 10 km of stratigraphy (Thamm & Johnson, 2006).

The Ordovician to Early Devonian Table Mountain Group was deposited in shallow marine and fluvial environments, and the sediments reach up to ~4500 m in thickness (Thamm & Johnson, 2006). The Devonian Bokkeveld Group, reaching up to ~3000 m, consists of alternating fine-grained sandstone and mudrock units (Thamm & Johnson, 2006). Bokkeveld sediments were deposited in deltaic and shallow marine environments, and contain marine invertebrate fossils (Thamm & Johnson, 2006). The Late Devonian to Early Carboniferous Witteberg Group is up to ~1700 m thick, and consists of quartzitic sandstone and micaceous mudstone, deposited in shallow marine and deltaic depositional environments (Thamm & Johnson, 2006).

The Cape Supergroup unconformably overlies a Neoproterozoic-Cambrian metasedimentary and granitic basement (Tankard et al., 1982) that was formed and consolidated during the Pan-African orogeny. Erosion formed a near-sea level, moderate relief before the earliest, shallow-

marine sediments of the Cape Supergroup were deposited (Lock, 1978). This basement consists of the Kaaimans, Malmesbury, Kango and Gamtoos Groups, and intrusions of the Cape Granite Suite (Frimmel et al., 2001). Exposure of pre-Cape rocks in the Cape Fold Belt is restricted to three fault-bound inliers – the Kango and Gamtoos inliers, and the Kaaimans horst (Thomas et al., 1993).

Overlying the Cape Supergroup are sedimentary rocks of the southern margin of the Karoo Supergroup, ranging in age from Late Carboniferous to Middle Jurassic (Johnson et al., 2006). The Cape Fold Belt formed while deposition of the upper two groups of the Karoo Supergroup was still taking place, whereas the lower units of the Karoo Supergroup have been intensely deformed as a result of the Cape Orogeny (Johnson et al., 2006).

1.2.2 Regional structures in the Cape Fold Belt

Three domains are distinguished in the CFB, based on structural grain, fold style and the amount of shortening (Hälbich et al., 1983): The north-south trending Western Cape Fold Belt and the east-west trending Southern Cape Fold Belt meet at the syntaxis in the south-west Cape (De Beer, 1992). Deformation is strongest in the southern branch (Shone & Booth, 2005), where the fold geometries generally have higher amplitudes and shorter wavelengths (Hansma et al., 2016). Deformation in the western branch is less severe (Shone & Booth, 2005).

The structural style is also partly related to differing mechanical strengths of the strata (Tankard et al., 2009). The Table Mountain quartz sandstones are strongest, and tend to form large folds, while the sandstone-shale lithologies of the Bokkeveld and Witteberg Groups form smaller, first order folds (Tankard et al., 2009).

Abundant evidence, such as folding of quartz-dominated rocks, indicates that the deformation conditions in the Cape Orogeny exceeded the minimum of plastic deformation and recrystallization in quartz, which points to at least lower greenschist facies deformation conditions (Voll, 1976). On the other hand, the lack of metamorphic rocks and minerals indicating amphibolite facies metamorphism places the possible deformation conditions into the greenschist facies or, as far as the brittle features in the Cape Orogen are concerned, below.

1.2.2.1 Folds

Folding is the most prominent form of deformation in the CFB. Fairly open, north-verging folds are the most common (Newton et al., 2006), but different fold styles are discernible in each domain. The western branch is characterised by northwest to north-trending gentle, open folds which fade out toward the east (Shone & Booth, 2005).

Within the more strongly deformed Southern CFB, there are a further two structural domains: a northern domain dominated by northward verging and asymmetric folds; and a southern domain comprised of two regional-scale, anticlinal box folds (Paton et al., 2006). Folds plunge at shallow angles both to the east and west (Newton et al., 2006). Disharmonic folding, where intensely folded strata is over- or underlain by less intensely folded strata, is common in the Southern CFB (Newton et al., 2006).

The syntaxis region is characterised by abundant short wavelength and low amplitude folds (Paton et al., 2006). Folds of the western and southern branches merge relatively smoothly with the north – east trending syntaxial folds (De Beer, 1995). The northwest- to north-trending folds of the western branch bend to a north – south orientation near the syntaxis (Newton et al., 2006). Similarly, the east – west trending folds of the southern branch are bent south-west in the syntaxis area (Newton et al., 2006).

1.2.2.2 Faults

In the southern branch, the dominance of south-dipping thrusts indicate that thrusting probably occurred in response to approximately north-south crustal contraction (Newton et al., 2006). Closely-spaced thrusts are characteristic of the southern branch, and individual thrust displacement is difficult to identify (Shone & Booth, 2005).

Thrusts often exploit pre-existing zones of weakness, so individual thrusts often occur parallel to bedding or exploit suitably oriented cleavage planes (Shone & Booth, 2005). Often, shale units are eclipsed by thrust faults, so that shales that were formerly interbedded with quartzites have been tectonically reduced in thickness or even eliminated from the stratigraphy along thrust surfaces (Shone & Booth, 2005).

Both branches of the CFB are cut by numerous post-tectonic normal faults (De Beer, 1995). Most strike east-west, and most dip towards the south (Shone & Booth, 2005). Normal faults transect all earlier faults and folds (Booth & Shone, 2002), and most of the normal faults have a small strike-slip component (Shone & Booth, 2005). Some normal faults appear to be reactivated former thrust ramps, in which planes of weakness were exploited when compressive stresses were replaced by tensional stresses during the breakup of Gondwana (Newton et al., 2006).

Fault filling is mostly quartz veins, along which slickensides are common (Booth & Shone, 2002). In fact, faults are recognised in the field mainly by the presence of quartz veins (Booth et al., 2004), but there are many non-hydraulic faults as well.

1.2.2.3 Relationship between folding and faulting

Sequential relationships between thrusting and folding are not always clear (Booth & Shone, 2002). In various studies, sequences of thrusting before faulting (de Wit et al., 1998, cited in Booth & Shone, 2002, p. 187), simultaneous thrusting and faulting (Booth, 1996, cited in Booth & Shone, 2002, p. 187), and thrusting after faulting (Booth & Shone, 1992, cited in Booth & Shone, 2002), have been recognised. Nevertheless, it is certain that in the eastern CFB, some thrusts are closely associated with folding, and back-thrusting and fore-thrusting are closely related to each other in their genesis and probably also in time (Booth, 1996; Booth & Shone, 1999). Normal faults are related to the late Mesozoic breakup of Gondwana (~190 to 90 Ma; Watkeys, 2006), and therefore transect all earlier faults and folds (Booth & Shone, 2002).

1.2.3 Absolute timing of events

Very few studies have been done to provide ages for tectonic events during the deformation of the Cape Supergroup. The earliest data comes from a study by Hälbich et al. (1983), in which six pulses of deformation were identified between 300 Ma and 215 Ma. These ages are based on $^{40}Ar/^{39}Ar$ ages of white mica. More recently, Hansma et al. (2016) challenge these data, and argue for two episodes of muscovite growth during the Cape Orogeny, based on $^{40}Ar/^{39}Ar$ age constraints: An older cluster of samples from the north CFB give an age of 261 ± 3 to 276 ± 5 Ma, which is interpreted as the main deformation event. A younger group in the southernmost, highest grade CFB may indicate cooling of exhumed rocks, or a second, younger deformation episode at 248 ± 2 to 254.6 ± 2.1 Ma. This period of deformation (~30 Ma) is much shorter than the ~85 million years proposed by Hälbich et al. (1983).

2. METHODS

2.1 Sampling and field work

Twenty-nine sampling sites were chosen from four, roughly north-south transects across the Southern Cape Fold Belt (Figure 2.1). Thirty-seven samples of quartz veins were collected from twenty-nine road cuttings along the Swartberg Pass, the Meiringspoort Pass, the Outeniqua Pass, and a section between De Vlugt and Uniondale.

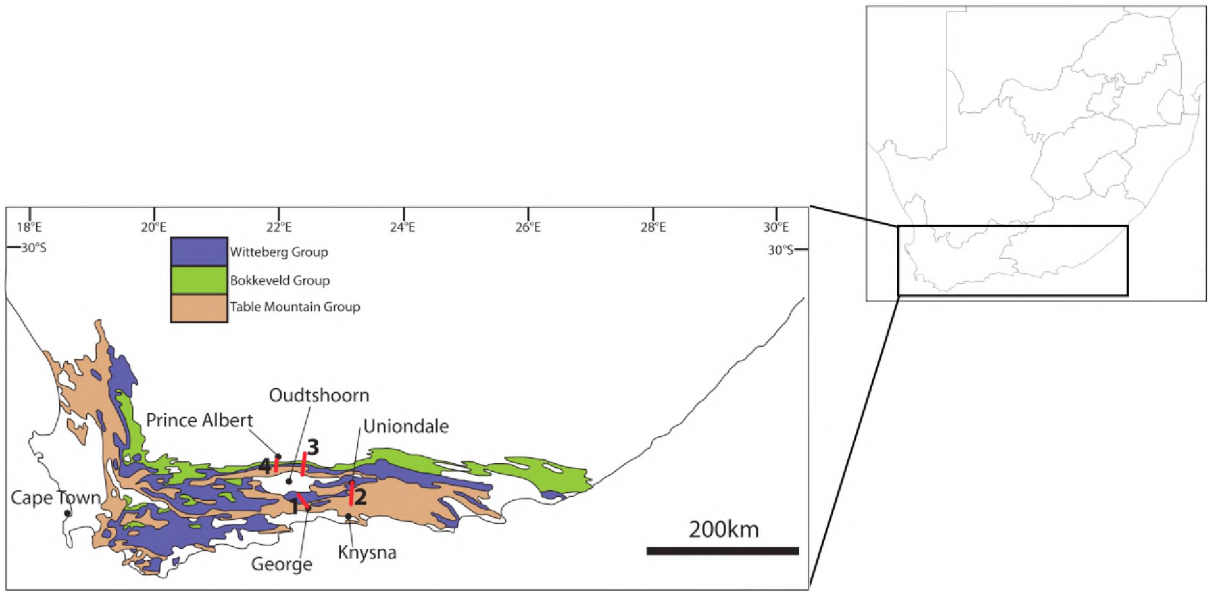

***Figure 2.1**: Locations of the four transects which were sampled for this study:*
1. Outeniqua Pass transect; samples P1 to P7
2. de Vlugt – Uniondale transect; samples P8 to P17
3. Meiringspoort transect; samples P18 to P25
4. Swartberg Pass transect; samples P26 to P29
(modified after Thamm and Johnson, 2006)

Samples were selected from locations where quartz veins could easily be associated with a specific deformation structure. Macroscopic observations were done to classify the type of structure – fault, fold or tension gash – and in the case of faults and folds, lineations and slickenside steps were used to determine the sense of movement. In total, thirty-seven quartz vein samples were collected.

2.2 Sample preparation

Doubly polished thick sections (wafers) were prepared for microthermometry on all quartz vein samples. Each wafer was approximately 150 μm thick. A representative selection of samples was also chosen to prepare thin sections (~30 μm) for petrographic studies.

2.3 Quartz petrography and fluid inclusion mapping

Through petrographic studies on thin sections and doubly polished wafers, fluid inclusions were mapped in twenty-four of the thirty-seven collected samples. Thin section petrography was done to investigate microfabrics of the vein quartz. Of particular interest was establishing different generations of quartz crystal growth. Thin section petrography was done on a Leica petrographic microscope, mounted with a Leica EC3 camera. Leica LAS EZ imaging software was used to capture photomicrographs.

Petrography on doubly polished wafers was done to identify fluid inclusion assemblages (FIAs): groups of inclusions which are all related to one petrographic feature. The inclusion assemblages were then characterised as primary, pseudosecondary or secondary, as defined by Roedder (1984), and the phases present in the fluid inclusions was identified by sight.

Also noted for each inclusion were the inclusion size (the largest dimension of the inclusion, ignoring any thin or irregular extensions), shape (Figure 2.2) and percentage volume of phases present.

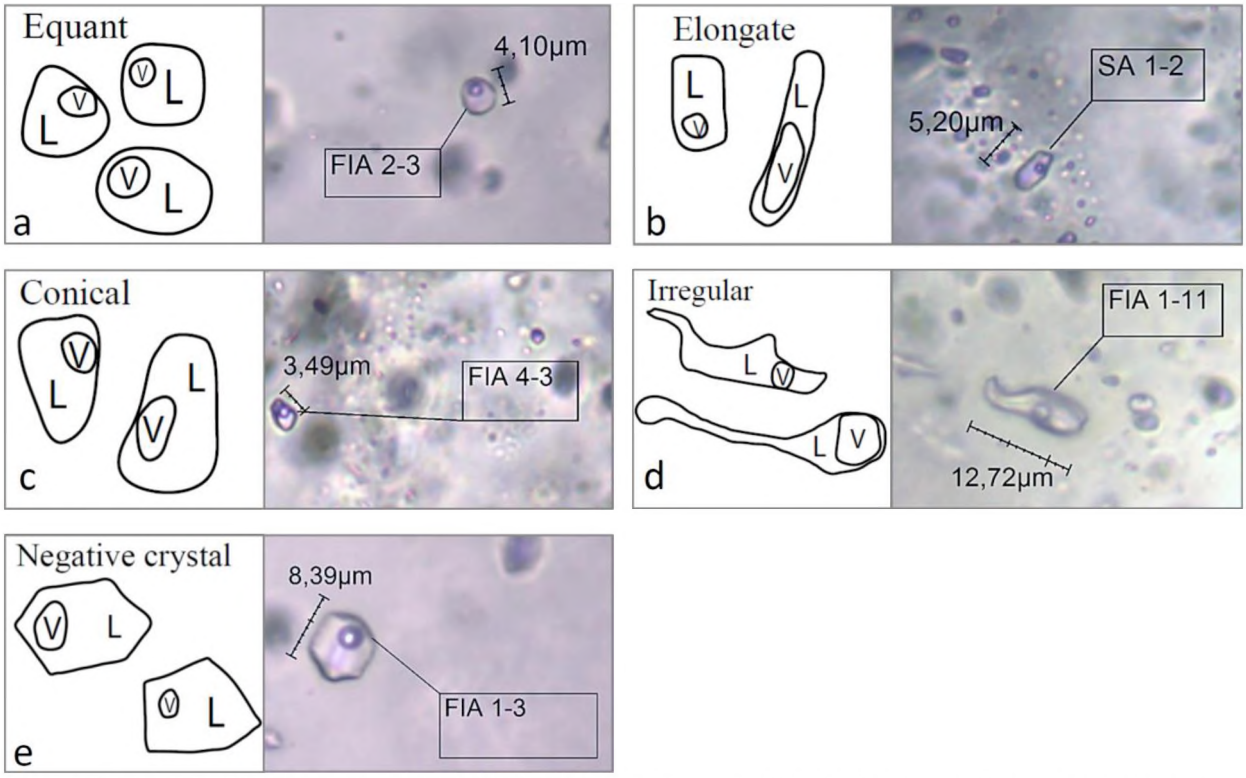

***Figure 2.2**: While FI shape varies widely, FI's can all be broadly classified as one of five shapes: Equant, elongate, conical, irregular and negative crystal. Here, basic outlines of the different shapes are shown, ('L' and 'V' refer to liquid and vapour respectively), as well as examples of FI shapes from the current study. They are: a) Equant; example from fluid inclusion assemblage 2 (FIA 2) in sample P20A. b) Elongate; example from secondary assemblage 1 (SA 1) in sampleP20A. c) Conical; example from FIA 4 in sample P23B. d) Irregular; example from FIA 1 in sample P23A. e) Negative crystal (controlled by crystallography of host mineral); example from FIA 1, sample P20A.*

2.4 Microthermometry

Physical characteristics of selected fluid inclusions in quartz veins were analysed during heating and cooling runs on doubly polished wafers using a Linkam THMSG 600 temperature controlled geology stage, using an LNP cooler and a TMS 93 temperature controller. Observation of inclusions during heating and cooling was done through a Nikon Eclipse E600 microscope which was fixed to the Linkam stage and equipped with objective lenses of 4x, 20x, 50x and 100x magnification. The microscope was fitted with a Nikon TV lens C-0,45X camera, through which onscreen monitoring and photomicrographs could be managed using DeltaPix Insight camera software.

The heating stage is fitted with an electric element, which allowed for the heating of samples at a pre-programmed rate, up to 600 °C (although in this study is was not necessary to go above 300 °C). Synthetic quartz wafer standards for melting point and homogenisation temperature ranges of <0 °C and >25 °C were used to calibrate the stage. Readings are reproducible up to ±0.5 °C or less.

The physical characteristics of interest were the initial melting temperature (T_i), final melting temperature (T_m), and temperature of homogenisation (T_h). A typical cooling-heating run involves cooling the selected inclusion to -180 °C, then heating to observe T_i and T_m, at a rate of 2 °C/min over the T_i and T_m ranges. Heating above 25 °C is set at a rate of 10 °C/min up to ~100 °C. Thereafter the inclusion is heated at a rate of 5 °C per minute to record T_h at an accuracy of ±0.5 °C. Using the results from microthermometry, the salinity of H_2O-NaCl fluid inclusions was calculated as described by Bodnar (1993).

2.5 Raman Spectroscopy

The chemistry of fluid inclusions was analysed using a WITec alpha300R confocal laser Raman microscope at the Geology Department at University of Johannesburg. Raman spectral measurements were done with a non-polarised argon-ion laser. The spectra were captured by Nikon objective lenses using 50x and 100x magnification. Raman spectra calibration was done using a silicon standard. Accumulation was 10 at 2 second intervals.

Compounds of interest are H_2O, CO_2 and CH_4. Only analyses that show a well-developed peak at 1285, 1388 or 1370 cm^{-1} are interpreted to contain CO_2. Spectra showing broad, poorly defined peaks at those wavelengths were interpreted as containing no or only insignificant amounts of CO_2.

3. Field observations

Sampling was done along four roughly north-south trending transects across the southern Cape Fold Belt (Figure 3.1). Twenty-nine sampling sites (Figure 3.2) were chosen in locations where quartz veins could be associated with a specific deformation feature. A summary of all analysed samples and the structures to which they are related is given in Appendix E.

In this chapter, I will describe the macroscopic observations which provided the basis for the classification of the structure as a fault, fold or tension gash. Where applicable, the quartz veins are described as either coherent – a distinct vein that has not been broken up and is continuous for some length along the structure to which it is related – or as disrupted, a vein which is fragmented, but fragments can be associated with each other along the structure to which the vein is related.

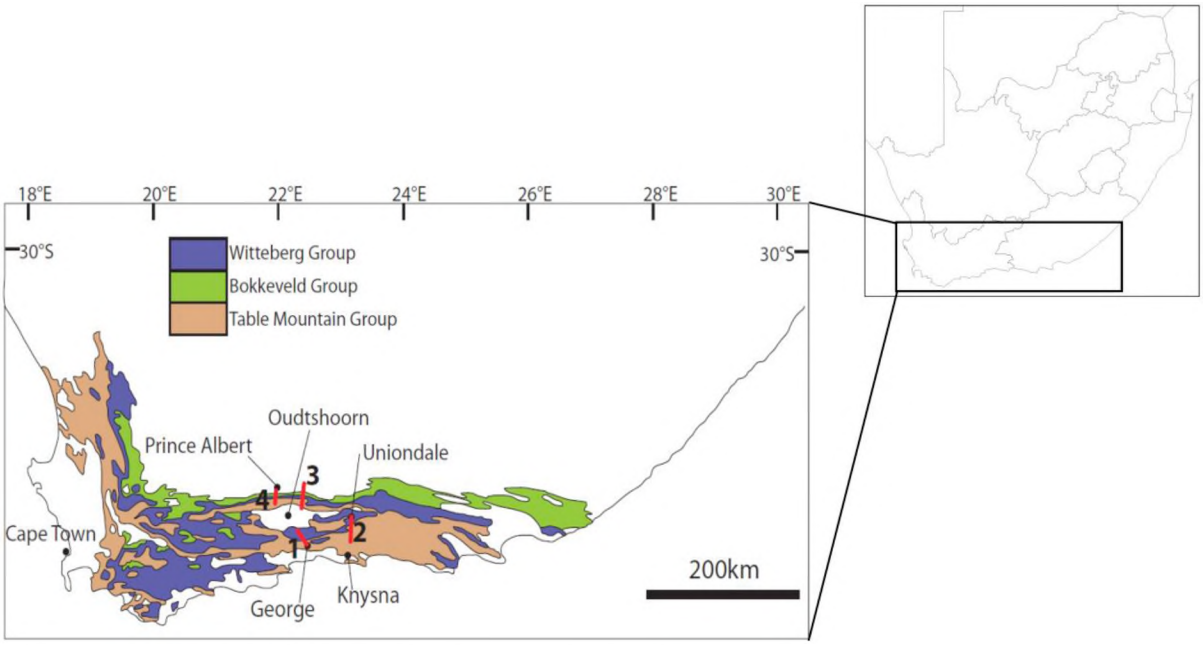

***Figure 3.1**: Locations of the four transects which were sampled for this study:*
1. Outeniqua Pass transect; samples P1 to P7
2. de Vlugt – Uniondale transect; samples P8 to P17
3. Meiringspoort transect; samples P18 to P25
4. Swartberg Pass transect; samples P26 to P29
(modified after Thamm and Johnson, 2006)

3.1 Outeniqua Pass and Montague Pass – Samples P1-P7

Along the Outeniqua Pass, rocks of the Table Mountain Group (TMG) (Figure 3.2) are exposed. They are primarily massive, poorly layered, light grey quartzitic sandstones with minor interbedded shale. With the exception of sample P5, which was taken from the Tchando Formation, the samples from this profile come from the Peninsula Formation – a thrust-fault-stacked quartzite package (Figure 3.3).

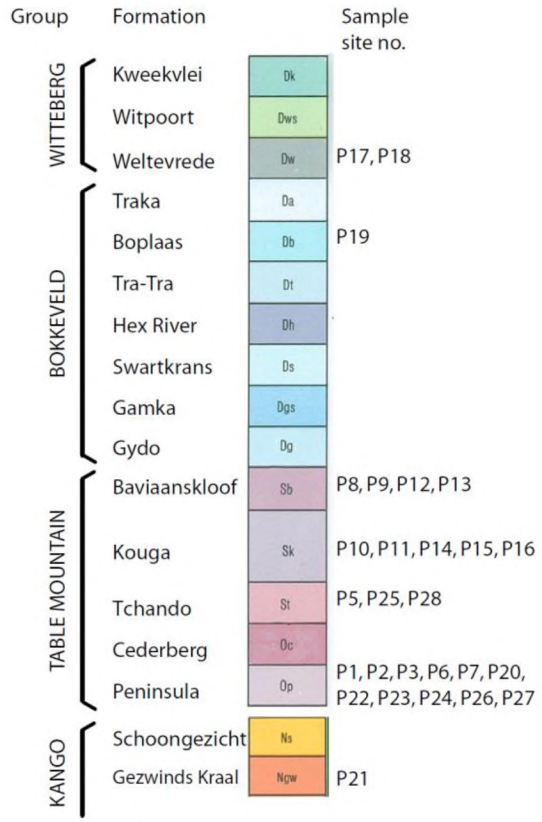

***Figure 3.2**: Stratigraphic profile of the formations within the Cape Supergroup and the uppermost formations of the Kango Inlier, showing the sample sites from each formation (modified after Council for Geoscience, 1979).*

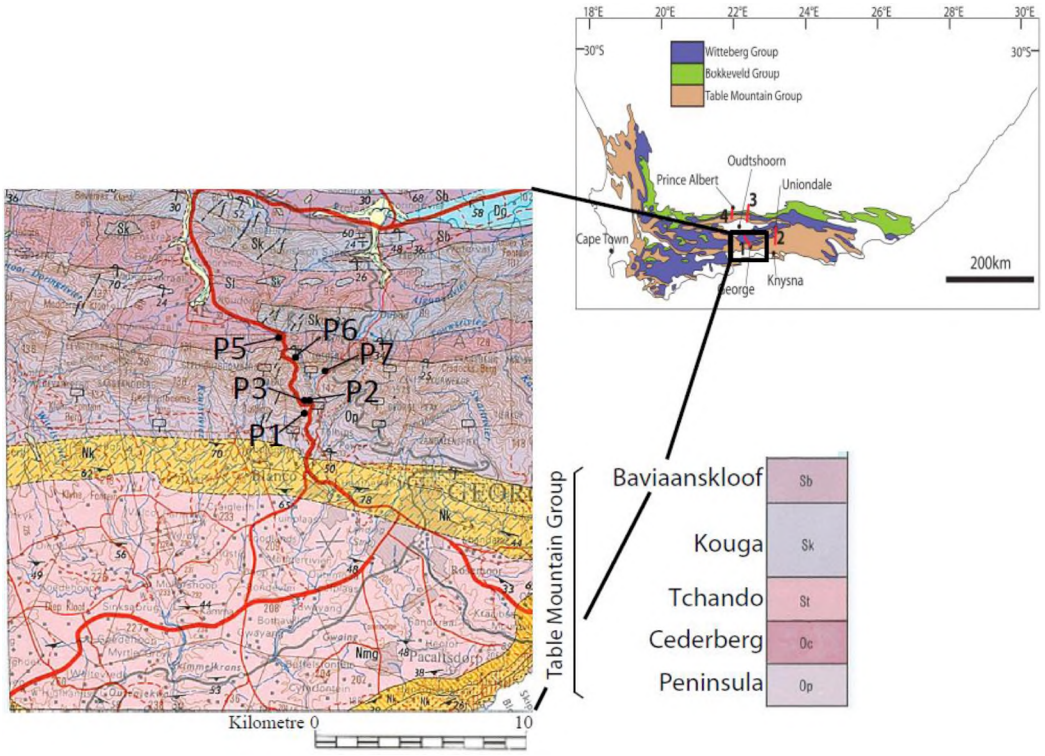

***Figure 3.3**: Locations of sample sites P1-P7 along the Outeniqua Pass transect. All samples apart from P5 are from rocks of the Peninsula Formation, the lowermost formation of the Table Mountain Group. Sample P5 is from the Tchando Formation (modified after Council for Geoscience, 1979).*

Samples P1, P2, P3, and P6 are vein quartz samples from thrust faults in road cuttings where quartz veins are abundant. The veins, all approximately 5-10 cm thick, occur in shallowly south to south-west dipping fault zones (~198/40). Quartz fibres (174/38 to 232/30) in conjunction with SC fabrics and slickenside steps indicate top-north to north-east displacement (Figure 3.4).

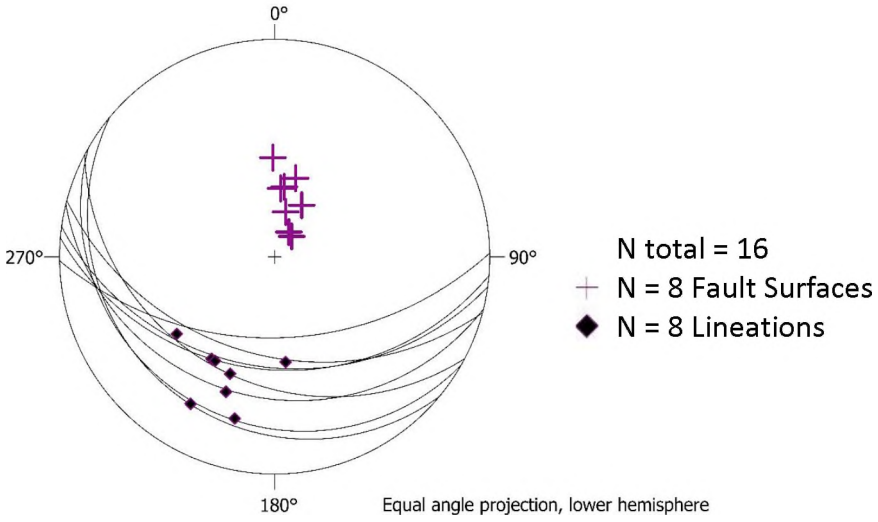

***Figure 3.4**: Sample sites P1-P3 and P6 were all at fault zones along the Outeniqua Pass. The fault planes have a consistent shallow south to south-west dip. The presence of shear sense indicators at sample sites P1, P2, P3 and P6 indicate top N-NE movement.*

Three samples were taken at sample site P5, a 10-20 cm thick shear zone. A thrust fault (188/36) developed approximately parallel to bedding along a shale layer, and fibrelines (210/32) and SC fabrics indicate top-north-east movement. Sample P5A is from a small, symmetrically folded vein with an amplitude of ~10 cm that is located adjacent to the shear zone. The folds are tight, and the axial surfaces of the folds are orientated approximately parallel to the shear zone. The fold is disrupted, but hinge zones are clearly visible (Figure 3.5). Sample P5B is from an en-echelon tension gash, and P5C is from vein quartz in the thrust fault.

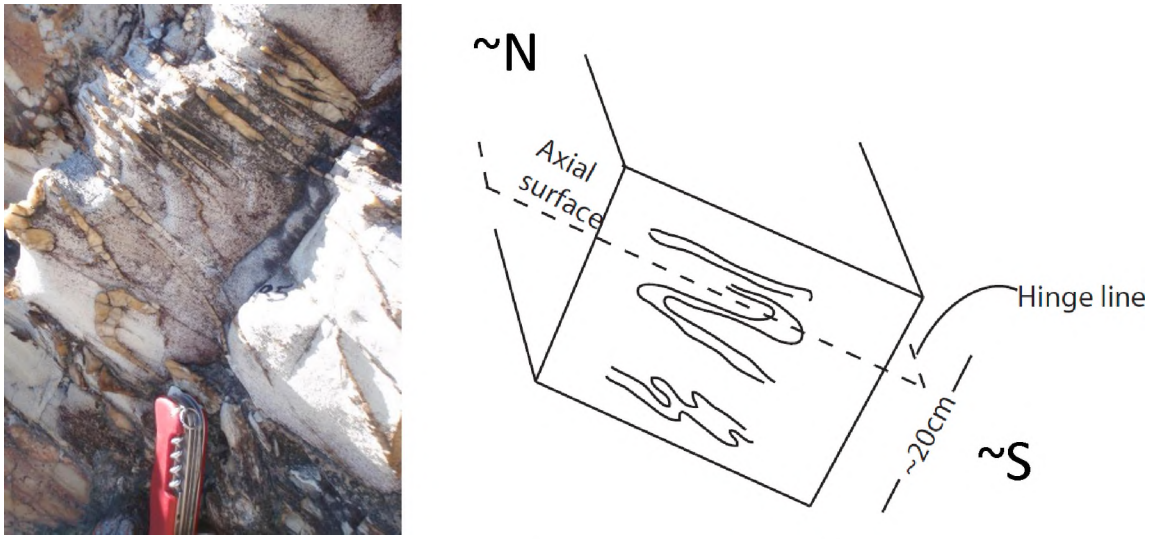

***Figure 3.5**: Sample P5A (Outeniqua Pass) is from a small, symmetric fold characterised by a quartz vein. Although the vein is disrupted, a hinge zone is clearly visible.*

Sample site P7 is on the Montagu Pass, in quartzites of the Tchando Formation. Sample P7A is taken from a poorly characterised ~2 cm thick vein which appears to have been folded. The vein is compatible in orientation with disrupted limbs of tight folds, but there is no hinge zone visible (Figure 3.6). The axial surface of these possible limbs is oriented at approximately 190/44.

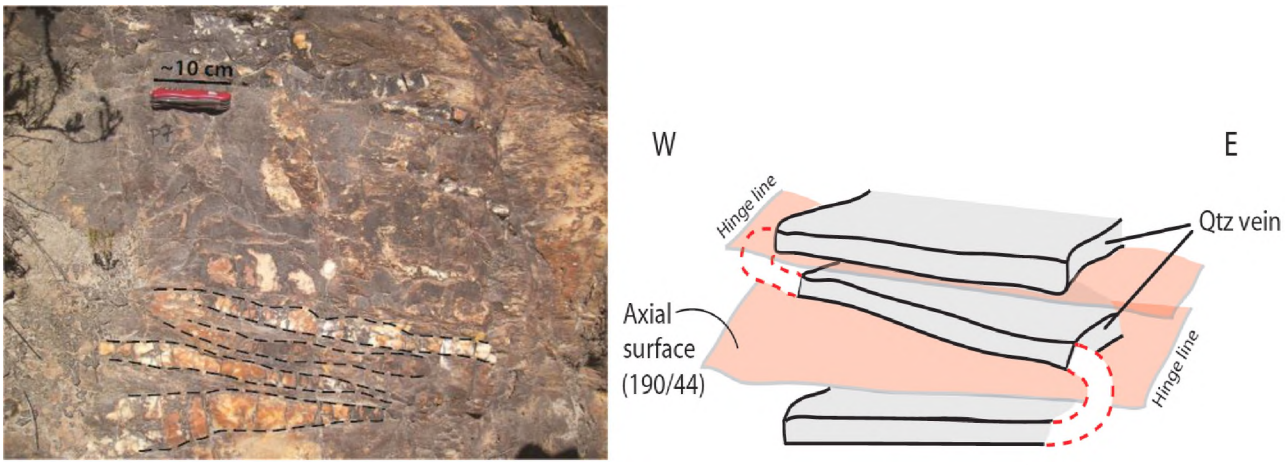

***Figure 3.6**: The Tchando Formation quartzite outcrop at sample site P7 on the Montague Pass (Outeniqua transect). The quartz (Qtz) vein appears to be part of a folded stack, but there are no visible hinge zones to confirm this.*

3.2 De Vlugt to Uniondale profile – Samples P8-P16

There are two clusters of sample sites along this profile (Figure 3.7). Veins are rare to absent in the first part of the profile towards Avontuur, but become abundant again in the northern part of the profile near Uniondale, even though equally good exposures exist all along the profile. The difference between the two profile sections is that the northern part of the profile is characterised by shallow to moderately south dipping fold limbs, while upright folds with moderate to steeply dipping limbs and smaller interlimb angles are typical towards the south. Since most of the veins sampled for this study are associated with shallow south dipping fold limbs or bedding planes, it seems likely that such planar structures were more susceptible to hydraulic failure than steeply oriented planar structures. This also implies that these limbs in the northern and southern part of this profile section were already in a different orientation at the time of faulting and vein formation.

Sites P8 and P9 are in the Baviaanskloof and the Kouga Formations of the upper Table Mountain Group. The sample from site P8 is quartz from vertical en-echelon tension gashes (Figure 3.8). The tension gashes are up to 3 cm thick, hosted in decomposed metagreywackes of the Baviaanskloof Formation.

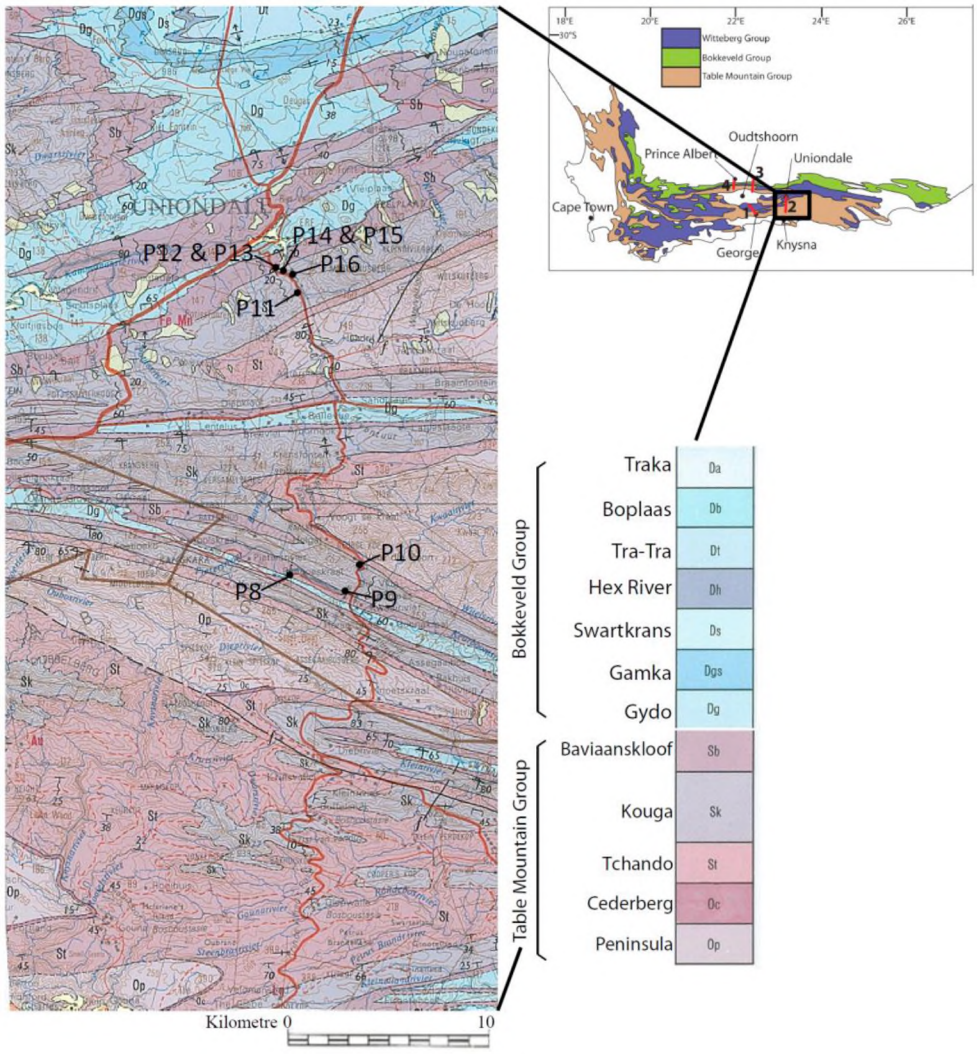

***Figure 3.7**: Locations of sample sites P8-P16 along the de Vlugt – Uniondale transect. All samples from this transect are from the upper two formations of the Table Mountain Group. Samples P8, P9, P12 and P13 are from the Baviaanskloof Formation, and samples P10, P11, P14, P15 and P16 are from the Kouga Formation. (modified after Council for Geoscience, 1979)*

***Figure 3.8**: Sample P8A is from vertical en-echelon tension gashes, hosted in metagreywackes of the Baviaanskloof Formation in the de Vlugt – Uniondale transect. (Penknife for scale, ~10 cm.)*

Sample P9A is from a ~5 cm thick quartz vein along folded bedding in the Baviaanskloof Formation. The vein is parallel to the folded bedding, but cannot be followed as far as the hinge of the fold, and it is not clear whether the vein bent around the hinge or not. Fibrelines on the vein indicate that the vein likely formed as a result of flexural slip, and any fluids in the quartz are therefore likely to have been trapped coeval with the folding event.

Sample P10A is from a vein which has developed along a northward dipping (021/59) dip-slip top-south reverse fault zone in the Kouga Formation. The fault is defined by the ~3 cm thick coherent quartz vein that shows fibrelines (~020/53). The transition to the host rock, a medium-grained, massive white quartzite, is sharp.

Samples P11 – P16 are also from the Baviaanskloof and Kouga Formations of the Table Mountain Group. Samples P12 – P16 were all taken from the same exposure. The coherent quartz vein at P11 is hosted in orange weathering interlayered sandstone and shale. There are layers which have been folded into an open and upright fold, with an amplitude of approximately 3-5 metres. The sample is taken from the south-dipping limb of this upright fold. South-west plunging fibrelines (231/34) and downward-facing slickenside steps on the ~2 cm layer parallel quartz vein indicate top-to-the-north-east kinematics.

Sample P12 is from a ~15 cm thick sinistral reverse-slip fault zone (152/47) in well-layered, medium-grained quartzitic sandstone. The fault is characterised by ~1-2 cm thick individual quartz veins, surrounded by cataclastic fragments approximately 0.5-1 cm in size. There is abundant iron-manganese oxide staining on the joints of the host rock, as well as significant feldspar weathering indicated by the whitish colour and porous texture of the rock surface.

Sample P13 (Figure 3.9 a) is from a coherent quartz vein in a layer-parallel, 2-4 cm thick fault zone in white-grey quartzites. The fault dips at 245/15, with transport lineations (quartz fibrelines) plunging at 176/04. There are whitish, ~10 cm thick shale layers interbedded with the ~30-50 cm thick quartzite layers. The locally overlying and underlying quartzite is strongly foliated and sheared.

Sample site P14 (Figure 3.9 b) is a 1 m thick fault zone (172/42) in light grey slightly phyllitic shale. The fault zone is characterised by cataclastic rock, in which there are disrupted quartz veins, approximately 4-7 cm thick. SC fabrics indicate top-north dextral thrust movement. The shear zone in the shale layer is bounded above and below by feldspathic sandstone.

Sample site P15 (Figure 3.9 c) is at a set of approximately ten narrowly spaced coherent quartz veins, each ~2-3 cm thick. The veins are hosted in the feldspathic quartzite, just below a tectonised zone (166/30). Tectonic strain in this zone is evident by fibrelines (210/24) and slickenside steps on the quartz veins and the quartzite, which indicate top-to-the-NNE sinistral thrust movement.

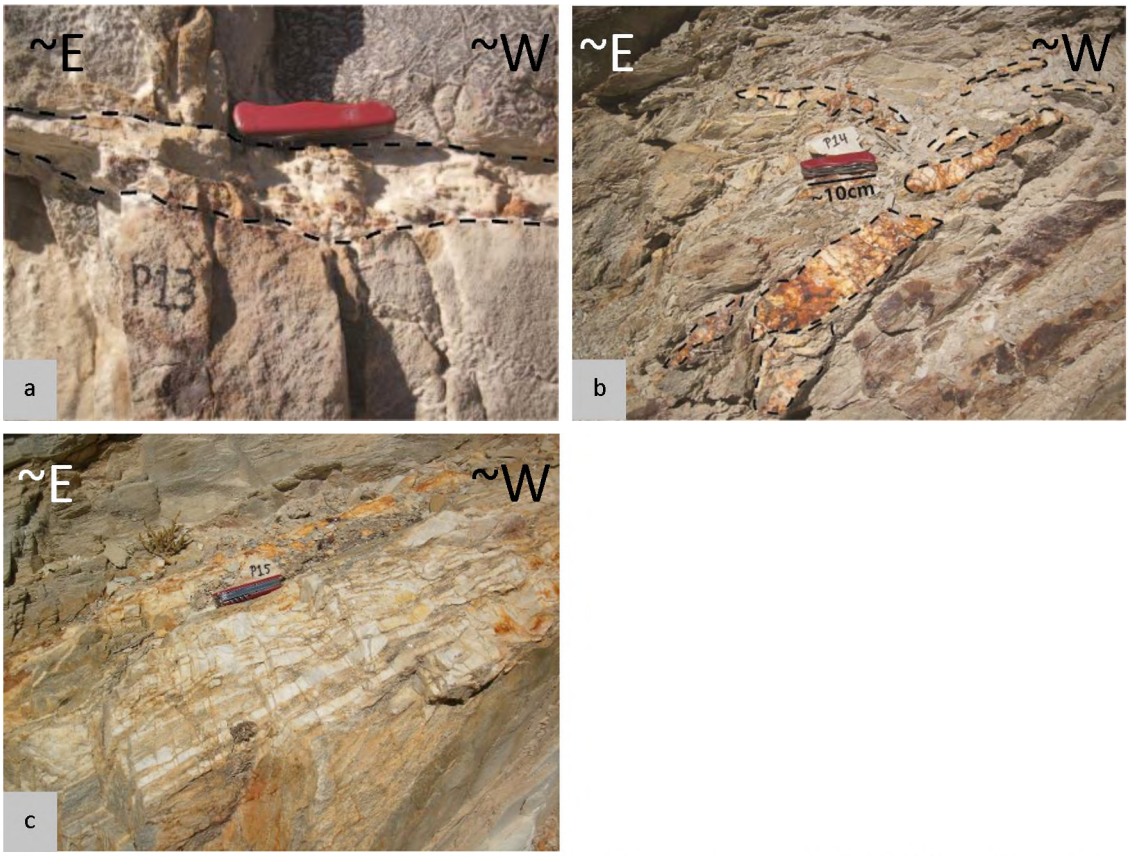

***Figure 3.9**: Sample sites P13, P14 and P15 are all from the same outcrop in the de Vlugt – Uniondale transect. a) Sample P13A is from a quartz vein in a layer-parallel fault, hosted in white-grey quartzites of the Baviaanskloof Formation. (Penknife for scale, ~10cm.) b) Sample P14A is from a disrupted quartz vein in a fault zone hosted by slightly phyllitic shale. c) Sample P15A is from a set of narrowly spaced veins hosted in feldspathic quartzite, just below a tectonised zone.*

Sample site P16 is at a vein in a 6-10 cm thick, layer-parallel thrust zone (174/27) between light brown weathering sandstone layers with crossbedding. There is no shale nearby. P16A samples a thrust zone that is defined by a 6-10 cm thick coherent quartz vein (Figure 3.10). Fibrelines and slickenside steps on the underside of the vein (215/21) indicate top-to-the-north-east sinistral thrust-slip movement. Two more samples, P16B and C, were taken from smaller, secondary veins above the shear zone.

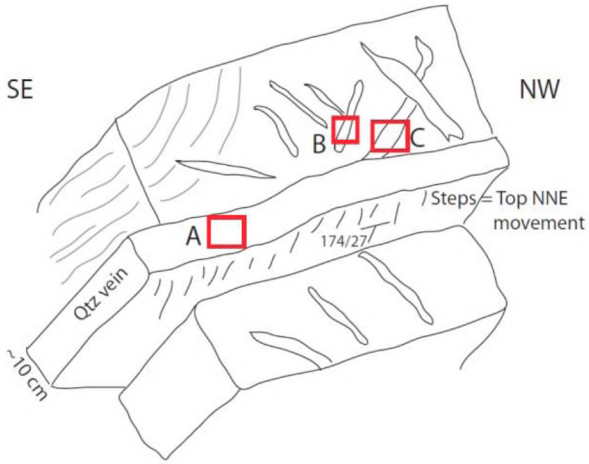

***Figure 3.10**: Sample site P16 is at a quartz (Qtz) vein within a thrust zone in sandstone layers of the Kouga Formation, along the de Vlugt – Uniondale transect. Three samples were taken here, indicated by the red boxes. P16A is from the quartz vein that characterises the fault zone, while P16B and P16C are from secondary veins above the shear zone.*

3.3 Meiringspoort Profile – Samples P17-P25

There are nine sample sites along the Meiringspoort profile (Figure 3.11). The samples include syntectonic veins from thrust and reverse faults in the Table Mountain, Bokkeveld and Witteberg Groups, as well as one sample (P21) from the Pan-African Kango Inlier in the footwall of the Cape Supergroup (Figure 3.2).

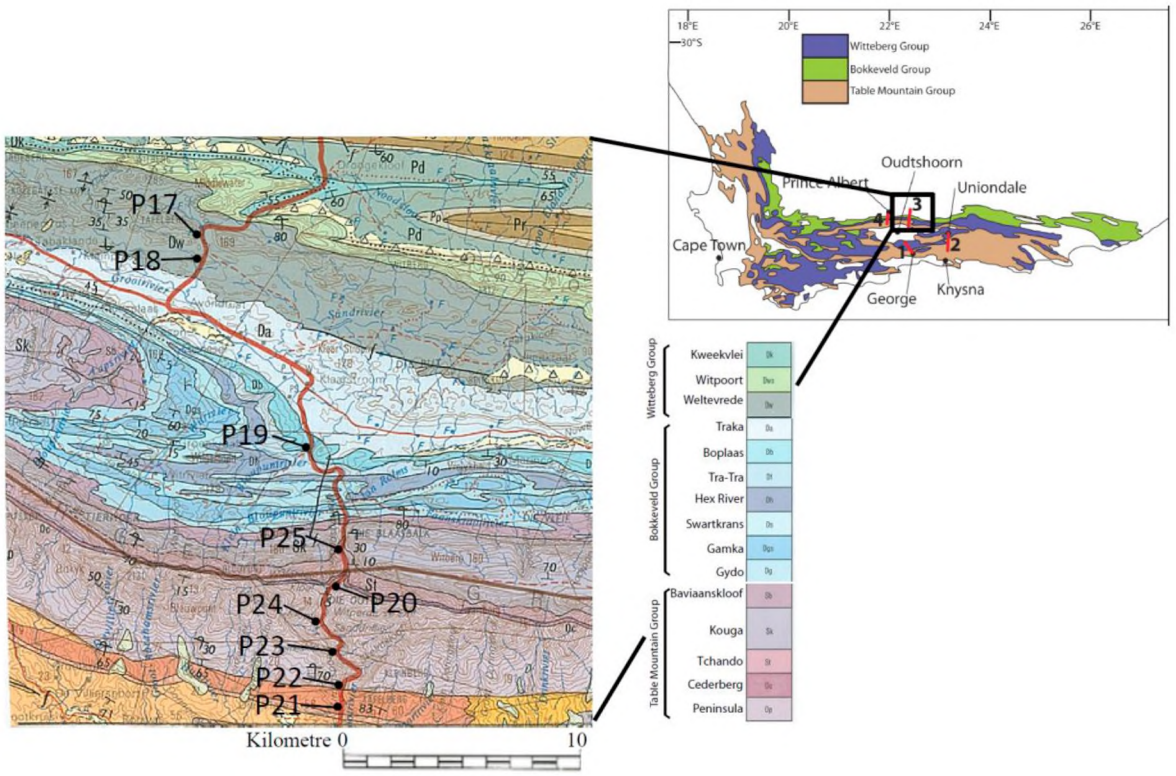

***Figure 3.11**: Sample sites P17 to P25 are from Meiringspoort. P17 and P18 are in the Witteberg Group (upper Cape Supergroup). P19 is in the Bokkeveld Group. P20 to P25 are in the Table Mountain Group (modified after Council for Geoscience, 1979).*

Sample site P17 (Figure 3.12) is at an anticlinal/synclinal fold in the Weltevrede Formation of the Witteberg Group. The fold is open and asymmetric, with a subhorizontal hingeline (~100/05) and north-vergent axial surface. The anticline has a long, shallowly south dipping (~184/55) southern limb and short, steeply north dipping (~009/85) northern limb – typical of the folding style in the CFB. There is a second-order z-fold between layers of quartzite of the first order fold (Figure 3.12). The parasitic fold is characterised by a thin (~0.5 cm) disrupted quartz vein, from which sample P17A was taken. Sample P17B is from en-echelon tension gashes on the southern limb of the anticline, perpendicular to the primary layering. The tension gashes are approximately parallel to σ_1 of the folding stress field, therefore may be compatible with N-S shortening. The same applies to the north-verging folds.

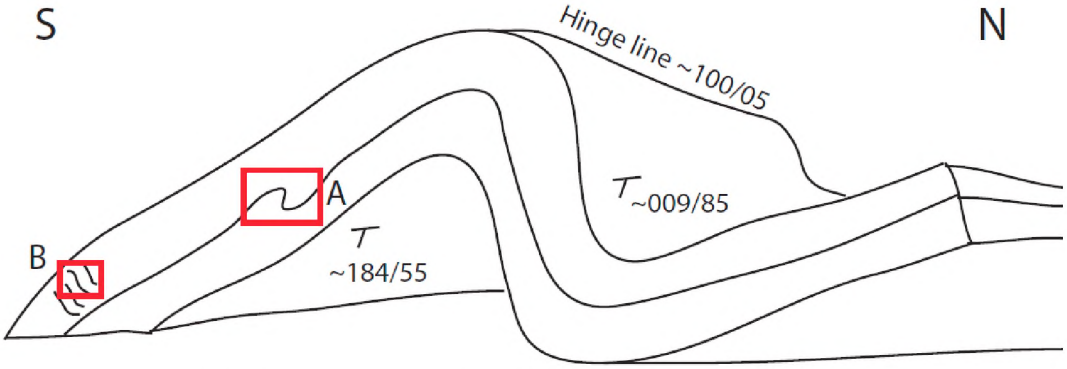

***Figure 3.12**: Sample P17A is from a parasitic fold on the southern limb of a larger, first order fold along the Meiringspoort profile. The anticline has a long, shallow southern limb and a shorter, steeply dipping northern limb – a typical folding style of the CFB. P17B is from en-echelon tension gashes, also on the southern limb of the first order fold.*

Sample site P18 shows a sequence of intensely folded shales with minor interbedded fine-grained sandstone of the Weltevrede Formation (Witteberg Group). A quartz vein (~4 cm thick) within the shale has been affected by the intense folding, and in places is disrupted by boudinage. It is possible, however, to trace this quartz vein along the fold. Three samples were taken here – P18A and P18B are from the hinge zone, and P18C is from a fold limb (Figure 3.13).

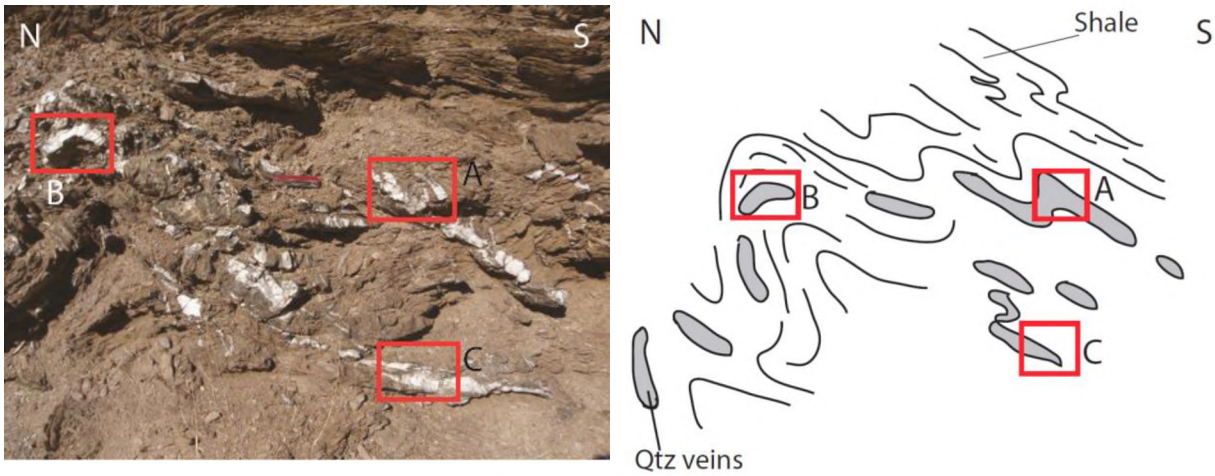

***Figure 3.13**: Sample site P18, along the Meiringspoort transect, shows complex folding in shale which affected pre-fold quartz (Qtz) veins. Three samples, P18A, P18B and P18C, were taken here, indicated by the red boxes. P18A and P18B are from hinge zones, while P18C is from a fold limb.*

Sample site P19 is at a top-north thrust flat ramp structure in the Boplaas Formation of the Bokkeveld Group. The outcrop consists of a thick (~25-30 m) quartzite package, in which quartz layers dip shallowly towards the south, and have been thrust northwards along a discordant, moderately south-east dipping ramp (155/18) (Figure 3.14). Above the ramp, the quartzite layers have been folded in response to the tectonic displacement along the ramp, to form an open, asymmetric main anticline. From south to north, a trailing syncline is followed

by a trailing anticline, which are connected by a moderately south dipping long limb. The trailing anticline merges with the leading anticline, and together they constitute the hinge zone of the main anticlinal fold of the flat-ramp structure. The northern limbs of the anticlines are short and dip steeply north, whereas the longer southern limbs dip more gently towards the south. The axial surface of the main anticline dips steeply south at ~60 °.

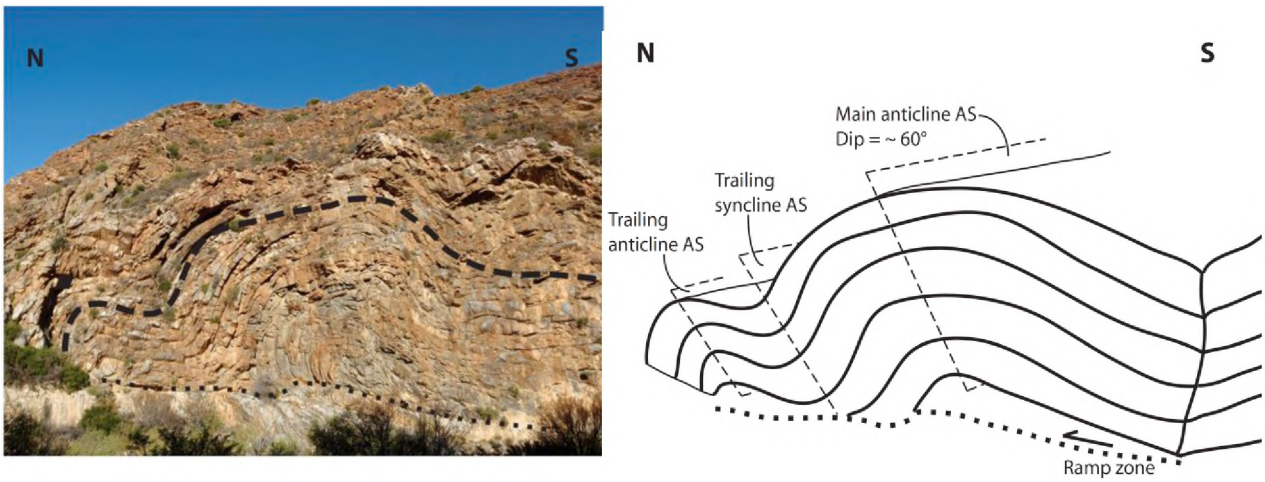

***Figure 3.14**: Sample site P19 is at a top-north thrust flat ramp structure along the Meiringspoort transect. Shallowly south-dipping quartz layers have been thrust northwards along a south-east dipping ramp. Quartz layers above the ramp have been folded to form a main, open anticline, which is followed by a trailing syncline and a trailing anticline towards the north.*

Sample P19A is from a ~3 cm thick coherent quartz vein in the thrust fault, while sample P19B is from a set of en-echelon tension gashes below the ramp (Figure 3.15), the centres of which define a north-dipping semi-brittle shear zone. The tension gashes dip shallowly south and show significant rotation during growth, with horizontal tips. The shallow southern dip angle is compatible with north-south contraction and with the displacement along the nearby flat ramp structure, which has a top-north kinematic sense.

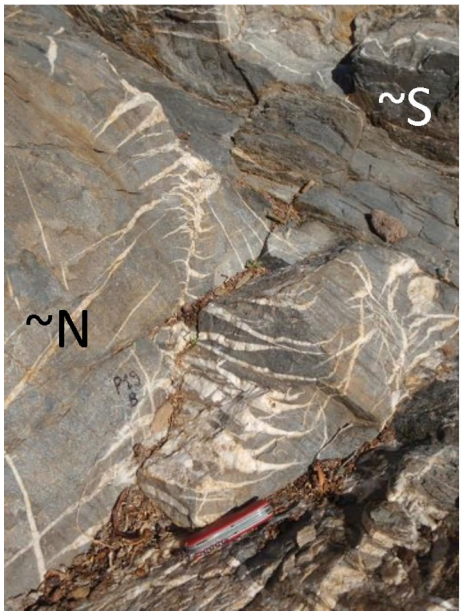

***Figure 3.15**: Sample P19B is from rotated en-echelon tension gashes just below a flat ramp structure in the Meiringspoort transect. The tension gashes dip shallowly south, and show significant rotation during formation, with horizontal tips.*

Sample site P20 is at the access path to the Meiringspoort waterfall. P20A is from a ~5 cm thick, coherent synkinematic quartz vein that developed along a fault with top-north-east kinematics (fault ~238/17; lineations ~234/17). The vein is hosted in dark grey Peninsula Formation quartzite that is over several metres thick. Semi-brittle SC-fabrics and C' fabrics indicate northward shearing in a major shear zone. Fibrelines in the quartz vein are parallel to the transport lineations of the shear zone in the host rock.

Sample P21A is from a coherent vein in phyllite of the Pan-African Kango Inlier. Hence, this vein is hosted in Proterozoic rocks, whereas all other samples were taken from the Palaeozoic Cape Supergroup. The age of the sampled vein, however, is unknown, and fluid influx might be either of Cape or of Pan-African age. The sample is ~3 cm thick, but the vein widens out to ~40 cm. The vein is associated with a fault; lineations and S-C fabrics indicate top-north kinematics (Figure 3.16).

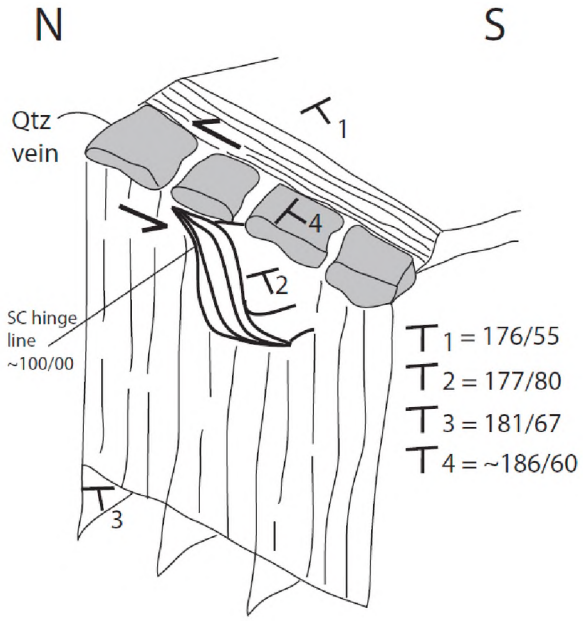

***Figure 3.16**: Sample site P21 is at a disrupted quartz (Qtz) vein in a top north reverse fault, hosted by phyllites of the Kango inlier. Lineations and SC fabrics indicate top-north movement. Readings were taken at (1) the foliation above the vein, (2) SC fabrics, (3) foliation below the vein, and (4) a bearing was taken of the vein.*

Site P22 is at a steeply north-dipping reverse fault (014/70) in Peninsula Formation quartzites, close to the contact with the Pan-African Kango inlier. There are abundant, thick (~5-10 cm) quartz veins, but many are massive and do not show fibrous quartz, whereas other veins do show fibrelines, indicating synkinematic fluid influx. Sample P22A is from a disrupted ~5 cm thick vein in a 40-50 cm thick fault zone, which extends upwards over 20 m (Figure 3.17). Fibrelines and slickenside steps on the vein indicate top-south reverse faulting.

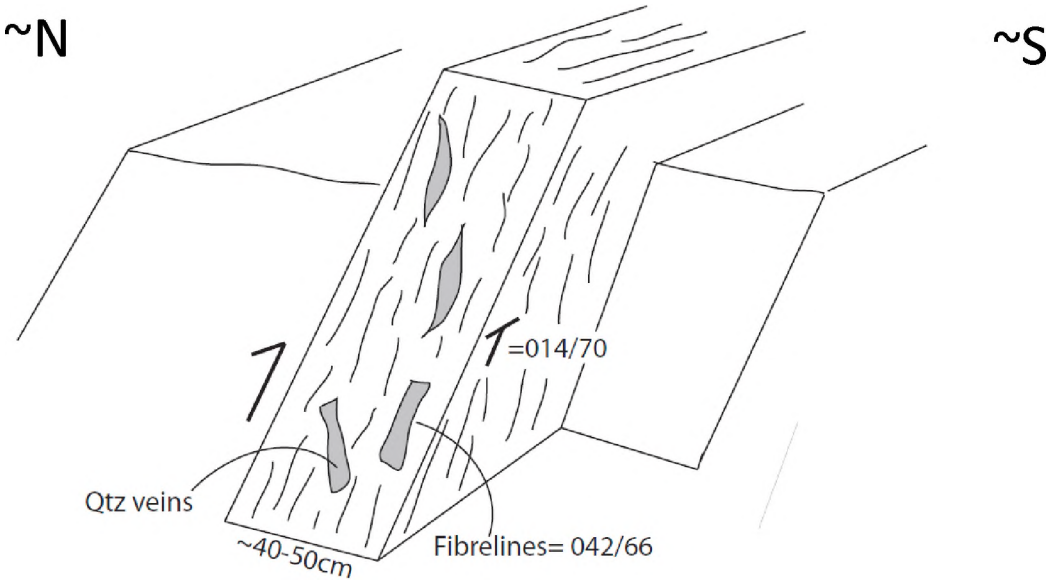

***Figure 3.17**: Sample site P22 is at a steep, north-dipping reverse fault in Peninsula Formation quartzites along the Meiringspoort transect. The quartz (Qtz) vein is disrupted, and slickenside steps on the vein indicate top-south movement. The vein is in a cohesive quartzite matrix.*

Site P23 is along the bridge at Dubbeldrif se Draai. Three samples were taken here, all hosted within the Peninsula Formation. P23A is from one of many veins in a shallow south-dipping, top-north thrust (fault ~184/10; lineation ~190/08). The vein is approximately 10 cm thick and coherent. The fault is roughly layer-parallel, hosted in medium-grained, light grey quartzite. P23B is from a ~10 cm thick vein in a steep, sub-vertical fault (fault: ~188/84; lineation: ~190/83), along which the northern block has moved up (relative to the current orientation of the fault). Sample P23D is from a thrust fault similar to that at which P23A was taken. A thick (5-30 cm), laterally extensive quartz vein is hosted in a shallow to horizontal thrust (sub-horizontal; lineation ~024/15. Abundant fibrelines and slickenside steps indicate top-north movement.

Sample site P24 is at Wa Drif, at a (apparently) dextral normal fault (fault ~186/70; lineation 224/66) in steep to vertical bedding of the Peninsula Formation. The fault is characterised by a syntectonic vein, approximately 4 cm thick and coherent. Fibrelines and slickenside steps indicate top-south movement. The host rock is a poorly layered, medium-grained massive quartzite with an orange weathering surface.

Sample site P25 is close to the northern end of the Meiringspoort transect, at a shallowly south-west dipping, top-north thrust fault (fault ~220/08; lineation ~189/03) hosted in the Tchando Formation of the Table Mountain Group. There are several veins up to 10 cm thick in the ~40 cm thick shear zone with abundant fibrelines and laterally intense SC fabrics. The quartz veins are disrupted at the SC fabrics, suggesting the fault was possibly reactivated under dry conditions or its activity outlasted the precipitation of vein quartz.

3.4 Swartberg Pass – Samples P26-P28

Syntectonic quartz veins are rare on the Swartberg Pass. Only three samples were taken, from reverse and thrust faults, all hosted within the Table Mountain Group (Figure 3.2 & Figure 3.18).

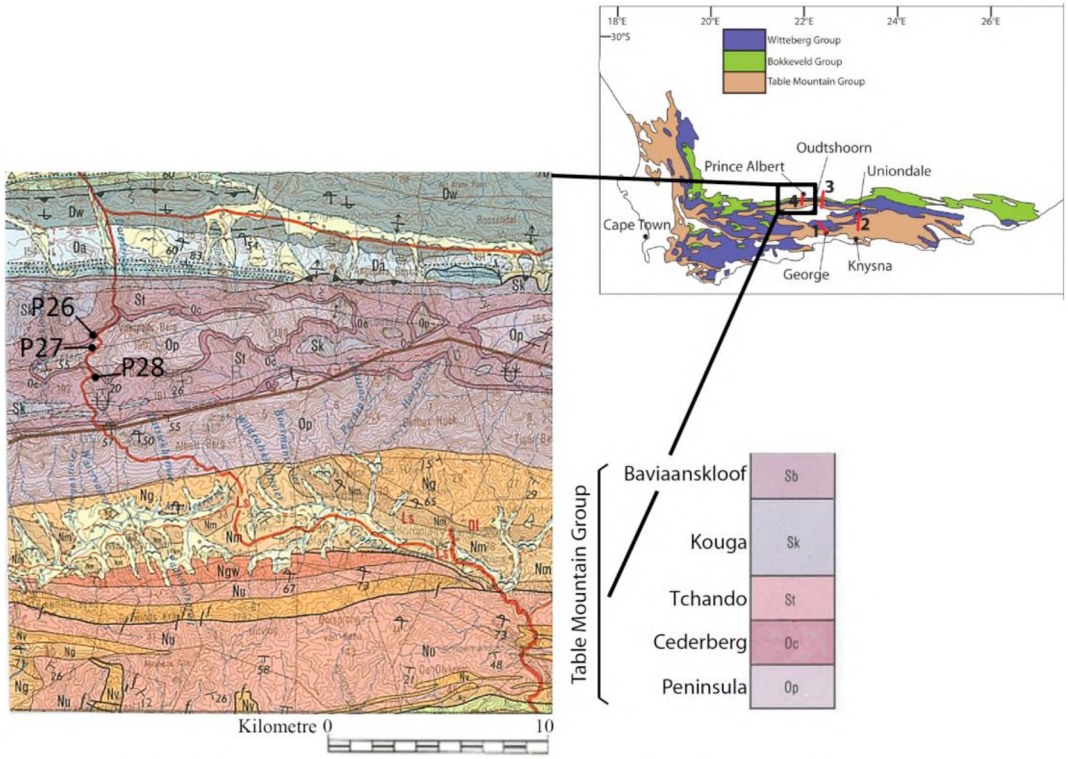

***Figure 3.18**: Sample sites P26 to P28 are from Table Mountain Group rocks from the Swartberg Pass. P26 and P27 are from the Peninsula Formation, while P28 is from the Tchando Formation (modified after Council for Geoscience, 1979).*

Sample P26A is a synkinematic vein from a 2 m wide top-NE reverse fault zone (fault plane ~170/66; lineations ~227/56). P27A is from a 2-5 cm thick, coherent vein, in a shear zone that is parallel to the subhorizontal (014/15) bedding. Fibrelines are present (010/10), but no shear sense indicators are present along this shear zone. Sample P28A is from a strongly weathered, ~1-2 cm thick syntectonic vein in a ~1-5 cm thick sinistral thrust fault (fault ~107/27; lineation ~167/10) in the Peninsula Formation. SC fabrics indicate the top-north movement.

3.5 Kango Fault

Three samples, P29A-C, were taken at the Kango Fault. The samples are taken from a ~100 long and 30 m high exposure of Cape Supergroup quartzite showing a complex network of quartz veins. Abundant veins indicate that fluid influx was pervasive, but relative age successions could not be systematically obtained. P29A and P29B were taken from a rare spot where relative age is unambiguous (Figure 3.19), where one vein (sample P29A) has been cut off and displaced along a younger vein (sample P29B). P29C was taken from a nearby, 0.4-1 m thick vertical vein. None of these veins shows evidence for a syntectonic lateral displacement

component (fibrelines). Failure may have taken place by mode 1 tensile opening, but there are also no fibres at high angle to the vein boundaries present to confirm this.

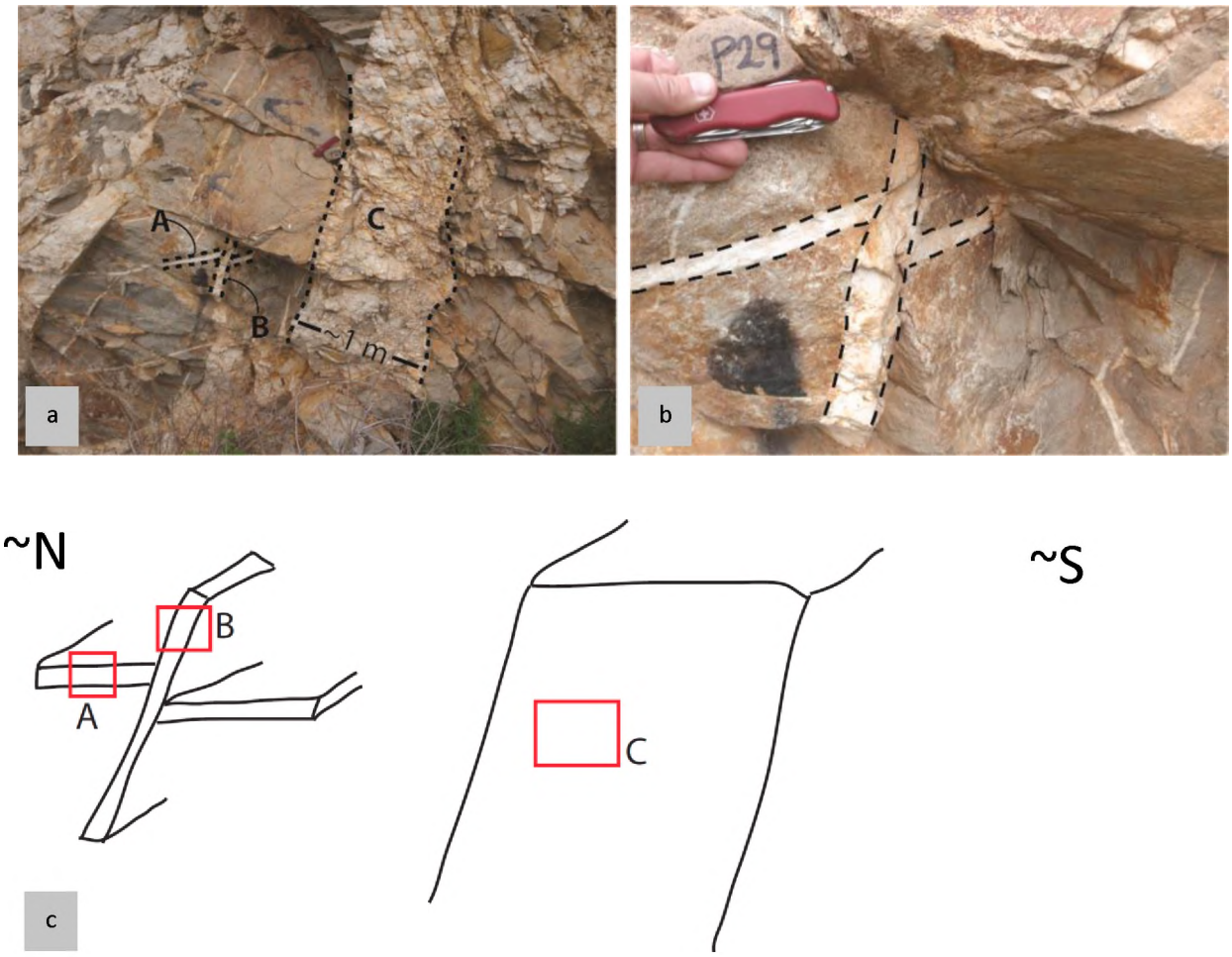

***Figure 3.19**: Sample site P29 is at a complex network of veins at the Kango fault. A) Sample localities for P29A, B and C. b) A rare spot where the relative ages of two veins is unambiguous, where samples P29A and P29B were taken. c) Outcrop sketch of sample site P29, showing the localities of samples A, B and C.*

4. PETROGRAPHY: QUARTZ FABRICS

In this chapter I will describe the quartz microstructures in deformed and undeformed hydrothermal veins. Primary hydrothermal quartz is large in grain size, typically exceeding 1 mm and reaching up to 7 mm. Commonly, quartz shows evidence of plastic deformation, such as undulose extinction, subgrains, deformation or kink bands, or features that indicate recrystallization.

Undulose extinction is a wavy and changing extinction position under the microscope that is not spatially defined by planar boundaries. **Subgrains** show such boundaries, and, within the space they define, the extinction position is largely uniform (Shelley, 1993). The difference in extinction position of neighbouring subgrains does not exceed ~5° (Shelley, 1993). **Deformation bands** are subgrains with an elongate shape that are present through an entire grain. The difference between deformation bands and **kink bands** is somewhat gradual, but kink bands show a larger difference in extinction position across their boundary, and in places a high-angle boundary or fracture might be seen along kink bands (Vernon, 2004). **Recrystallization** may occur in two different ways, by grain boundary migration or by subgrain rotation (Passchier & Trouw, 1998). The result in both cases are new, optically strain-free grains bound on all sides by high angle boundaries (Passchier & Trouw, 1998). Subgrain rotation increases the tilt across subgrain boundaries by accumulating more and more dislocations (by dislocation slip or glide) until high angle boundaries form (Passchier & Trouw, 1998). Grain boundary migration recrystallization, forming serrated grain boundaries, might lead to the isolation of small quartz domains, which eventually are bound on all sides by high-angle boundaries (Passchier & Trouw, 1998).

Both recrystallized grains formed by subgrain rotation or grain boundary migration might undergo static recrystallization, which straightens curving shapes of grain boundaries and eventually might form stable grain configurations (Passchier & Trouw, 1998). These are indicated by planar boundaries intersecting in 120 ° (Shelley, 1993). Such patterns are referred to as *foam texture*.

4.1 Thrust faults

Thrust fault samples from the Outeniqua Pass (P1A, P2A, P3A and P6A from the Peninsula Formation, and P5C from the Tchando Formation), the de Vlugt – Uniondale transect (P11A, P14A and P15A, all from the Kouga Formation), and the Swartberg Pass (P28A from the Tchando formation) show similar characteristics of deformation. All these deformed quartz vein samples consist of medium to large (up to ~3000 μm long) anhedral grains. They range from roughly equant to elongate in shape. Gradational transition between subgrains and new, strain-free smaller grains that are bound by high-angle boundaries indicates recrystallization by subgrain rotation (Figure 4.1 a). However, serrated grain boundaries are also common, along which, in places, small strain-free grains form, indicating recrystallization by grain boundary migration (Figure 4.1 b; Hobbs et al., 1976; Passchier and Trouw, 1998; Vernon, 2004).

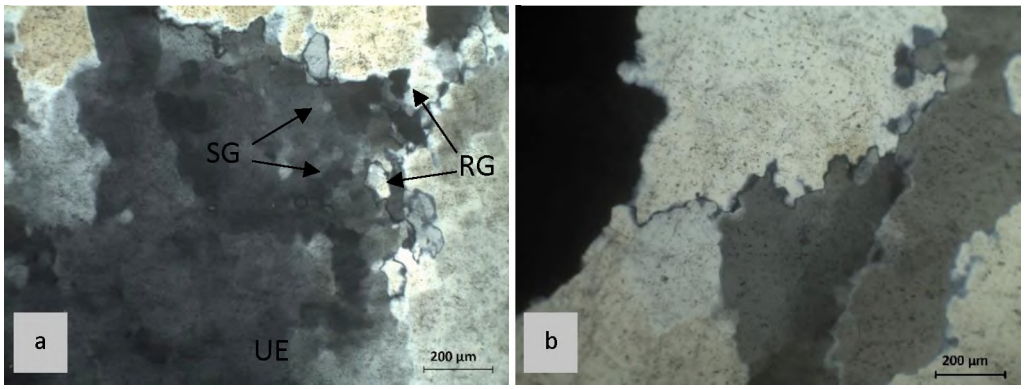

Figure 4.1: *a) Undulose extinction (UE) grades into subgrains (SG) and then recrystallized grains (RG) in sample P3A. b) Grains also show serrated boundaries where grain boundary migration and, in places recrystallization have taken place (thrust sample P3A, Outeniqua).*

By contrast, the samples from Meiringspoort, (P20A, P23A, and P23D from the Peninsula Formation; and P25A from the Tchando formation) show much less intense deformation. Samples P20A, P23A, P23D and P25A show very large, elongate old grains (up to ~7000 µm long, but only ~1000-2000 µm wide). These grains show undulose extinction (Figure 4.2 a), but very little, if any, recrystallization has taken place. The grain boundaries are smooth, and indication of grain boundary migration is not evident (Figure 4.2 b). Sample P19A, from the Boplaas Formation at Meiringspoort is however almost entirely recrystallized, with only a few relicts of old grain left (Figure 4.2 c).

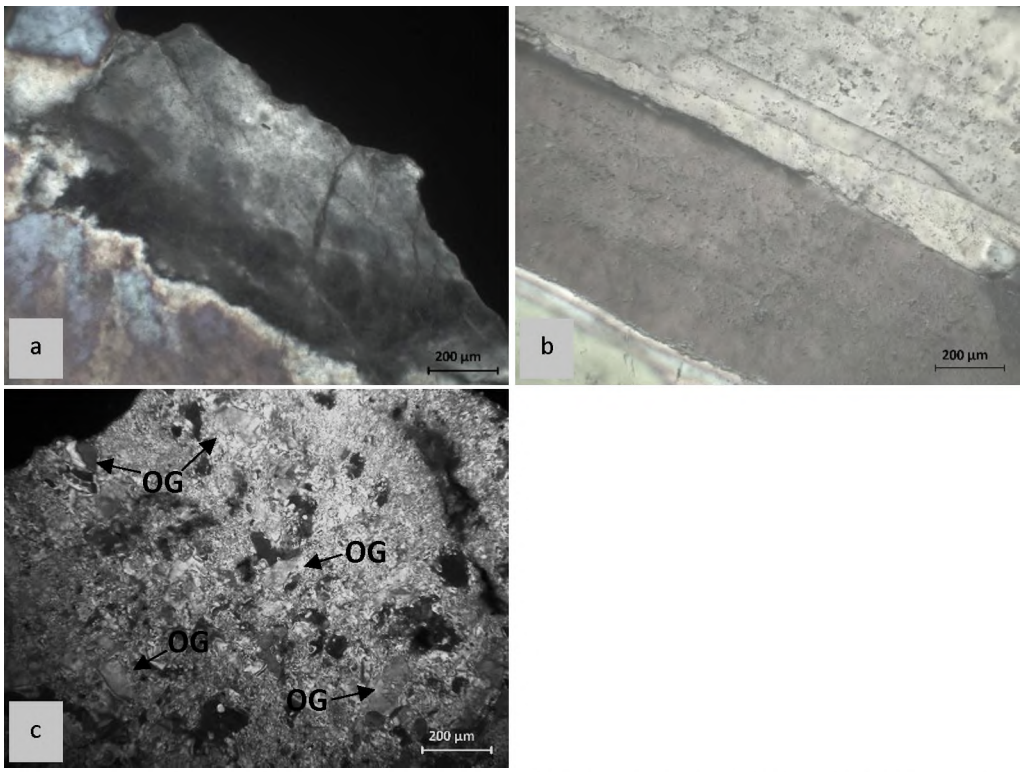

Figure 4.2*: a) Grains show undulose extinction but there is no prominent development of subgrains (sample P23D, Meiringspoort). b) Grain boundaries of primary hydrothermal grains are smooth in most of the Meiringspoort samples (sample P2OA). c) Thrust sample P19A (Meiringspoort) is largely recrystallized, with only a few old grain (OG) relicts remaining.*

4.2 Reverse faults

There are four reverse fault samples – one each from the de Vlugt – Uniondale transect (P10A), the Meiringspoort transect (P22A), the Swartberg Pass transect (P26A), and one sample taken from the Kango Inlier (P21A). The samples all show very similar deformation microstructures.

Grains are generally fairly large, reaching ~5000 µm. They are elongate, and all display undulose extinction (Figure 4.3 a). In sample P10A, deformation bands have developed (Figure 4.3 b). In places, serrated grain boundaries indicate grain boundary migration (Figure 4.3 c & d), but the absence of small quartz grains along these grain boundaries shows that this did not lead to recrystallization.

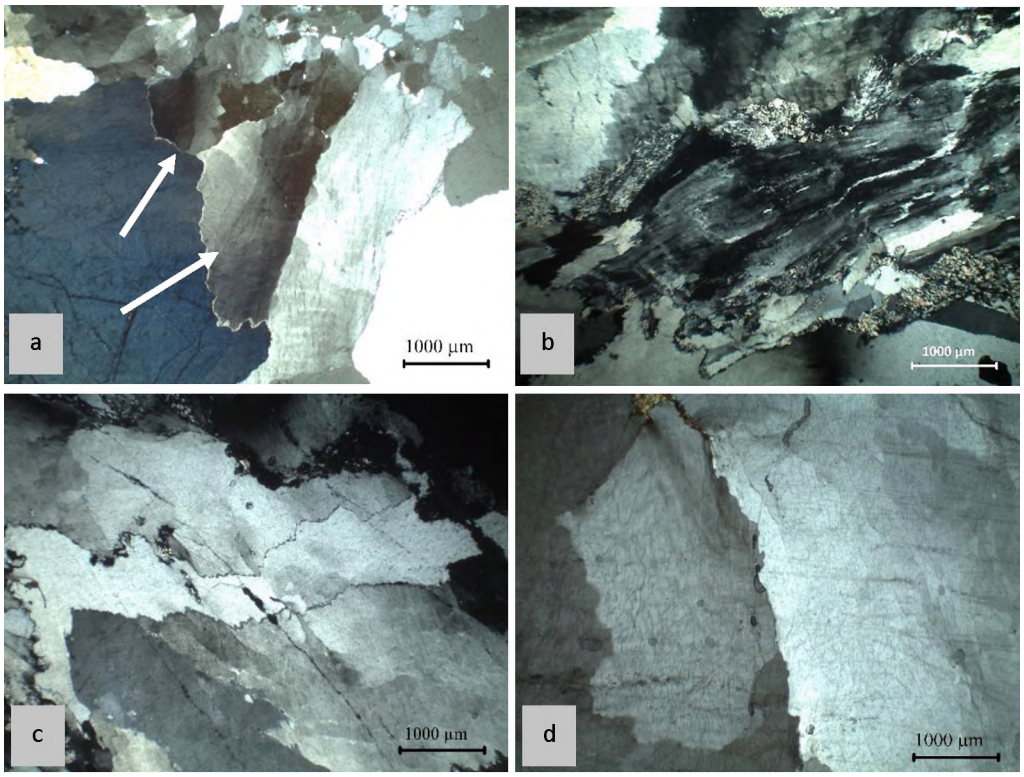

***Figure 4.3**: a) Undulose extinction occurs in all reverse fault samples, shown here in sample P22A (Meiringspoort). b) Deformation bands have developed in sample P10A (de Vlugt – Uniondale) only. c) Finely serrated (P10A, de Vlugt – Uniondale) and d) coarsely serrated grain boundaries (P22A, Meiringspoort) in hydrothermal quartz from reverse faults.*

In sample P22A (Peninsula Formation, Meiringspoort), old hydrothermal grains grade into subgrains and eventually into a zone where small grains are bound by high-angle boundaries. This pattern is interpreted as evidence of subgrain rotation recrystallization (Figure 4.4 a). Old grains, subgrains and recrystallized grains show abundant solid and fluid inclusions, indicating that such inclusions were not removed during subgrain rotation recrystallization. In places, recrystallized grains are up to ~300 µm in size, are roughly equant in shape, and have straight grain boundaries with 120° interface angles. These textures are interpreted as foam structures (Figure 4.4 b). These features require quartz recrystallization, which takes place under at least greenschist facies conditions (e.g. Voll, 1969; Shelley, 1993; Passchier and Trouw, 1998; Vernon, 2004). In addition, the postkinematic temperature must have remained high enough

for a sufficiently long time in order to form the equilibrated texture of the foam structure (i.e. static recrystallization; Passchier and Trouw, 1998).

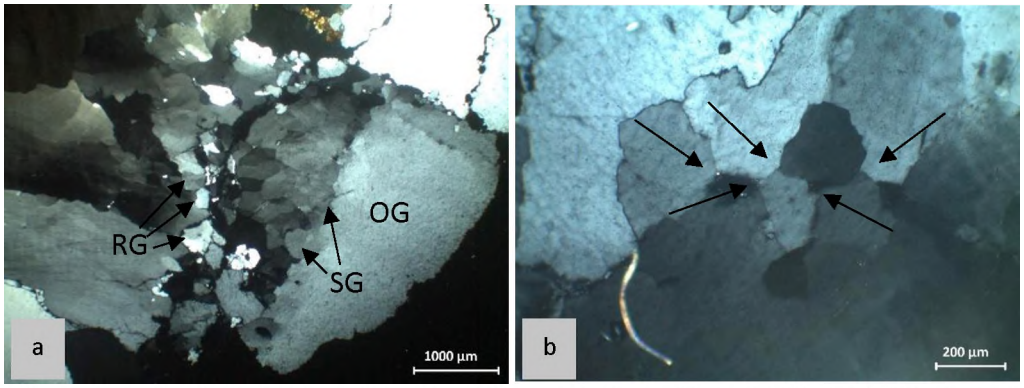

***Figure 4.4**: a) Old hydrothermal grains (OG) grade into subgrains (SG) and then into recrystallized grains (sample P22A, Meiringspoort). b) Foam texture is present in sample P22A, indicated by the 120° triple junction interface angles of subgrains.*

In sample P10A, there are ~1 mm-sized mica aggregates consisting of numerous individual crystals (Figure 4.5 a). Their primary origin is unclear. These clusters might have developed from larger primary grains that underwent recrystallization. They might have formed in the hydrothermal vein or might be host rock material that became entrained into the vein.

In sample P22A, chlorite forms individual and undeformed crystals of up to ~50 µm in size (Figure 4.5 b). These are interpreted as hydrothermal crystals that precipitated together with the vein quartz.

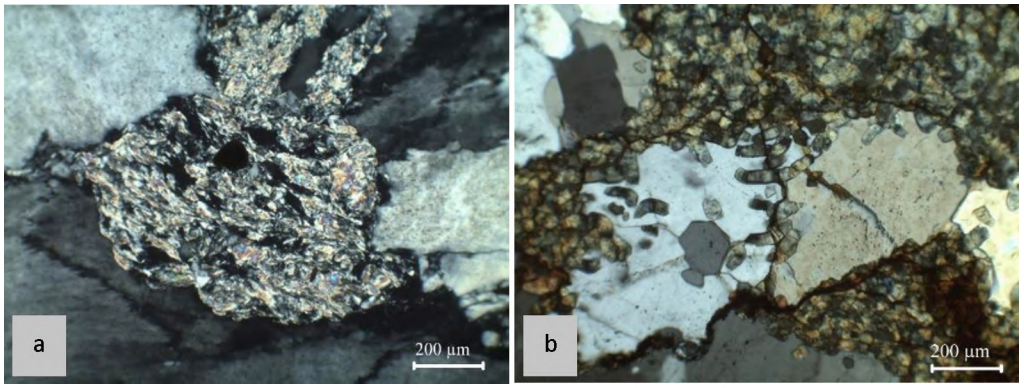

***Figure 4.5**: a) Mica flakes in sample P10A (de Vlugt – Uniondale). The non-uniform extinction position and non-uniform interference colours suggest that this is an aggregate of multiple grains that may have formed by deformation or recrystallization of an initially larger grain. b) Individual and undeformed crystals (probably chlorite) were most likely precipitated together with the vein quartz (sample P22A – Meiringspoort).*

4.3 Normal faults

There are two samples from normal faults, P23B and P24A, both from the Peninsula Formation, and both from the Meiringspoort transect. In both samples, grains are medium- to coarse-grained (up to ~ 500-1000 µm). In P23B, the grains are roughly equant, but elongate grains are more common in P24A. In both samples P23B and P24A, old grains show undulose extinction (Figure 4.6 a), but subgrains are not observed. Deformation bands have developed in a few grains in P24A (Figure 4.6 b).

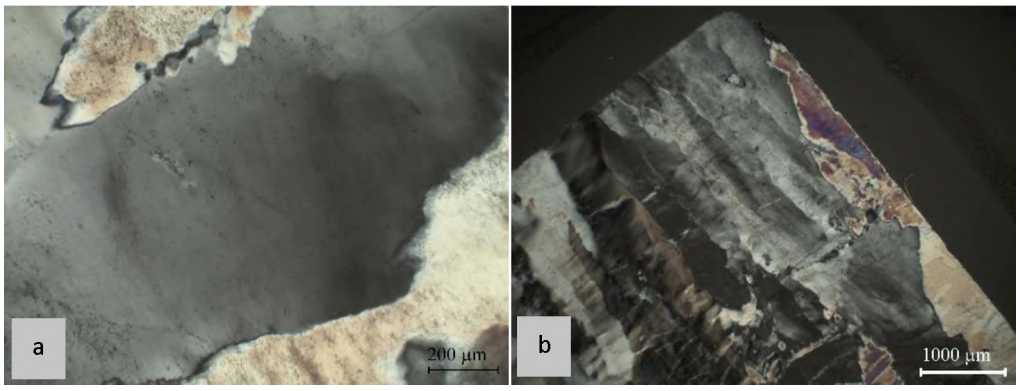

***Figure 4.6**: a) Undulose extinction (P24A, Meiringspoort) has not developed into subgrains. b) Deformation bands at high angle to subgrain boundaries in grains that also show undulose extinction. This may suggest several episodes of deformation (sample P24A).*

In both samples grain boundary migration is evident by the presence of serrated grain boundaries (Figure 4.7 a). Along some of these boundaries, the presence of small quartz grains indicates that recrystallization by grain boundary migration has taken place (Figure 4.7 b). In sample P24A, kink bands have formed, suggesting deformation in the brittle-ductile transition (Figure 4.7 c).

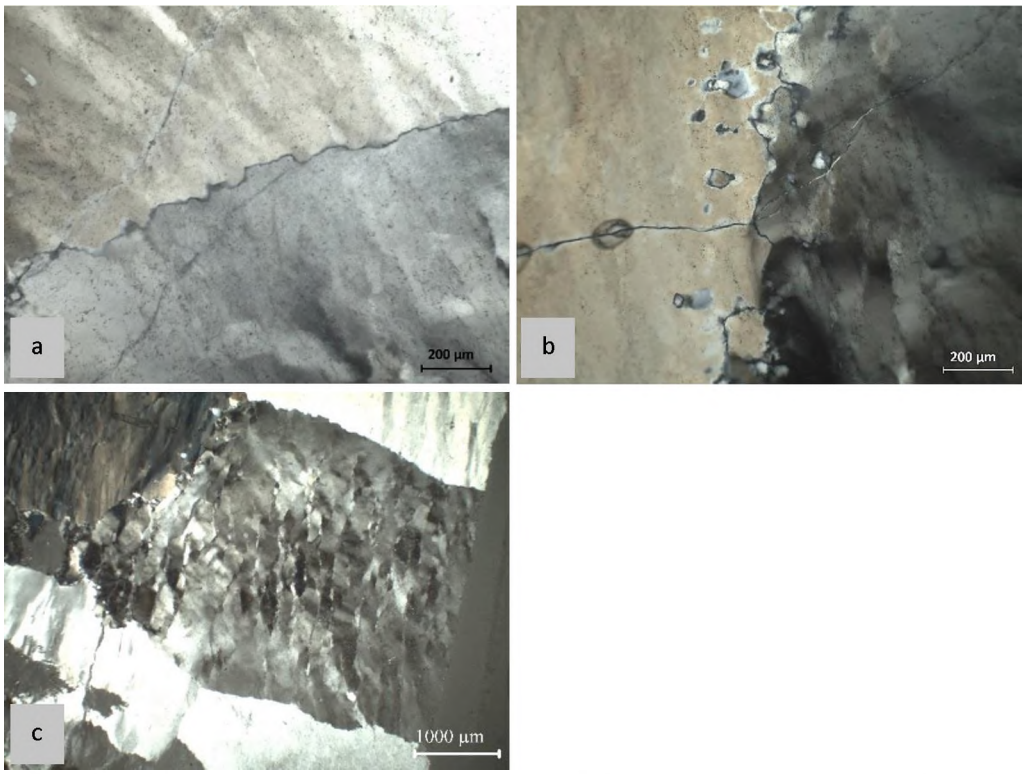

***Figure 4.7**: a) Serrated grain boundaries in sample P24A (Meiringspoort). b) The presence of small quartz grains along serrated quartz boundaries indicates that recrystallization by grain boundary migration has taken place in sample P24A. c) Subgrains and crosscutting kink bands in sample P24A.*

4.4 Oblique- and strike-slip faults

Sample P12A is from a strike-slip fault in the Baviaanskloof Formation in the de Vlugt – Uniondale transect. It is mostly medium- to coarse-grained (~500-1000 µm), but some grains reach up to ~5000 µm. Sample P16A, from an oblique-slip fault in the Kouga Formation, is also from the de Vlugt – Uniondale transect, and also has large, primary hydrothermal grains, reaching up to ~4000 µm across.

The quartz shows strong undulose extinction, which grades into subgrains and in places into grains bounded by high-angle boundaries, indicating recrystallization by subgrain rotation (Figure 4.8 a). The recrystallized grains are ~50 µm in size, and, in a few areas, form 120° triple junction boundaries, indicating the formation of foam texture (Figure 4.8 b).

The samples also show grains with serrated boundaries (Figure 4.8 c), and along these boundaries, the presence of very small (~20µm) quartz grains (Figure 4.8 d) indicates recrystallization by grain boundary migration. Deformation bands in strongly bent, large hydrothermal grains have developed in P16A (Figure 4.9).

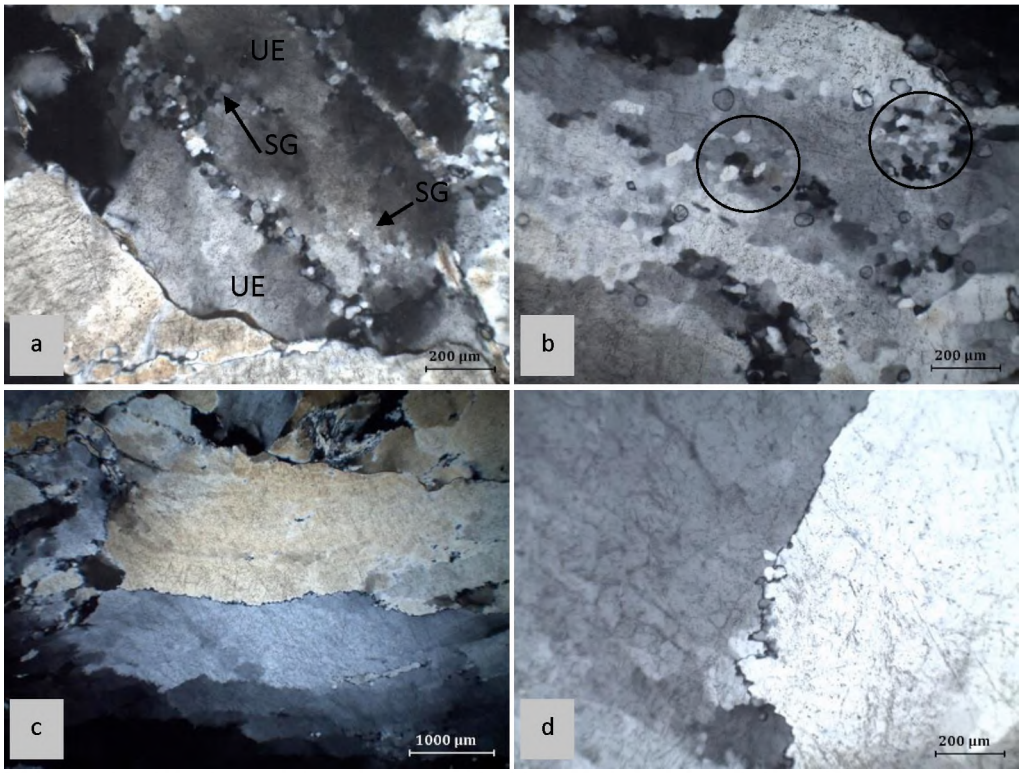

***Figure 4.8**: a) In oblique-slip fault sample P16A (de Vlugt – Uniondale), undulose extinction (UE) grades into domains of subgrains (SG) and new grains, indicating that recrystallization by subgrain rotation has occurred. b) In some areas, these subgrains form triple junction boundaries to form foam texture. c) Grains in P16A have finely serrated boundaries, and d) small recrystallized quartz grains are present in places along or nearby such boundaries.*

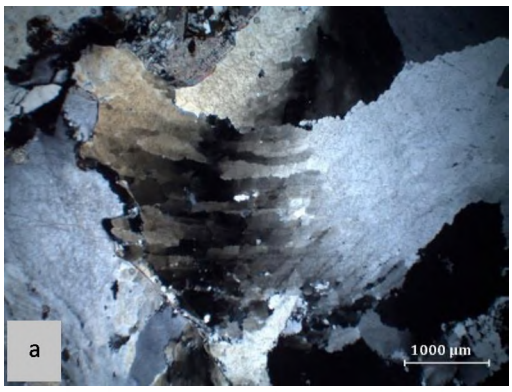

***Figure 4.9**: Deformation bands in oblique-slip sample P16A (de Vlugt – Uniondale).*

4.5 Tension gashes

Six tension gashes were sampled from the four transects in the study area. Sample P5B (Tchando Formation) is from the Outeniqua Pass; P8A (Baviaanskloof Formation), P16B and P16C (both Kouga Formation) are from the de Vlugt – Uniondale transect; and P17B (Weltevrede Formation) and P19B (Boplaas Formation) are both from Meiringspoort. Irrespective of locality and transect, the hydrothermal quartz from tension gashes shows similar petrographic and deformation characteristics.

Primary hydrothermal grains are anhedral and range in size from ~100 to ~3000 µm. The samples show strong undulose extinction in old (hydrothermal) grains (Figure 4.10 a). Undulose extinction grades into areas of subgrains, and then small, individual quartz grains, indicating recrystallization by subgrain rotation (Figure 4.10 a). The recrystallized grains are ~50 µm in size, and, in a few areas, form 120° triple junction boundaries, indicating the formation of foam texture (Figure 4.10 b).

There are also grains with serrated boundaries (Figure 4.10 c), and small, individual quartz grains (~10-20 µm) have developed along these boundaries (Figure 4.10 d). This indicates that recrystallization took place not only by subgrain rotation but also by grain boundary migration.

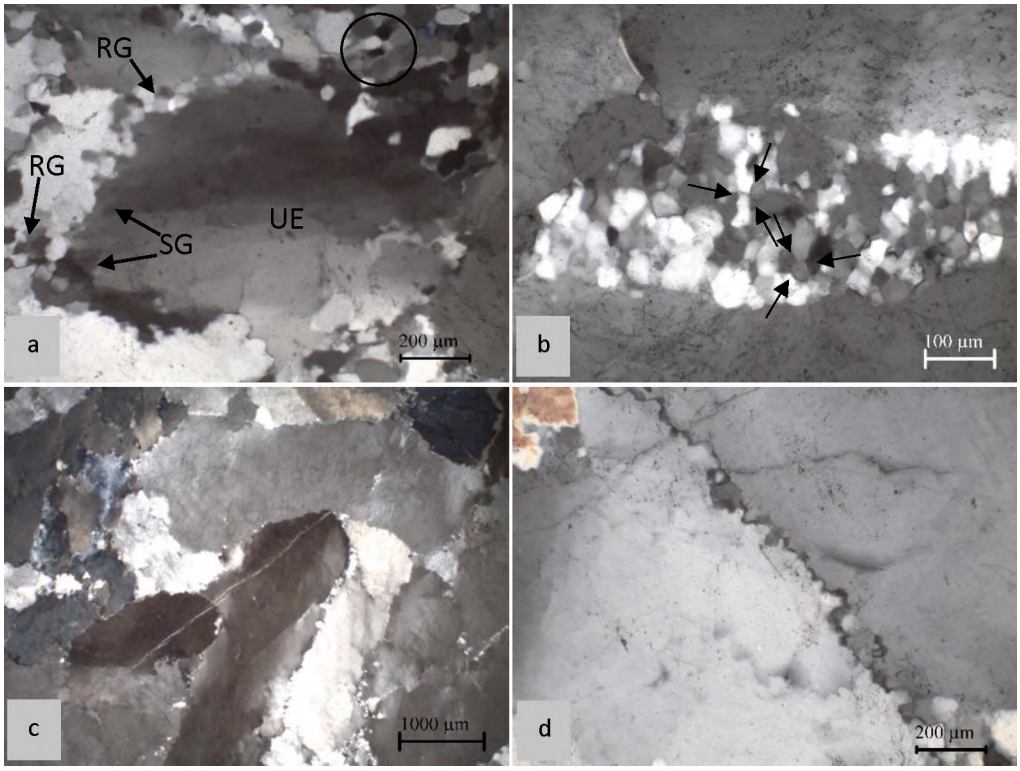

***Figure 4.10**: a) Grains in tension gash samples have undulose extinction (UE), which grades into subgrains (SG) and then recrystallized quartz grains (RG) (sample P5B, Outeniqua). The recrystallized grains have started to form foam texture, as indicated by the triple junction in the black circle. b) In places, the recrystallized grains form 120° triple junction boundaries, indicating the formation of foam texture (sample P16C, de Vlugt – Uniondale). c) Some grains have serrated grain boundaries (sample P16C). d) Along serrated grain boundaries, the presence of small quartz grains indicates recrystallization by grain boundary migration (sample P5B).*

4.6 Folds

The six samples from folded quartz veins (P5A from the Outeniqua Pass; P9A from the de Vlugt to Uniondale transect; and P17A, P18A, P18B and P18C from Meiringspoort) show different textural patterns.

The four Meiringspoort samples (P17A, P18A, P18B and P18C) show euhedral grain shapes (indicated by the presence of rhombohedral and prism planes, Figure 4.11 a & 4.11 b), which indicate that quartz grew and developed these crystal faces while growing into cavities filled with hydrothermal fluid. This former interstitial space has been filled with subsequent hydrothermal quartz or with chlorite (Figure 4.11 a). These quartz grains show minor undulose

extinction and minor subgrain formation (Figure 4.11 c), but do not show abundant evidence of more intense deformation. However, in places, particularly along the interface of two or three large quartz crystals in sample P17A, intense undulose extinction and subgrains grade into irregularly shaped recrystallized grains, indicating recrystallization. No foam textures are observed, suggesting that sufficiently high temperature did not outlast deformation for a substantial time period (Figure 4.11 d).

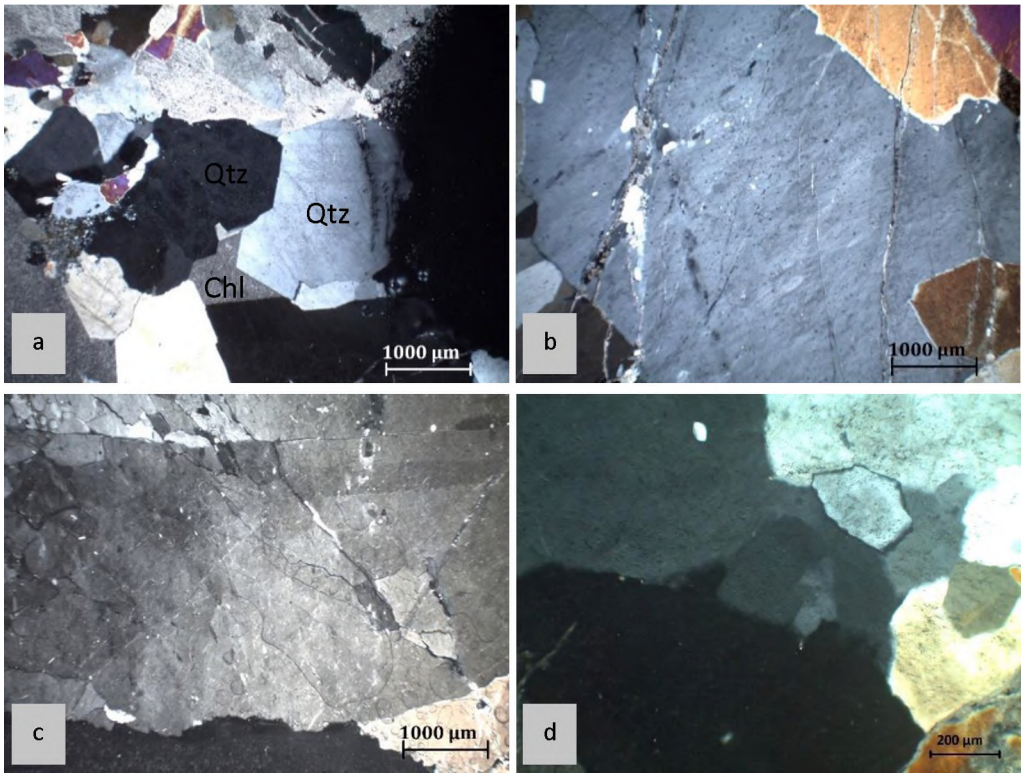

***Figure 4.11**: a) & b) Four of the six fold samples have euhedral grain shapes, shown here for example in a) sample P17A and b) P18B (both from Meiringspoort; Qtz = quartz; Chl = chlorite). c) Interstitial quartz grains show subtle undulose extinction and minor subgrain formation (sample P18C). d) In places, undulose extinction grades into subgrains, but does not reach the stage of intense recrystallization or foam texture formation (sample P17A).*

Substantial plastic deformation is not observed in the four Meiringspoort samples, although one would expect to see this in folded veins. It appears, however, that in the late stage of folding of initially planar veins new space was created in which quartz and, in places, chlorite precipitated. These new crystals then underwent minor deformation.

The other two fold samples, P5A (Outeniqua Pass) and P9A (de Vlugt – Uniondale transect), are more intensely deformed. Quartz shows strong undulose extinction, and serrated grain boundaries (Figure 4.12 a & b). Intense recrystallization is indicated in sample P5A by small, individual recrystallized grains replacing large primary hydrothermal grains (Figure 4.12 c), and which grade into domains showing foam texture (Figure 4.12 d).

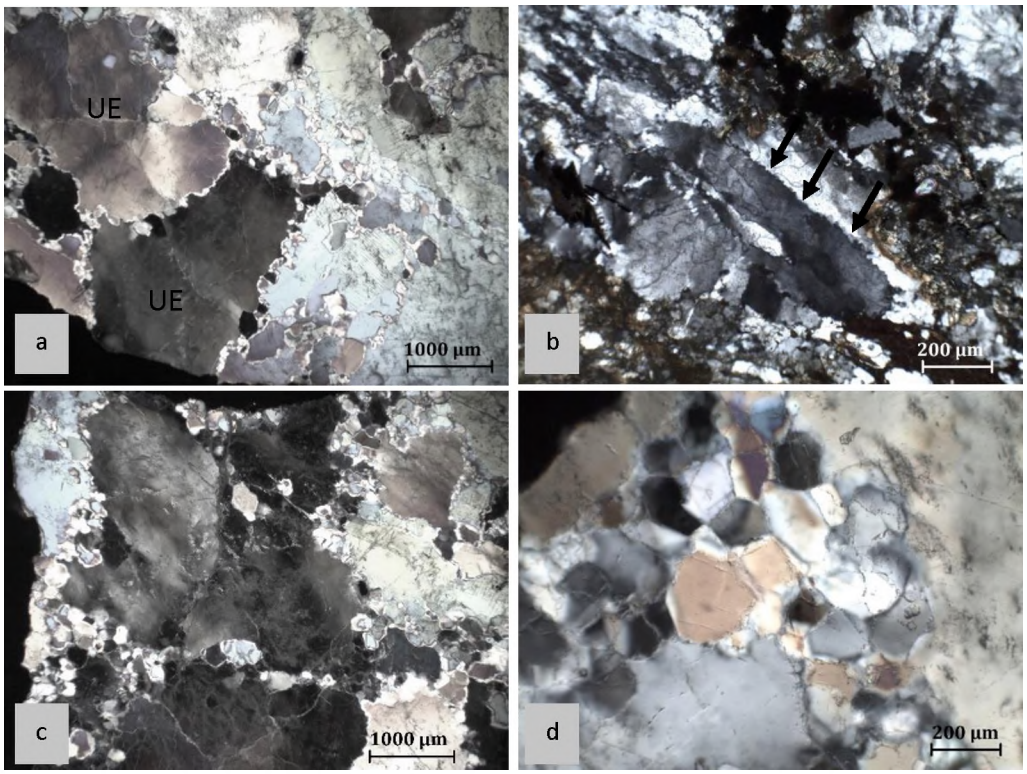

***Figure 4.12**: a) Sample P5A (Outeniqua) and b) sample P9A de Vlugt – Uniondale) both show undulose extinction (UE) and grains with serrated boundaries (indicated by arrows). c) Recrystallization leads to the formation of small, individual quartz grains which grade into domains of d) foam texture (sample P5A).*

Sample P9A also shows fine-grained (up to ~50 µm) quartz recrystallization by grain boundary migration (Figure 4.13 a). Other grains show fibrous quartz (Figure 4.13 b) with individual grains showing different crystal orientations, as indicated by highly variable extinction positions and interference colours. The orientation of quartz fibres is non-uniform, suggesting variable directions of vein opening during the evolution of the vein. This might, in this sample, be related to the folding process.

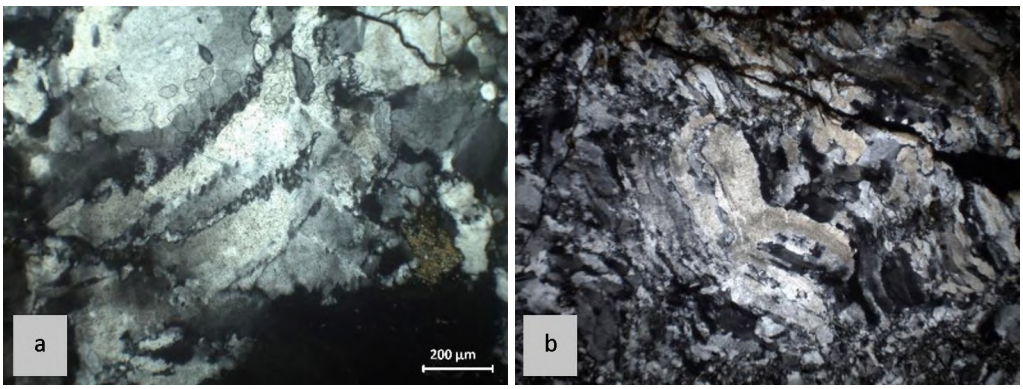

***Figure 4.13**: a) Recrystallization by grain boundary migration has occurred in fold sample P9A (de Vlugt – Uniondale). b) Elsewhere in sample P9A, fibrous quartz shows minor recrystallization along grain boundaries.*

4.7 Summary

For the most part, samples from different transects do not show significant differences in petrographic and deformation characteristics. Most samples show similar evidence of plastic deformation, including undulose extinction, formation of subgrains, and recrystallization. The exceptions to this trend are the thrust and fold samples from the Meiringspoort transect, which show less intense deformation than other samples, with larger grains and less recrystallization.

There are samples from each type of structure which show recrystallized grains, and hence deformation must have taken place under at least greenschist facies P-T conditions (Voll, 1976). However, an absence of abundant white mica neoblasts in the samples (and in the study area in general; Chapter 3) indicates that temperatures of the regional metamorphism, and hence deformation, are not likely to have exceeded ~440 °C. Above this temperature metamorphic white mica growth should be prominent in rocks of pelitic composition (Simpson et al., 2000).

5. FLUID INCLUSION CHARACTERISTICS

5.1. Fluid Inclusions

Fluid inclusions are fluid filled cavities in crystals. When a crystal grows in the presence of a fluid phase, some of the fluid may become trapped as a fluid inclusion in that crystal (Bodnar, 2003). Secondary fractures that may have formed during or after crystallization of a crystal may heal in the presence of fluid, which may be trapped as a fluid inclusion (Roedder, 1984). "Fluid inclusions provide one of the best tools available to constrain the pressure, temperature and fluid composition history of geological processes" (Roedder, 1984). Since fluid inclusions can form during or after crystal growth, they can record the conditions of several different deformation events which affected the crystal.

Fluid inclusions each act as geothermometers, recording the temperature of the fluid at the specific moment that the inclusion was sealed (Roedder, 1984). After trapping, on cooling, the fluid trapped as an inclusion tends to shrink far more than the cavity formed by the host mineral, and the difference in shrinkage leads to pressure changes, which may lead to the separation of a once primary phase into phases that are distinguishable by different physical state, such as liquid, gas or solid (Roedder, 1984). To work out the temperature at which the fluid was first trapped as a homogeneous fluid, the process of cooling can be reversed by heating the inclusion until the phases homogenise (Roedder, 1984).

The pressure of the environment of trapping can also be obtained from fluid inclusions, through a variety of procedures based on experimental data (Roedder, 1984). Similarly, density of the fluid in the inclusion can be obtained and can provide valuable information about circulation of fluids in the crust at the time of trapping (Roedder, 1984).

Finally, the composition of the fluid inclusion can be obtained through either observing phase behaviour at different temperatures, or, more accurately, by Raman spectroscopy. Raman spectroscopy allows the identification of major fluid components such as H_2O, CO_2, CH_4, N_2, and others. Laser ablation ICP-MS analysis allows the quantitative measurement of individual major, minor and trace elemental concentrations (e.g. Günther et al., 1998), but this technique is analytically challenging and only few laboratories (e.g., ETH Zürich, Leeds) have successfully executed such analysis. None of these laboratories is located in South Africa.

This chapter summarises petrographic characteristics of FIs, such as FI shape (see chapter 2), size, type (L + V, V + L, etc.; see chapter 2), composition, temperature of final melting (T_m), and temperature of homogenisation (T_h). Results of heating-cooling experiments, and fluid compositions are also presented in this chapter.

Fluid compositions were determined by Raman Spectroscopy. Compounds of interest were H_2O, CO_2 and CH_4, and, as no other compounds were detected, only H_2O, CO_2 and CH_4 are discussed.

The observed characteristics presented in this chapter will be applied to various methods to find bulk fluid compositions, fluid salinities, fluid densities, and trapping temperatures and pressures. The results of those thermometric estimations will be presented in Chapter 6.

5.2 Thrust faults

Table 5.1 summarises the properties of primary and secondary inclusions in thrust faults. The following subsections will discuss the composition and physical properties of these inclusions in terms of FI generation (primary and secondary).

Table 5.1: Summary of fluid inclusion characteristics for thrust faults.

	Primary FIs		**Secondary FIs**	
Number of samples	12		7	
Occurrence	Narrow arrays		Arrays along fractures	
Size	Majority ≤2-6 µm, up to ~26 µm		≤2-10 µm	
Shape	Elongate and equant		Elongate, equant, irregular	
Type	L + V		L + V	
Composition	H_2O-NaCl	H_2O-NaCl-CO_2	H_2O-NaCl	H_2O-NaCl-CO_2
Number of inclusions	121	135	42	14
T_i (°C)	-6.5 – -1	-5 – -1	-8 – -1	-6.5 – -3
T_m (°C)	-4 – 0	-4 – 0	-3 – 0	-3 – 0
Phase separation (T_h (CO_2)) (°C)	NA	7 – 12	NA	9 – 12
T_h (°C)	130 – 190 [1]	140 – 240 [2]	130 – 170 [3]	130 – 160

[1] 78% of the data are within this range, but there are outliers from 110 – 280 °C.
[2] 85% of the data are within this range, but there are outliers from 140 – 300 °C (Figure 5.2).
[3] 84% of the data are within this range, but there are outliers from 110 – 190 °C.

5.2.1 Primary inclusions

Primary fluid inclusions generally occur as planar arrays of small to medium sized inclusions. Inclusions larger than ~8 µm occur as isolated single inclusions or form small clusters (2-5 FIs). The majority of primary inclusions range from <2 µm up to ~6 µm, but larger FIs, up to ~15 µm, are common. Inclusions larger than 15 µm are rare, but may reach up to ~26 µm (sample P23A).

Most commonly, primary fluid inclusions show elongate and equant shapes (Figure 5.1) but irregular and negative crystal shapes may also occur. No conical inclusions were found. The large majority of primary inclusions are liquid-rich, two-phase inclusions with a vapour component (L + V; Figure 5.1), with a gas content (φ_{gas}) of up to 30 vol% at room temperature. There are rare gas-rich, two-phase inclusions as well, with gas volume fractions between 50-60 vol% at room temperature. Monophase liquid inclusions also occur.

Raman spectroscopy reveals two types of primary inclusions – one in which the gas and liquid contain H_2O + NaCl, and another which contains CO_2 gas and saline liquid (for example, Figure 5.2). H_2O-NaCl and CO_2-containing primary inclusions show initial melting (T_i) at -6.5 – -1 °C and -5 – -1°C respectively, and both show final melting (T_m) at -4 to 0 °C.

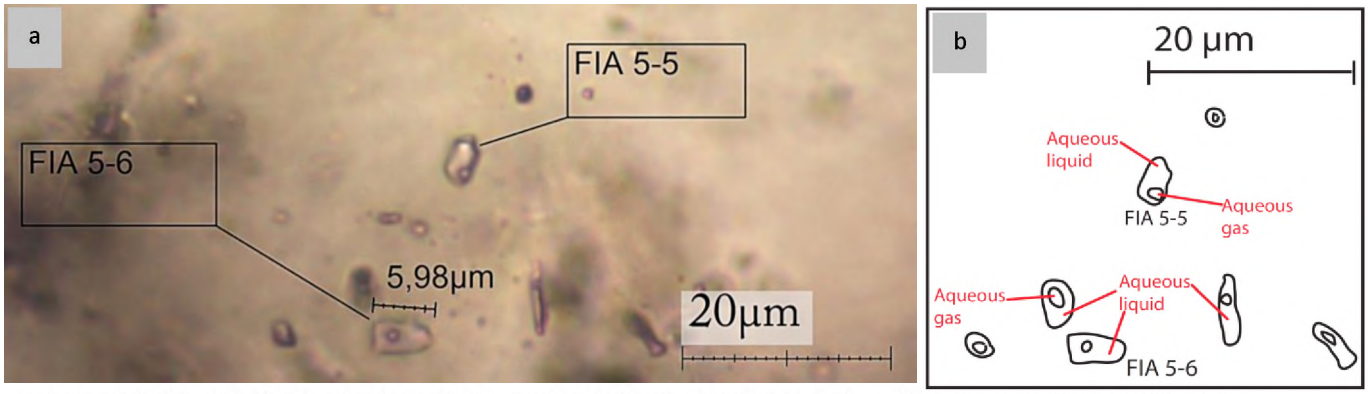

***Figure 5.1**: Fluid inclusions in thrust faults are typically elongate or equant, with gas content of up to 30 vol% at room temperature. An example is shown here in a) a photomicrograph and b) a sketch of FIs from Fluid Inclusion Assemblage (FIA) 5 in sample P19A.*

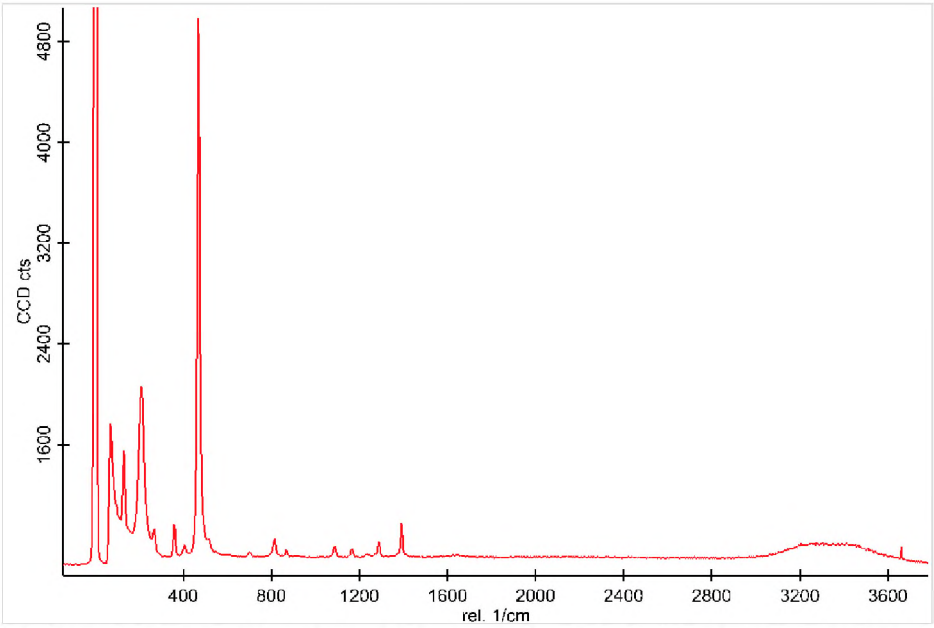

***Figure 5.2**: The Raman spectrum for an exsolved CO_2 bubble in a fluid inclusion in sample in P20A shows CO_2 peaks at 1285 and 1388 cm^{-1}, and a broad H_2O peak over 3219 cm^{-1}.*

H_2O-NaCl primary inclusions homogenise to liquid at 130-190 °C. CO_2-bearing primary inclusions show phase separation ($T_h(CO_2)$) between 7-12 °C, at which CO_2 separates from the liquid and forms a separate bubble. CO_2-bearing inclusions homogenise at a higher temperature interval than that of H_2O-NaCl inclusions, at T_h = 140 – 240 °C, with a roughly normal distribution about the 190 – 200 °C range (Figure 5.3).

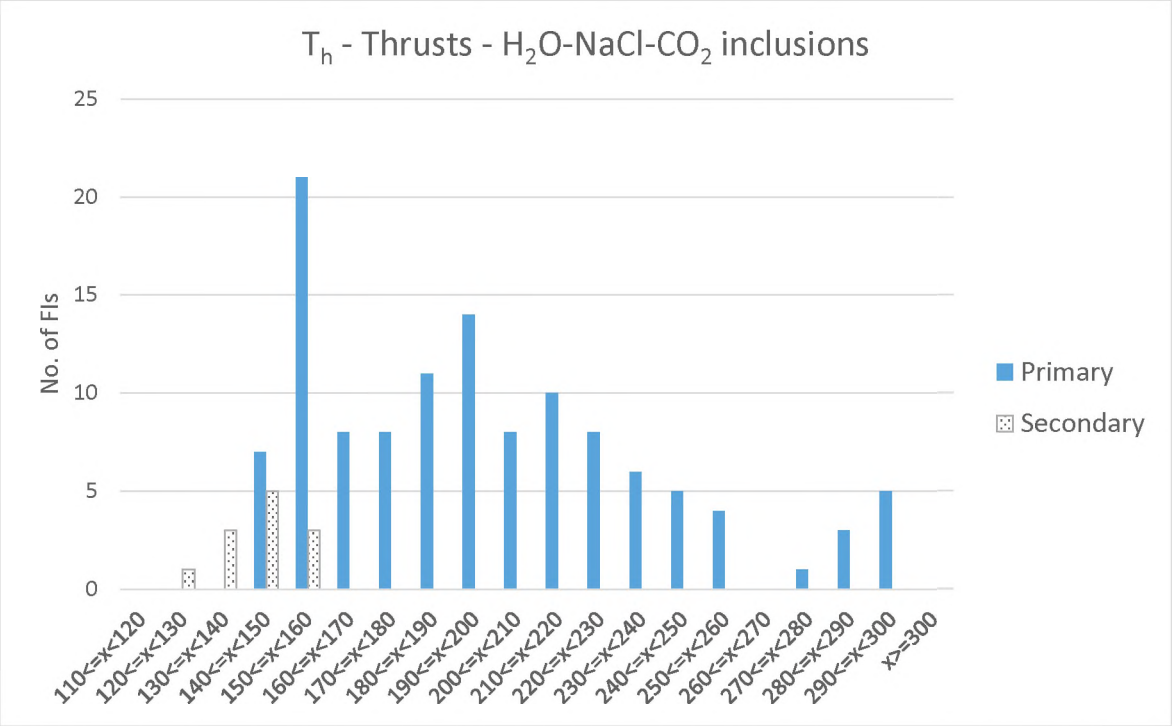

***Figure 5.3**: Histogram of the T_h ranges for CO_2-bearing inclusions in thrust faults. 85% of the readings for primary inclusions fall within 140 – 240 °C, forming a roughly normal distribution about the 190 – 200 °C range.*

5.2.2 Secondary Inclusions

Secondary inclusions are fairly common in thrust faults, occurring as arrays along healed fractures. The inclusions are up to ~10 µm in size but the majority of inclusions are smaller than 2 µm and therefore not large enough for meaningful thermometrical analysis (Figure 5.4). In roughly equal proportions secondary inclusions are either elongate, equant or irregularly shaped. There are a few negative crystal shapes as well, but no conically shaped inclusions.

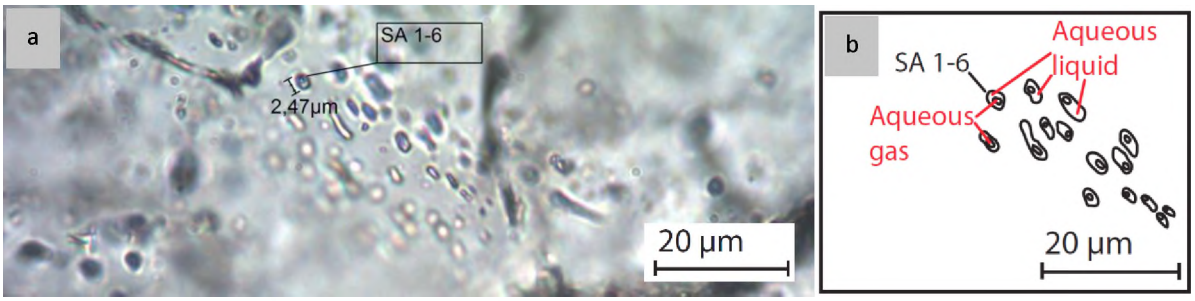

***Figure 5.4**: Secondary inclusions in quartz-filled thrust faults are typically very small, and are typically elongate, equant or irregularly shaped. An example is shown here in a) a photomicrograph and b) a sketch of FIs from Secondary Array (SA) 1 in sample P6A.*

Like primary inclusions, most secondary fluid inclusions are liquid-rich, two-phase inclusions (L + V), with gas volume percentages of 10 – 20% at room temperature. Raman spectroscopy shows there are two types of secondary inclusions (as with primary inclusions). Secondary

fluid inclusions contain H_2O-NaCl as well as H_2O-NaCl-CO_2, which is the same composition seen in primary inclusions.

T_i is between -4 – -1 °C, and T_m ranges from -3 to 0 °C in both NaCl-H_2O and CO_2-bearing secondary inclusions. T_h of both inclusion types is, however somewhat lower than seen in primary inclusions (Table 5.1). H_2O-NaCl secondary inclusions homogenise to liquid at 130 – 170 °C, and CO_2-bearing secondary inclusions have a slightly narrower T_h range of 130 – 160 °C. The CO_2-bearing inclusions show phase separation ($T_h(CO_2)$) between 10 – 13.5 °C, at which CO_2 separates from the liquid and forms a separate bubble.

5.3 Reverse faults

Primary and secondary inclusions in reverse faults (samples P10A, P21A and P22A) are very similar to each other in most aspects. Only the T_h range differs slightly. Table 5.2 summarises the properties of primary and secondary inclusions in reverse faults.

Table 5.2: Summary of fluid inclusion characteristics for reverse faults.

	Primary FIs	**Secondary FIs**
Number of samples	3	2
Occurrence	Abundant arrays	Wide arrays along fractures
Size	≤2-4 µm	≤2-5 µm
Shape	Elongate and equant (± irregular)	Equant and elongate
Type	L + V	L + V
Composition	H_2O-NaCl	H_2O-NaCl (CO_2 in P21A)
Number of inclusions	56	20
T_i (°C)	-5 – -1	-4 – -1
T_m (°C)	-2.5 – 0	-2.5 – 0
Phase separation (T_h (CO_2)) (°C)	NA	10 – 13.5
T_h (°C)	150 – 210	150 – 180

5.3.1 Primary inclusions

Primary fluid inclusions typically occur in planar arrays, which are so numerous and narrowly spaced that in places they become indistinguishable from each other (Figure 5.5 a). Fluid inclusions are abundant in the reverse fault samples, but are typically smaller than ~2 µm in size, and therefore too small for analysis. Most textural observations and thermometric data were obtained from inclusions of 2 – 4 µm in size. Larger inclusions of 4 – 7 µm are rare, occurring only in sample P21A from the Kango inlier.

Inclusions are typically equant or elongate shaped (Figure 5.5 b & c). They are commonly mono- or two-phase inclusions, with gas volume proportions of 5 – 30% at room temperature, though there are rare vapour rich inclusions as well, with up to 70 vol% gas.

Raman spectroscopy shows that primary inclusions from reverse faults contain only H_2O-NaCl liquid and gas; neither CO_2 nor CH_4 was detected. T_i for the inclusions is between -5 – -1 °C, and T_m ranges from -2.5 – 0 °C. The inclusions homogenise to liquid at 150 – 210 °C.

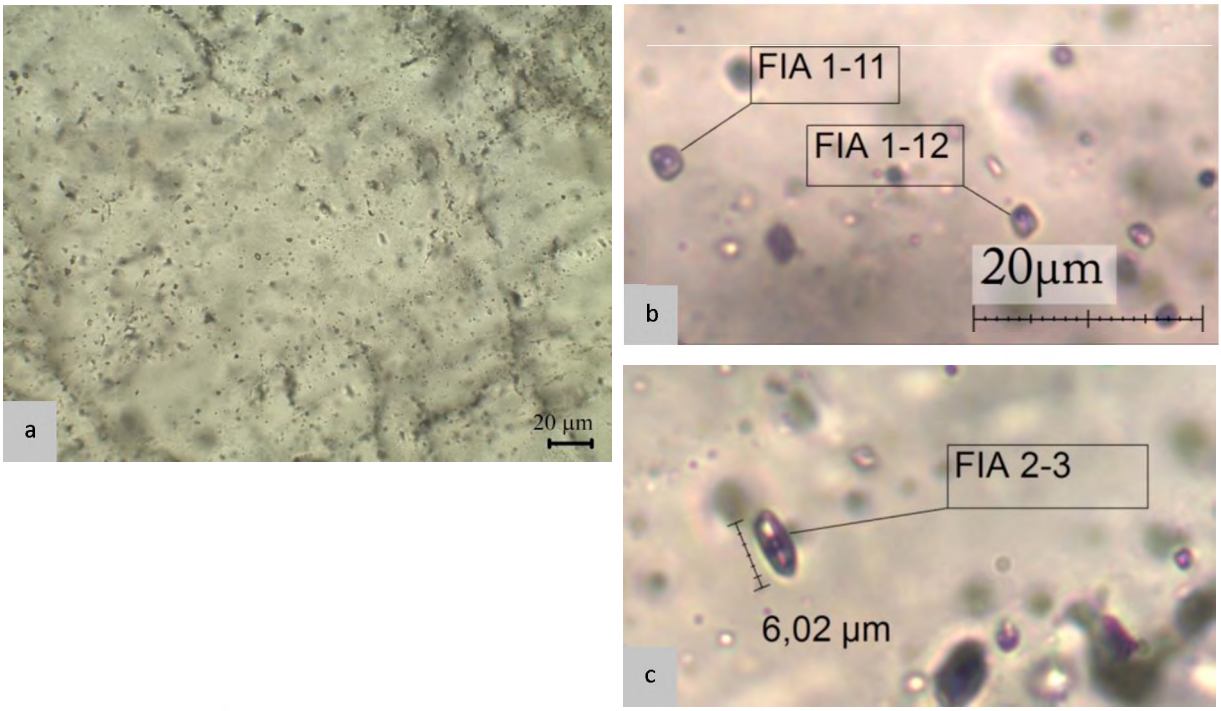

***Figure 5.5**: a) Inclusion arrays in sample P10A are so narrowly spaced that it is difficult to distinguish different arrays or assemblages from each other. b) Inclusions are typically equant, for example FIA 1 in P21A, or c) elongate, for example FIA 2 in sample P21A.*

5.3.2 Secondary inclusions

Secondary inclusions are common in reverse fault samples, but are mostly <2 µm. Inclusions of ~2 – 5 µm occur in clear, wide arrays along healed fractures. Secondary inclusions are elongate or equant in shape (Figure 5.6). All FIs are either liquid-rich two-phase inclusions with gas proportions of 10 – 20 vol%, or monophase liquid inclusions.

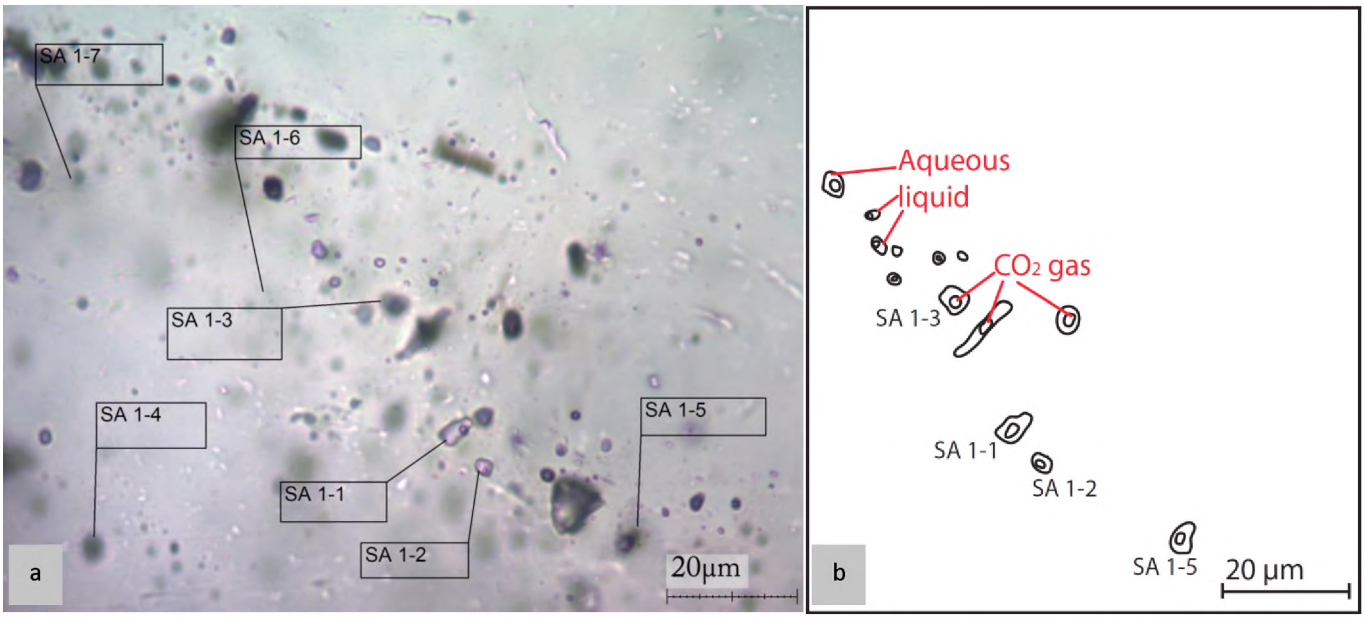

***Figure 5.6**: Secondary inclusions in reverse faults that are larger than ~2 µm occur in wide arrays along healed fractures, shown here for example in a) a photomicrograph and b) a sketch of SA 1 from sample P21A. FIs are generally elongate (e.g. SA 1-1) or equant (e.g. SA 1-2) in shape.*

One analysed secondary array shows CO_2 (sample P21A from the Pan-African basement in the Kango Inlier, Figure 5.7). All other samples show H_2O+NaCl in gas and liquid of secondary fluid inclusions. There is, however, no significant difference in the T_h of inclusions with or without CO_2 – both homogenise to liquid between 150 and 180 °C (Table 5.2), and the CO_2-bearing inclusions show phase separation between 10 – 13.5 °C (Table 5.2). The initial melting temperature for secondary inclusions is -4 – -1 °C, while the final melting temperature range is -2.5 – 0 °C (Table 5.2).

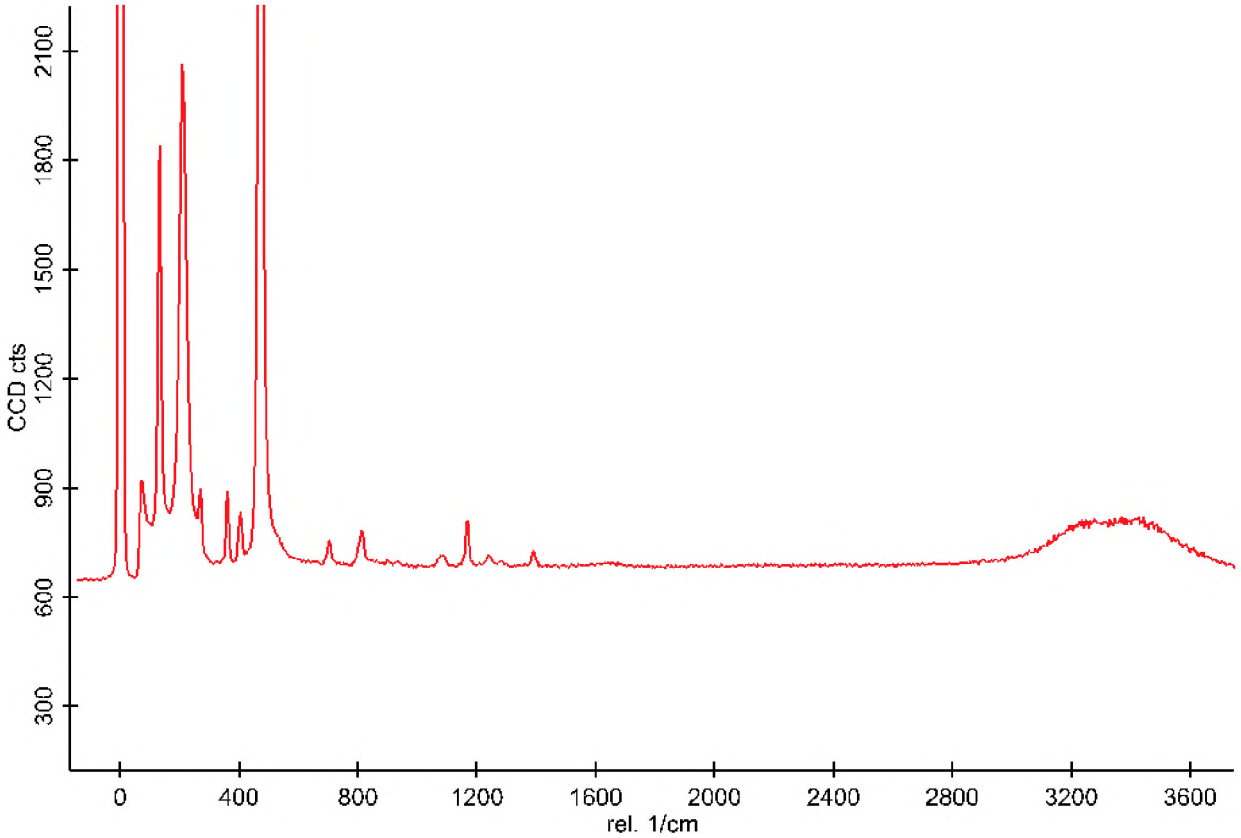

***Figure 5.7**: The Raman spectrum for the liquid in a fluid inclusion in sample in P21A shows CO_2 peaks at 1285 and 1388 cm^{-1}, and a broad H_2O peak over 3219 cm^{-1}.*

5.4 Normal faults

Inclusions from normal fault samples (P23B and P24A) were found to contain CO_2 and CH_4, and have higher T_h ranges than samples from other structures. Table 5.3 summarises the properties of primary and secondary inclusions in normal faults.

Table 5.3: Summary of fluid inclusion characteristics for normal faults.

	Primary FIs	**Secondary FIs**
Number of samples	2	2
Occurrence	Short, distinct arrays	Longer, wide arrays
Size	≤2-6 µm	≤2-6 µm
Shape	Elongate and equant (± conical)	Elongate
Type	L + V	L + V
Composition	H_2O-NaCl-CO_2-CH_4	H_2O-NaCl-CO_2 ± CH_4
Number of inclusions	42	28
T_i (°C)	-4.5 – -1.5	-4 – -1
T_m (°C)	-4 – 0	-3 – 0
Phase separation (T_h (CO_2)) (°C)	8.5-13	7-12
T_h (°C)	210 – 250 and 280 – 300 [1]	160 – 200 [2]

[1] 90% of the data are within these ranges, but there are outliers from 160 – 260 °C.
[2] 85% of the data is within this range, but there are outliers between 200 – 240 °C.

5.4.1 Primary inclusions

Primary inclusions in normal faults generally occur in short, distinct, and randomly oriented arrays. Inclusions are common, but small. Inclusions larger than ~6 µm are rare in normal fault samples. Elongate and equant are the most common shapes for primary inclusions, but conical, negative crystal and irregular shapes occur as well.

Inclusions are typically two-phase and liquid-rich, with gas proportions of 10 – 30 vol%. Gas-rich inclusions are rare, and show 50 to 60 vol% gas at room temperature. Raman spectroscopy shows H_2O + NaCl and CO_2 in the gas and the liquid phases. In addition, the gas phase contains some CH_4 (Figure 5.8).

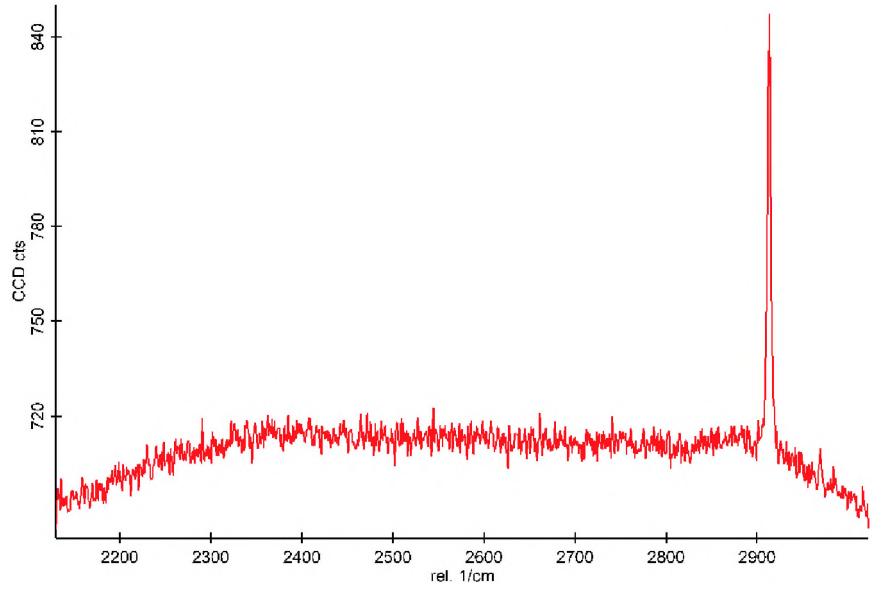

***Figure 5.8**: The Raman spectrum for the gas phase in a fluid inclusion in sample P23B shows a CH_4 peak at 2917 cm^{-1}.*

Primary inclusions have an initial melting temperature range of -4.5 – -1.5 °C, and a final melting temperature between -4 and 0 °C. Primary inclusions homogenise to liquid over two ranges: 210 – 250 °C and 280 – 300 °C (Figure 5.9). The higher readings come from sample P24A, but it is not clear why the higher range occurs. Both samples are from Meiringspoort, and both are from the Peninsula Formation. Phase separation ($T_h(CO_2)$) occurs between 8.5 and 13 °C, at which the CO_2 separates from the liquid and forms a bubble.

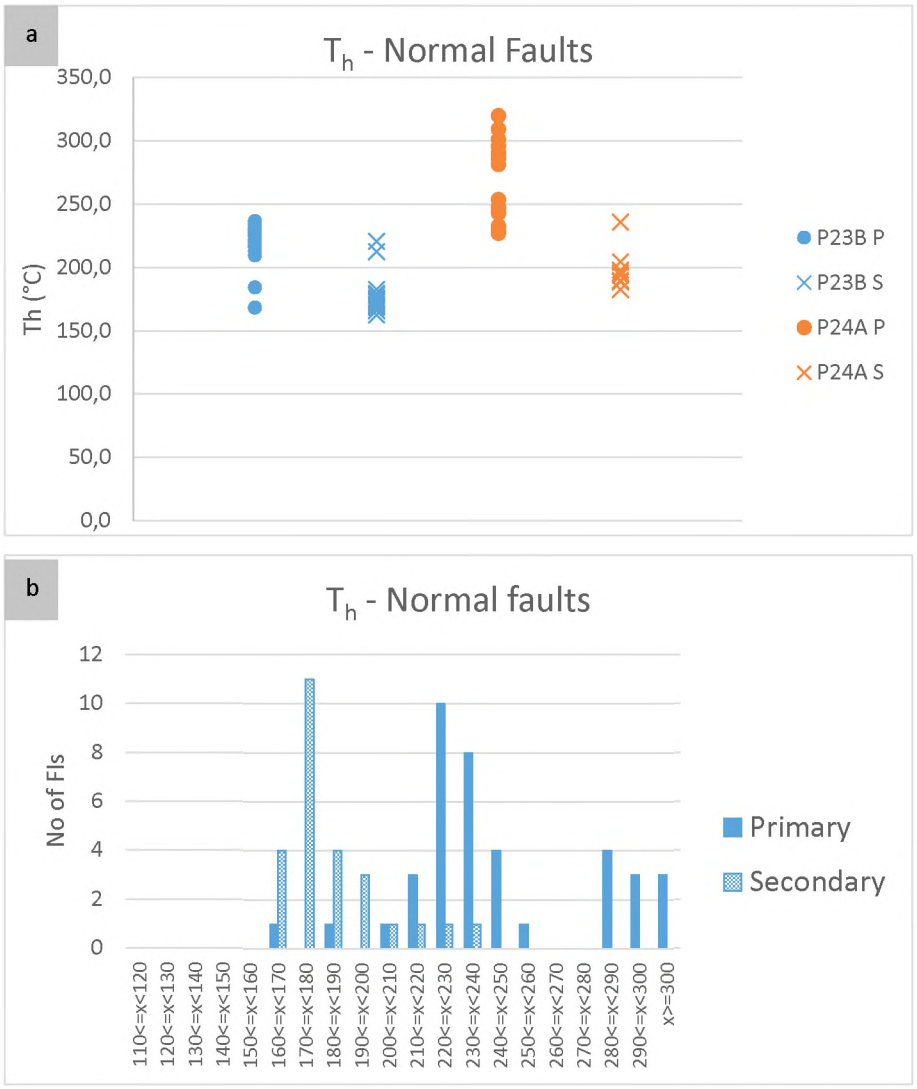

***Figure 5.9**: a) Scatter plot showing T_h for inclusions in normal fault samples, sorted by sample and with primary (P) and secondary (S) inclusions separated. b) Histogram showing the temperature of homogenisation for inclusions in normal fault samples. Ranges in which there is only one reading are excluded. Readings above 280°C come only from sample P24A, but there are also readings in the lower ranges from sample P24A.*

5.4.2 Secondary inclusions

Secondary inclusions also occur in arrays along healed fractures that tend to be longer and wider than arrays formed by primary inclusions. Elongate inclusions are by far the most common (Figure 5.10), but negative crystal, equant, irregular and conical inclusions are also present. Secondary inclusions are a similar size to the primary inclusions, ranging between ≤2 to ~6 µm. Gas-rich, two-phase inclusions are dominant, with 10 – 30 vol% gas. Monophase

liquid inclusions also occur in normal fault samples. Secondary inclusions in sample P23B contain H_2O+NaCl, CO_2, and CH_4, but the secondary inclusions from sample P24A contain only H_2O+NaCl and CO_2.

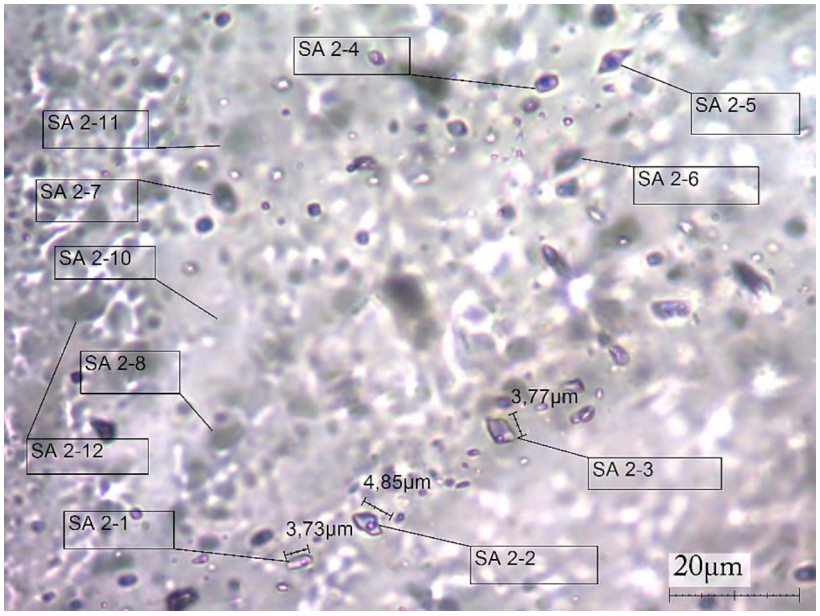

***Figure 5.10**: Secondary inclusions occur in wide arrays, and elongate FIs are most common. Secondary inclusions in normal fault samples range in size from ≤2 µm to ~6 µm (e.g. SA 2 in sample P23B.)*

The initial melting temperature range for secondary inclusions is -4 – -1 °C, and the final melting temperature for secondary inclusions is between -3 and 0 °C, one degree higher than T_m for primary inclusions. Phase separation occurs between 7 – 12 °C. The T_h range for secondary inclusions is 160 – 200 °C, and FIs containing CH_4 homogenise in the lower part of this interval (~160 – 180 °C). Where CH_4 is absent, T_h ranges between ~180 – 200 °C. Overall the T_h of secondary FIs is somewhat lower than of primary FIs (Table 5.3).

5.5 Oblique- and strike-slip faults

Table 5.4 summarises the characteristics of the 39 primary inclusions in oblique-slip and strike-slip faults samples (P12A and P16A). No secondary inclusions were analysed in these samples.

Table 5.4: Summary of fluid inclusion characteristics for oblique and strike-slip faults.

	Primary FIs	**Secondary FIs**
Number of samples	2	NA
Occurrence	Abundant, short arrays	
Size	≤3-7 µm	
Shape	Elongate (±equant & irregular)	
Type	L + V	
Composition	H_2O+NaCl-CO_2	
Number of inclusions	39	
T_i (°C)	-6.5 – -1	
T_m (°C)	-4 – 0	
Phase separation (T_h (CO_2)) (°C)	8 – 14	
T_h (°C)	130 – 170[1]	

[1] 76% of the data is within this range, but there are outliers from 110 – 200 °C.

5.5.1 Primary inclusions

Primary inclusions are abundant in samples P12A and P16A. Inclusions ≥2 µm are not common but, in places, the FI size may exceed ~7 µm. Inclusions mostly occur in planar arrays, but also in small clusters of three to six inclusions (Figure 5.11). Elongate inclusions are the most common, but equant and irregular shapes occur as well. Inclusions are either monophase or liquid-rich two-phase, the latter comprising of only 5-10 vol% gas.

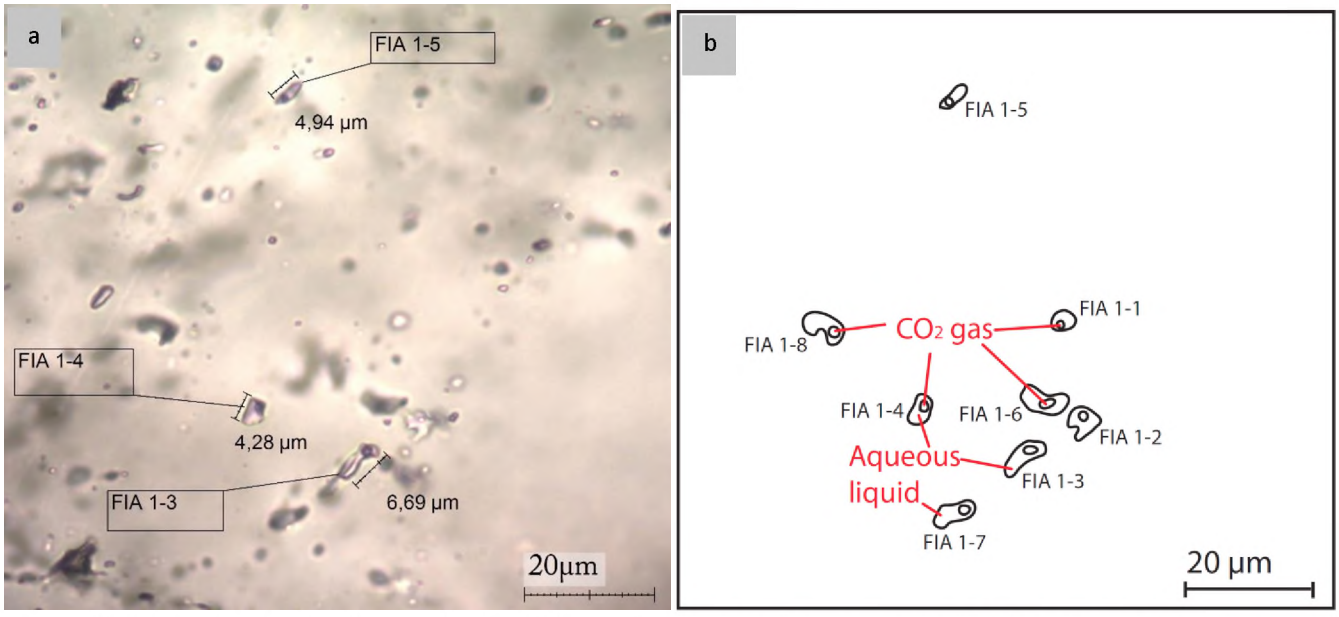

***Figure 5.11**: Primary inclusions from strike-slip fault samples occur in planar arrays or small clusters, as shown here in a) a photomicrograph and b) a sketch of FIA 1 from sample P12A. Elongate inclusions are most common.*

Raman spectroscopy shows that the inclusions consist of H_2O+NaCl and CO_2 in the gas and liquid phases. T_i for primary inclusions is -6.5 – -1 °C, and the final melting temperature (T_m) is between -4 to 0 °C. Phase separation ($T_h(CO_2)$) in primary inclusions occurs between 8 and 14 °C, and the inclusions homogenise to liquid at 130 – 170 °C (Table 5.4).

5.5.2 Secondary inclusions

Although secondary inclusions are abundant in these samples – occurring in narrow arrays – none were found that were large enough to analyse.

5.6 Tension gashes

Table 5.5 summarises the properties of primary and secondary inclusions in tension gash samples.

Table 5.5: Summary of fluid inclusion characteristics for tension gashes.

	Primary FIs		**Secondary FIs**	
Number of samples	4		2	
Occurrence	Abundant arrays		Narrow, distinct arrays	
Size	≤2-6 μm		≤2-5 μm	
Shape	Elongate		Elongate	
Type	L + V		L + V	
Composition	H_2O+NaCl	H_2O+NaCl-CO_2-CH_4	H_2O+NaCl	H_2O+NaCl-CO_2
Number of inclusions	49	35	10	10
T_i (°C)	-6 – -1.5	-5.5 – -1	-3.5 – -1	-4 – -1
T_m (°C)	-4 – 0	-4 – 0	-1.5 – 0	-2 – 0
Phase separation (T_h (CO_2)) (°C)	NA	9 – 14 °C	NA	10 – 12 °C
T_h (°C)	155 – 195 & 235 – 265[1]	260 – 290[2]	150 – 175[3]	180 – 220

[1] 82% of the data are within these ranges, but there are outliers between 140 – 270°C.
[2] 87% of the data is within this range, but there are outliers from 290 – 310°C.
[2] 90% of the data is within this range, but there are outliers from 140 – 150°C.

5.6.1 Primary inclusions

Primary fluid inclusions are common in samples from tension gashes and are typically very small (<1μm) to medium sized (~6 μm), although there are some rare large inclusions (up to ~12μm). Inclusions tend to occur in short, isolated arrays, which are randomly oriented. Elongate, equant and irregularly shaped inclusions occur in roughly equal proportions, and negative crystal and conical shapes occur in much smaller proportions.

The majority of inclusions are two-phase, liquid-rich, with 10-40 vol% gas. Vapour-rich inclusions occur as well (φ_{gas} up to ~60%). Raman spectra in one tension gash sample, P5B, show CH_4 as well as H_2O+NaCl in primary inclusions (Figure 5.12). The other three samples contain only H_2O+NaCl primary inclusions.

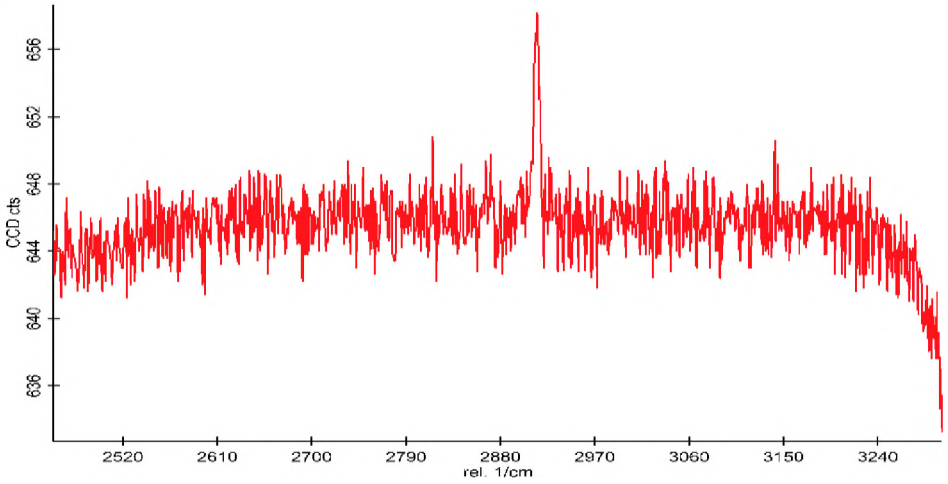

***Figure 5.12**: The Raman spectrum for an exsolved bubble in a fluid inclusion in sample P5B shows a CH_4 peak at 2917 cm^{-1}.*

The homogenisation temperatures in FIs from tension gashes show some variety. Phase separation on CO_2-bearing inclusions occurs between 9-14 °C. The CH_4 bearing inclusions in sample P5B have a T_h range of 260 – 290°C. This range is higher than the T_h range for H_2O+NaCl inclusions in samples P16C and P19B, which is 155 – 195°C. Although inclusions from P16B also contain only H_2O-NaCl, they have a higher T_h range (than those in P16C and P19B) of 235 – 265°C (Table 5.5). Although the homogenisation temperatures are quite variable, primary FIs in tension gashes all show an initial melting temperature between -6 and -1 °C, and a final melting temperature range of -4 to 0°C (Table 5.5).

5.6.2 Secondary inclusions

Secondary inclusions which are large enough to analyse are rare in tension gash samples, occurring in only two of the four samples (P5B and P16C). The rarely observed maximum size is ~5µm. These larger FIs occur as distinct arrays along healed fractures. Like secondary inclusions in other structures, the majority of inclusions are too small for analysis, and only five FIs are ≥4µm. Secondary inclusions are exclusively elongate or equant shapes.

The inclusions that are large enough to analyse are all two-phase, liquid-rich, with 10 – 20 vol% gas. Raman spectra of secondary FIs in P5B show H_2O+NaCl, CO_2 and CH_4, while secondary inclusions from P16C consist of only H_2O+NaCl.

H_2O-NaCl secondary inclusions have an initial melting temperature between -3.5 – -1 °C and a final melting temperature between -1.5 and 0 °C. H_2O-NaCl-CO_2 secondary inclusions have an initial melting temperature between -4 – -1 °C and a final melting temperature between -2 and 0 °C. The CO_2-bearing inclusions have a slightly higher T_h range (180 – 200 °C) than those that do not contain CO_2 (145 – 175 °C; Table 5.5). The CO_2-bearing inclusions also have a marginally higher T_m range (-2 – 0 °C) than those without CO_2 (-1.5 – 0 °C).

5.7 Folded veins

Fluid inclusions are fairly common in fold samples, occurring in abundant arrays, but out of six samples taken from folds, only one, sample P18A, shows primary inclusions large enough to analyse. No secondary inclusions were found that were large enough to analyse. Table 5.6 summarises the properties of primary and secondary inclusions in fold samples.

Table 5.6: Summary of fluid inclusion characteristics for folds.

	Primary FIs	**Secondary FIs**
Number of samples	1	NA
Occurrence	Abundant arrays	
Size	≤2 to 10 µm	
Shape	Elongate + equant	
Type	L + V	
Composition	H_2O+NaCl	
Number of inclusions	24	
T_m (°C)	-3 – 0	
T_h (°C)	150 – 180[1]	

[1] 82% of the data is within this range, but there are outliers from 120 – 190 °C.

5.7.1 Primary inclusions

In sample P18A, primary inclusions are rare, but can be quite large, reaching up to ~10µm in length. The predominant shapes are elongate and equant, though there are also some irregular shaped inclusions (Figure 5.13). Most inclusions are liquid-rich two-phase, with gas volume proportions of 10-20% at room temperature, though monophase liquid inclusions do occur as well.

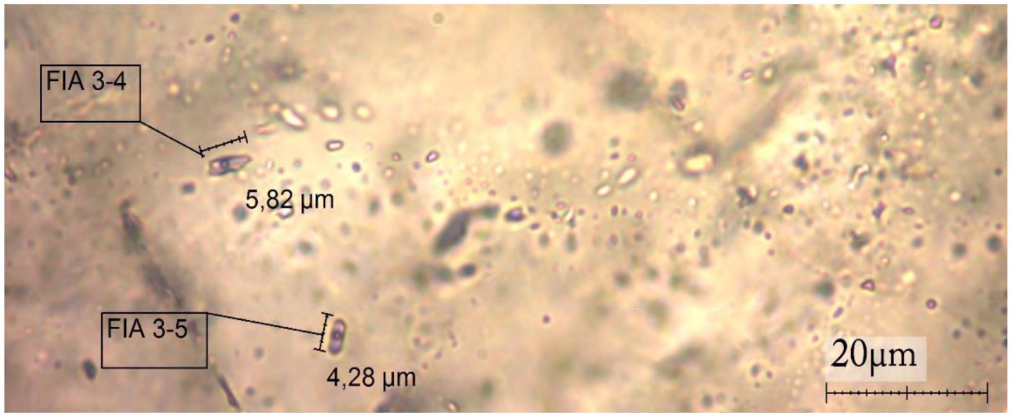

***Figure 5.13**: Primary inclusions from fold sample P18A occur in abundant arrays, and are generally elongate or equant.*

Raman spectra of P18A show H_2O+NaCl in the liquid and gas phase (Figure 5.14). Inclusions homogenise to liquid over a T_h range of 150-180 °C, and have a final melting temperature range of -3 to 0 °C.

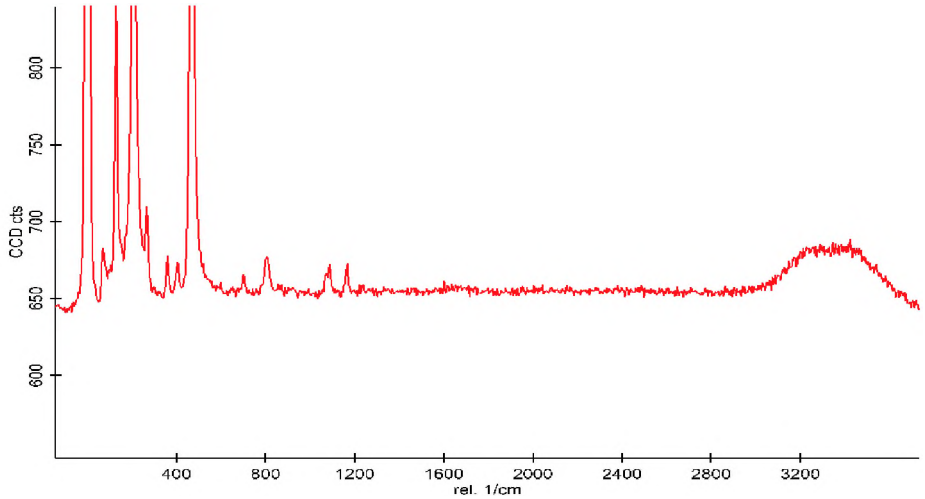

***Figure 5.14**: The Raman spectrum for an exsolved bubble in a fluid inclusion in sample P18A shows a broad H_2O peak at 3219 cm^{-1}.*

5.7.2 Secondary inclusions

Although secondary inclusions in folded quartz veins are common – occurring in long, narrow arrays – none were found that were large enough for thermometric analysis.

5.8 Summary

Most fluid inclusions (primary and secondary) are two-phase inclusions and liquid rich, while gas-rich inclusions are rare in all structures. The most common fluid composition is H_2O-NaCl, occurring in all samples. CH_4, on the other hand, is rare, occurring only in the normal fault samples (primary and secondary) and one tension gash sample (P5B, primary inclusions only). Secondary inclusions are rare in all structures, and tend to be much smaller than primary inclusions.

The temperature of final melting (T_m) of primary and secondary fluids differs very little across different structures. There is also very little difference between inclusions containing CO_2 and those without CO_2. Temperature of homogenisation (T_h) is similar for thrusts, reverse faults, strike- and oblique-slip faults, and folds. Primary H_2O-NaCl inclusions show T_h between ~130 and 200 °C, and H_2O-NaCl-CO_2 inclusions have slightly higher T_h, between ~140 and 240 °C. Secondary inclusions in all structures have a similar T_h range to primary inclusions, but have a lower maximum T_h (~130-180 °C). Inclusions containing CH_4 have the highest T_h (~210-300 °C).

6. MICROTHERMOMETRY

This chapter contains the results and evaluation of the fluid inclusion microthermometric data presented in Chapter 5. The physical and chemical properties in analysed fluid inclusions are summarised in Table C1 (Appendix C) and Table D1 (Appendix D). The fluids in the analysed fluid inclusions are assumed to be representative of the fluids present at the time of entrapment.

The observed microthermometric data, such as homogenisation or phase separation temperatures ($T_h(CO_2)$), will be applied to various methods that convert them into fluid trapping temperatures or pressures. Some methods yield unrealistic P_t or T_t results, which are nevertheless presented here. In the Discussion section (Chapter 7) the results presented here will be evaluated and interpreted.

For hydrous saline fluids, the salinities were calculated according to Bodnar's (1993) equation of state using the melting point depression:

$$Salinity\ (wt\%) = 0.00 + 1.78\theta - 0.0442\theta^2 + 0.000557\theta^3, \quad (1)$$

where θ is the depression of the freezing point in degrees Celsius.

For fluids containing CO_2 or CH_4, salinities were calculated using the FLUIDS software (Bakker, 2003).

From these salinities, and the T_h ranges obtained from microthermometry, the fluid density was determined graphically from the density contour diagrams of a vapour-saturated saline fluid (e.g. Figure 6.1; Bodnar, 1983; Roedder, 1984). The graphically determined densities are consistent with the results from the FLUIDS software (Bakker, 2003). The density of CO_2-bearing fluids was determined using pressure contours for the system CO_2 in the low-temperature range (e.g. Figure 6.3). Since this system only applies to CO_2-H_2O fluids which are NaCl-free, the density of CO_2 bearing fluids (which also contain NaCl) were determined using FLUIDS software (Bakker, 2003).

The CO_2 and H_2O-NaCl fluid densities allow the plotting of density isochore intersections in P-T space (e.g.; Figure 6.4), and the pressure estimation using T_h and CO_2 density according to Kalyuzhnyi and Koltun (1953; not seen, as reported in Roedder, 1984; e.g. Figure 6.5).

In inclusions containing only saline hydrous fluid, pressure correction factors allow the estimation of trapping temperatures from the salinity and temperature of homogenisation (Potter, 1977; e.g. Figure 6.25). This method does not apply to inclusions which contain anything other than a pure NaCl solution (Roedder, 1984).

In addition, in samples where CH_4 is present, pressure of trapping can be determined graphically from Raman spectroscopy peaks for CH_4 (Seitz et al., 1993; Theiu et al., 2000; e.g. Figure 6.13).

6.1 Thrust faults

Raman spectroscopy shows two groups of fluid inclusions in thrust fault-bound vein quartz: (i) primary and secondary inclusions containing H_2O and NaCl in aqueous solution; and (ii) primary and secondary inclusions containing aqueous saline liquid with a CO_2 gas phase. The results and evaluations of microthermometric data for thrust faults are summarised in Table 6.1.

Table 6.1: Summary of evaluation of microthermometric data for thrust faults. These have been determined using FLUIDS software (Bakker, 2003).

		Primary FIs		**Secondary FIs**	
Type		H_2O-NaCl	H_2O-NaCl-CO_2	H_2O-NaCl	H_2O-NaCl-CO_2
Average salinity (wt% NaCl equivalent)		2.8	2.7	2.2	2.6
Average bulk fluid composition	X(H_2O)	0.982792	0.949065	0.984583	0.954944
	X(Na^+/Cl^-)	0.008604	0.008212	0.007709	0.007862
	X(CO_2)	NA	0.034510	NA	0.029333
Average fluid density (g/cm^3)		0.92	0.88	0.94	0.94

6.1.1 H_2O-NaCl Inclusions

From 163 readings in 12 thrust fault samples from across the study area, the salinity calculation suggests similarly low salinity ranges of 0-6 wt% NaCl equivalent (avg. 2.8 wt%; Table 6.1) in primary FIs, and 0-5.5 wt% NaCl equivalent (avg. 2.2 wt% NaCl equivalent) in secondary inclusions. The salinity ranges do not vary across the study area (Figure 6.1 a-d) and nowhere exceed 6 wt% NaCl equivalent.

From these salinities, and the T_h ranges for thrust faults, the fluid density was determined as 0.87-0.97 g/cm^3 (average = 0.92 g/cm^3) in primary and 0.9-0.97 g/cm^3 (average = 0.94 g/cm^3) in secondary inclusions. Salinities and T_h values in all investigated thrusts are similar to each other, and, accordingly, the fluid densities do not vary between samples from the Outeniqua, de Vlugt – Uniondale, and Meiringspoort sections (Figure 6.1 a-c). Secondary fluids might have a slightly higher density than primary ones (e.g. in the Meiringspoort transect, Figure 6.1 c), but this variation is very small and is regarded as insignificant.

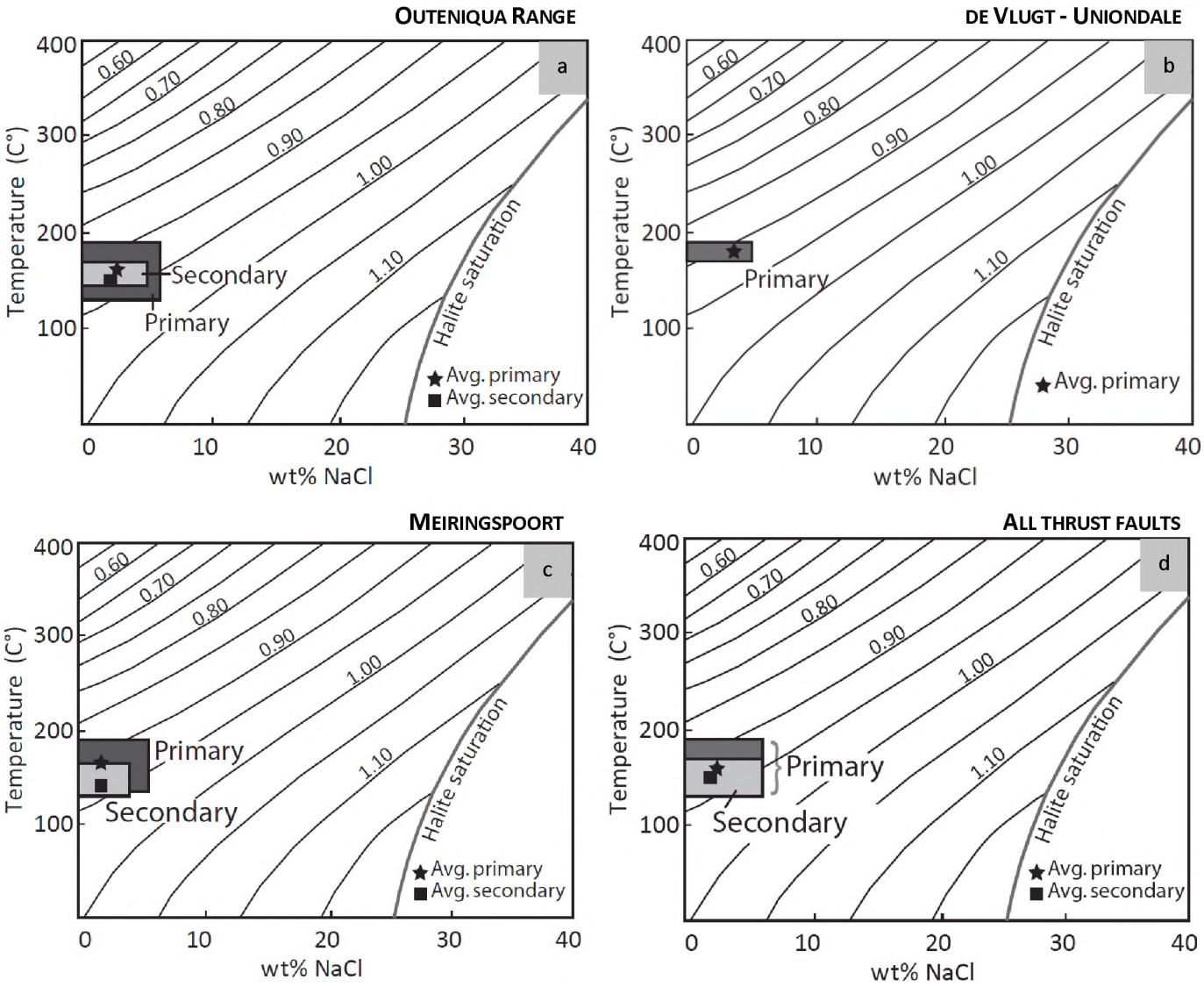

***Figure 6.1**: Density contours for a vapour-saturated saline fluid in the system H_2O-NaCl, depending on temperature of homogenisation (T_h) and salinity (modified after Bodnar, 1983; Roedder, 1984), for thrust faults in a) the Outeniqua transect, b) the de Vlugt – Uniondale transect, c) the Meiringspoort transect, and d) all thrust fault samples. Overall, thrust fault fluids have salinities ≤6wt% NaCl equivalent, and an average T_h range of 130 – 190 °C in primary and 130 – 170 °C in secondary fluids. The corresponding densities range between ~0.90 and 0.95 g/cm³ for primary and secondary inclusion fluids. The individual ranges for the Outeniqua, de Vlugt – Uniondale and Meiringspoort fluids do not differ from each other significantly, and are adequately represented in diagram d).*

Thrust sample P19A is from the Boplaas Formation in the Bokkeveld Group, further up in the CSG stratigraphy than the majority of thrust samples (Figure 7.1). This sample contains only H_2O-NaCl fluid inclusions, and the fluid salinity is somewhat lower than the average of the other Meiringspoort samples (primary fluid salinity = 0-3.5 wt% NaCl equivalent; secondary fluid salinity = 0-1.8 wt% NaCl equivalent). From these salinities, and the T_h ranges for primary and secondary fluids (primary T_h = 135-160 °C; secondary T_h = 120-145 °C), the fluid density for this sample was determined as 0.90-0.95 g/cm^3 for primary fluids and 0.93-0.95 g/cm^3 for secondary fluids (Figure 6.2).

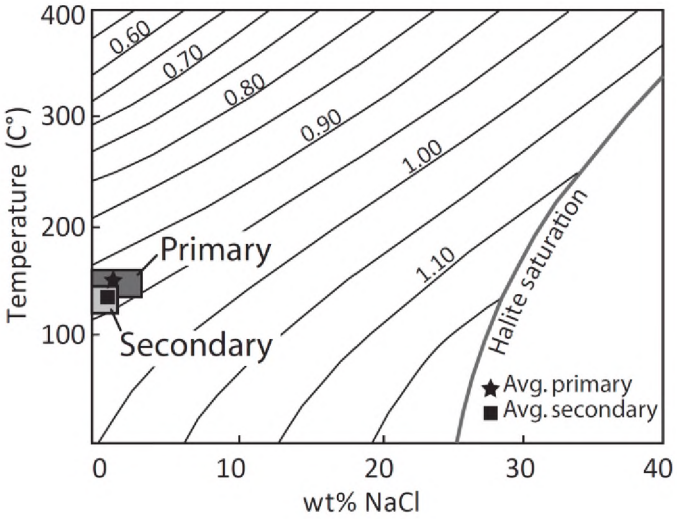

***Figure 6.2**: Density contours for a vapour-saturated saline fluid in the system H_2O-NaCl, depending on temperature of homogenisation and salinity (modified after Bodnar, 1983; Roedder, 1984), for thrust fault sample P19A from the Boplaas Formation in the Bokkeveld Group. A salinity of ≤3.5 wt% NaCl equivalent and a T_h range of 135-160 °C corresponds to fluid density of 0.90-0.95 g/cm³ for primary fluids. A salinity of ≤1.8 wt% NaCl equivalent and a T_h range of 120-145 °C shows a fluid density of 0.93-0.95 g/cm³ for secondary fluids.*

Because this sample is associated with a fold, the trapping temperature (T_t) must have been at least 300 °C. In absence of CO_2 in the fluids, the pressure of trapping can only be inferred from the H_2O-NaCl isochore. Due to its steep slope and its position, the 0.90-0.95 g/cm³ isochore (e.g., Figure 6.25) reaches temperatures exceeding 300 °C only at pressures of ~200 MPa. The minimum trapping conditions for P19A are therefore ~200 MPa and ~300 °C, which, at an average rock density of 2600 g/cm³, corresponds to a depth of 7900 m and a geothermal gradient of 38 °C/km.

6.1.2 H_2O-NaCl-CO_2 Inclusions

Fluid salinities for CO_2-bearing fluids can be determined from the FLUIDS software (Bakker, 2003). Primary fluids have a salinity range of 0-4.1 wt% NaCl equivalent, (average = 2.7 wt% NaCl equivalent), while secondary fluid salinity ranges between 0-2.8 wt% NaCl equivalent, with an average of 2.6 wt% NaCl equivalent.

The CO_2-bearing inclusions in thrust faults show phase separation ($T_h(CO_2)$) of CO_2 vapour and liquid in the range 7-12 °C for primary inclusions and 9-12 °C for secondary inclusions (Table 5.1). Although the CO_2-bearing inclusions are not completely NaCl-free, the salinities are very low, and fluid densities have been determined using pressure contours for the system CO_2 in the low-temperature range (Figure 6.3). A fluid density of 0.83-0.87 g/cm³ (average = 0.84 g/cm³) can be determined for the CO_2-component in primary H_2O-NaCl-CO_2 inclusions. H_2O-NaCl-CO_2 fluids from secondary inclusions have a slightly narrower range of 0.83-0.85 g/cm³ (average = 0.83 g/cm³). FLUIDS software (Bakker, 2003) yielded slightly higher densities for CO_2-bearing inclusions (Table 6.1): Primary H_2O-CO_2-NaCl inclusions have an average density of 0.88 g/cm³ (ranging from 0.79 to 0.93 g/cm³), while secondary inclusions have an average density of 0.95 g/cm³. For the purpose of further calculations, the FLUIDS results are used (Table 6.1).

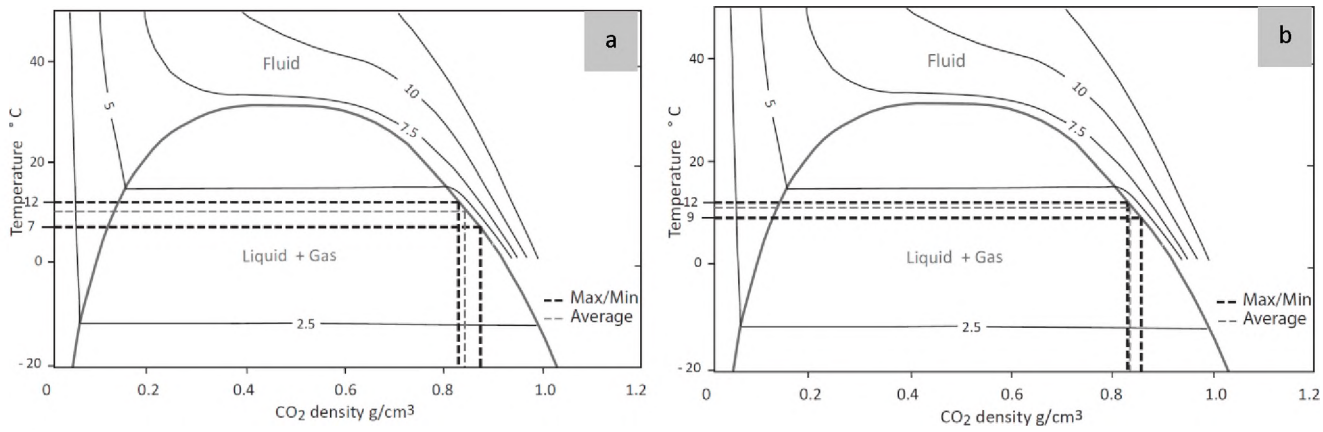

***Figure 6.3**: Temperature – density plot for the system CO_2, showing pressure contours and phase boundaries (modified after Roedder, 1984). a) In primary fluids in thrust fault samples, vapour-liquid separation occurs between 7 and 12 °C, corresponding to CO_2 densities of 0.83 to 0.87 g/cm³ (average = 0.84 g/cm³). b) In secondary fluids, vapour-liquid separation between 9 and 12 °C suggests a slightly narrower range for CO_2 densities of 0.83 to 0.85 g/cm³ (average = 0.83 g/cm³).*

H_2O-NaCl and CO_2 isochore intersection diagrams can be done for Samples P23A and P23D, which were taken from the same outcrop and therefore assumed to be cogenetic (Figure 6.4). The diagrams suggest a pressure and temperature of entrapment of 175 MPa and ~300 °C for primary inclusions (Figure 6.4 a), and ~105 MPa and ~230 °C for secondary inclusions (Figure 6.4 b). The conditions for entrapment of primary fluids are very close to the 46 °C/km maximum geothermal gradient proposed by Büttner et al. (2016). Those for the secondary fluids fall on a much higher, much less likely, geothermal gradient. However, the intersection of the isochores is at a very high angle, and there may therefore be a high degree of analytical error.

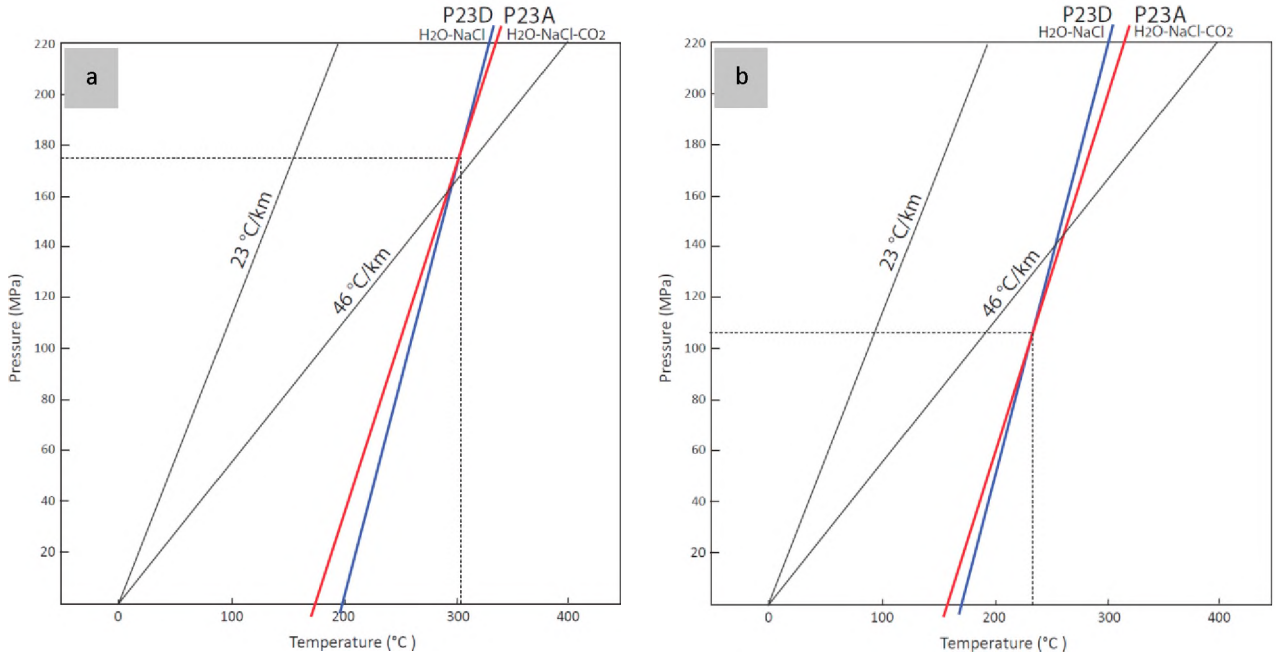

***Figure 6.4**: Iso-density (isochore) lines for H_2O-NaCl (blue) and H_2O-NaCl-CO_2 (red) inclusions in thrust fault samples P23A and P23D (modified after Kalyuzhnyi and Koltun, 1953; Roedder, 1984). Geothermal gradients of 23 °C/km (e.g. Allen and Allen, 1990) and 46 °C/km (Büttner, et al. 2016) have been added for comparison. a) P-T conditions of entrapment for primary inclusions are ~175 MPa and ~300 °C. b) P-T conditions of entrapment for secondary inclusions are ~105 MPa and 230 °C.*

Pressure of entrapment of primary CO_2-bearing fluids can also be determined from CO_2 pressure contours (Figure 6.5). An average fluid density of 0.88 g/cm^3 and 0.94 g/cm^3 for primary and secondary fluids respectively (Table 6.1), in conjunction with maximum T_h of 240 °C and 160 °C (Table 5.1) yields fluid pressures of ~170 MPa for primary fluids (very close to the result obtained from the CO_2-H_2O isochore intersection) and ~120 MPa for secondary fluids (approximately 15 MPa higher than the result obtained from the CO_2-H_2O isochore intersection). However, the diagram in Figure 6.5 assumes pure CO_2 fluids, and the observed fluids contain as little as 3% CO_2 (Table 6.1). Therefore, the similarity of the pressures might be coincidental. However, the best interpretation for average conditions of primary fluid entrapment in thrust faults is about 240-300 °C and 170-175 MPa. Assuming an average density of the overlying rock column of 2600 kg/m^3 at the time of deformation, these conditions imply a depth of ~6800 m at a geothermal gradient of ~33-44 °C/km.

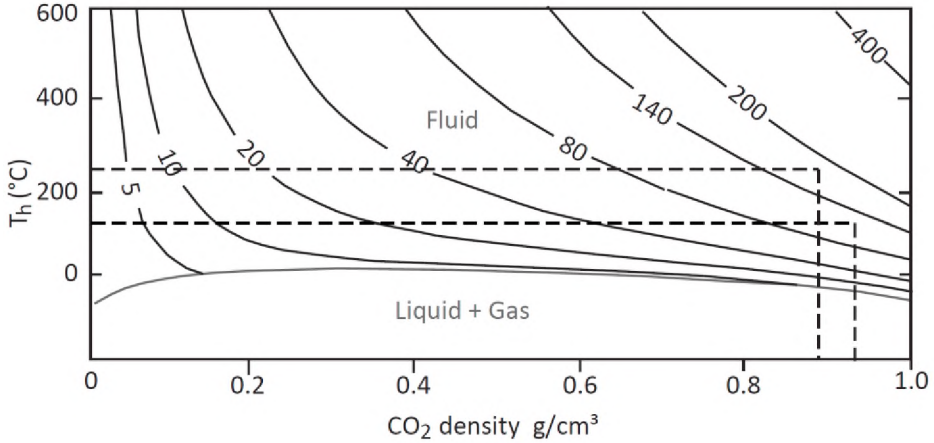

***Figure 6.5**: Pressure contours of CO_2 fluid, dependant on T_h and density (modified after Roedder, 1984). The maximum T_h and average density for primary and secondary inclusions in thrust faults corresponds to fluid pressures of ~170 MPa and ~120 MPa respectively.*

6.2 Reverse faults

Reverse fault primary inclusions contain only H_2O-NaCl aqueous solution. There are two types of secondary inclusions: (i) secondary inclusions containing H_2O and NaCl in aqueous solution, and (ii) secondary inclusions from sample P21A from the Kango inlier containing CO_2 as well as H_2O-NaCl. The results and evaluations of microthermometric data for reverse faults are summarised in Table 6.2.

Table 6.2: Summary of evaluation of microthermometric data for reverse faults. These have been determined using FLUIDS software (Bakker, 2003).

		Primary FIs	**Secondary FIs**	
Type		H_2O-NaCl	H_2O-NaCl	H_2O-NaCl-CO_2
Average salinity (wt% NaCl equivalent)		2.3	2.9	1.8
Average bulk fluid composition	X(H_2O)	0.985665	0.981883	0.956662
	X(Na^+/Cl^-)	0.007167	0.009059	0.005295
	X(CO_2)	NA	NA	0.032749
Average fluid density (g/cm^3)		0.92	0.92	0.91

6.2.1 H_2O-NaCl Inclusions

The salinity of primary and secondary inclusion fluids is uniformly low and does not exceed 4 wt% NaCl equivalent. The T_h range for primary fluids (150-210 °C) is slightly broader than for secondary fluids (160-180 °C; Table 5.2). T_h and salinity ranges correspond to a fluid density of 0.85-0.95 g/cm^3 for primary fluids (average = 0.91 g/cm^3), and a narrower range of 0.9-0.93 g/cm^3 for secondary fluids (average = 0.92 g/cm^3; Figure 6.6). These results are similar to those found using FLUIDS software (Bakker, 2003).

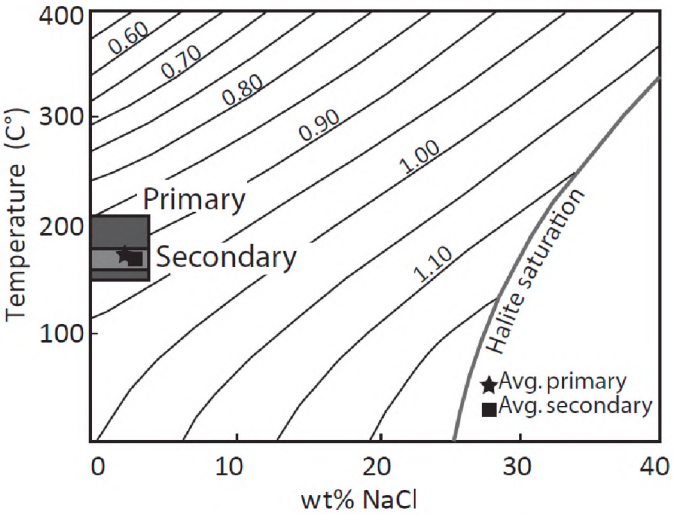

***Figure 6.6**: Density contours for a vapour-saturated saline fluid in the system H_2O-NaCl, depending on temperature of homogenisation and salinity (modified after Bodnar, 1983; Roedder, 1984), for reverse fault samples. A salinity of ≤4 wt% NaCl equivalent and a T_h range of 150-210 °C corresponds to fluid density of 0.85-0.95 g/cm^3 for primary fluids. The same salinity but a narrower T_h range for secondary fluids shows a fluid density of 0.9-0.93 g/cm^3.*

6.2.2 H_2O-NaCl-CO_2 Inclusions

In reverse faults, only secondary fluids contain H_2O-NaCl-CO_2. These inclusions have an average salinity of 1.8 wt% NaCl equivalent (Table 6.2), and show phase separation ($T_h(CO_2)$) of CO_2 vapour and liquid in the range 10-13.5°C (Table 5.2). According to the CO_2 phase diagram, this corresponds to a fluid density of 0.81-0.85 g/cm^3 (average = 0.83 g/cm^3; Figure 6.7,). The average fluid density can also be determined using FLUIDS software (Bakker, 2003). Secondary CO_2-bearing fluids in reverse faults have an average density of 0.91 g/cm^3 (Table 6.2).

The pressures of entrapment for secondary fluids can be determined from CO_2 pressure contours (Figure 6.8). A maximum T_h of 170 °C (Table 5.2) and an average CO_2 density of 0.91 g/cm^3 (Table 6.2) for secondary inclusions yields a fluid pressure of ~130 MPa. As in Figure 6.5, the diagram in Figure 6.9 assumes pure CO_2 fluids, and the observed fluids contain as little as 3% CO_2 (Table 6.1), and there are therefore some limitations on the result.

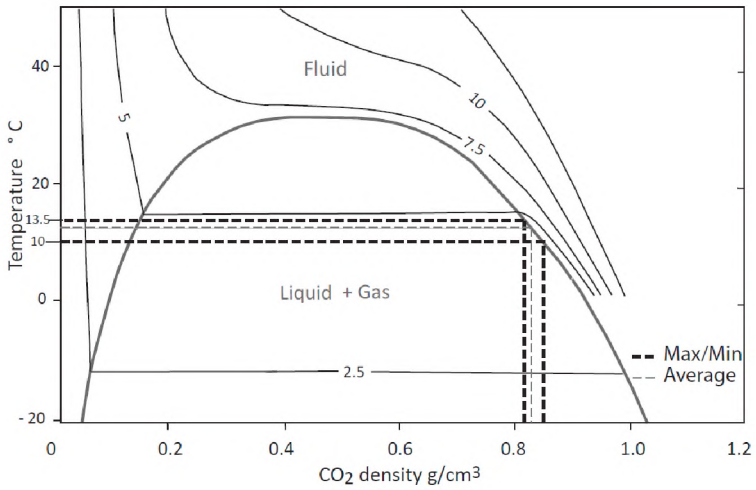

***Figure 6.7**: Temperature – Density plot for the system CO_2, showing pressure contours and phase boundaries (modified after Roedder, 1984). In secondary inclusions in reverse fault samples, vapour-liquid separation occurs between 10 and 13.5°C. This corresponds to a CO_2 density of 0.81-0.85 g/cm³. The average CO_2 density is 0.83 g/cm³.*

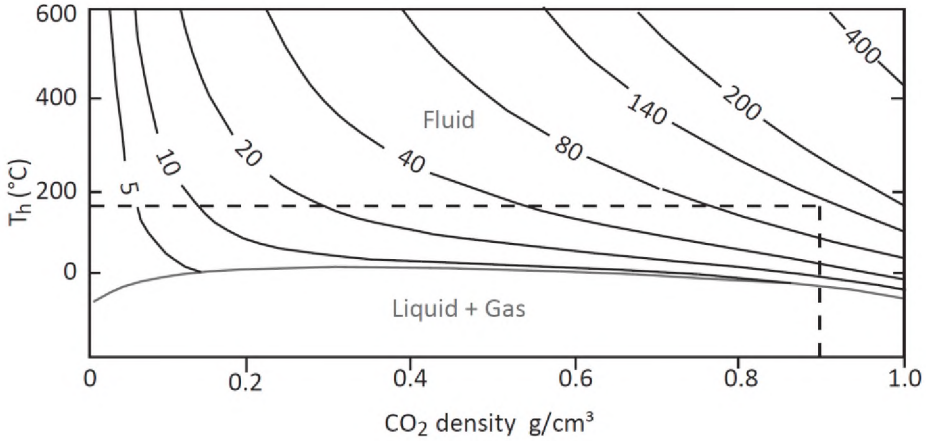

***Figure 6.8**: Pressure contours of CO_2 fluid, dependant on T_h and density (modified after Roedder, 1984). The maximum T_h and average density for secondary H_2O-NaCl-CO_2 inclusions in reverse faults corresponds to fluid pressure of ~130 MPa.*

6.3 Normal faults (H_2O-NaCl-CO_2-CH_4)

The two analysed normal fault samples (P23B and P24A) show H_2O-NaCl-CO_2-CH_4 in primary and in secondary fluids. The results and evaluations of microthermometric data are summarised in Table 6.3.

Table 6.3: Summary of evaluation of microthermometric data for normal faults. These data have been determined graphically and using FLUIDS software (Bakker, 2003).

	Primary FIs	**Secondary FIs**
Type	H_2O-NaCl-$CO_2 \pm CH_4$	H_2O-NaCl-$CO_2 \pm CH_4$
Average salinity (wt% NaCl equivalent)	2.7	2.1
Average fluid density (g/cm³)	0.75 & 0.85	0.9

Normal fault primary inclusion fluids have a salinity of 0-6 wt% NaCl equivalent (average = 2.7 wt% NaCl equivalent; Table 6.3), and secondary fluids have a salinity of 0-5 wt% NaCl equivalent (average = 2.1 wt% NaCl equivalent; Table 6.3). For primary inclusions, there are two ranges of T_h for (210-250 °C and 280-300 °C). The resulting H_2O fluid density for primary inclusions forms two ranges of 0.7-0.8 g/cm^3 and 0.78-0.9 g/cm^3, with averages of 0.75 and 0.85 g/cm^3 respectively (Figure 6.9; Table 6.3). For secondary fluids, the density is 0.86-0.95 g/cm^3, with an average of 0.9 g/cm^3 (Figure 6.9; Table 6.3).

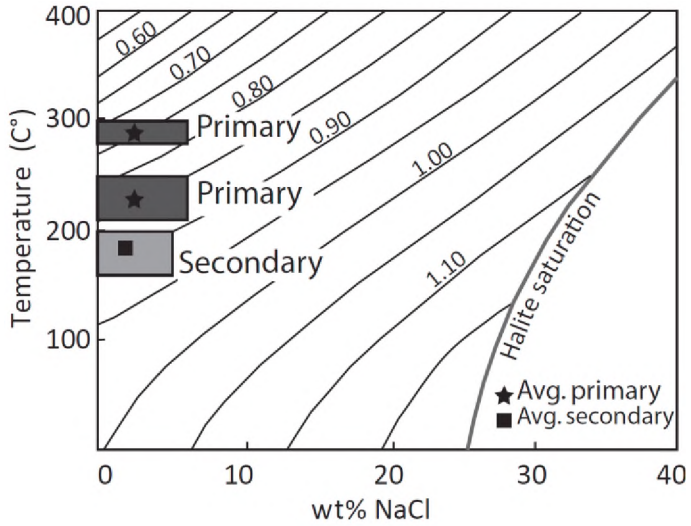

***Figure 6.9**: Density contours for a vapour-saturated saline fluid in the system H_2O-NaCl, depending on T_h and salinity (modified after Bodnar, 1983; Roedder, 1984) for normal fault samples. A salinity of ≤6 wt% NaCl equivalent and T_h ranges of 210-250 °C and 285-300 °C correspond to fluid density of 0.7-0.8 g/cm^3 and 0.78-0.9 g/cm^3 for primary fluids. A slightly lower salinity of ≤5 wt% NaCl equivalent, and a lower T_h range of 160-200 °C for secondary fluids shows a fluid density of 0.86-0.95 g/cm^3. The averages are ~0.75 and ~0.85 g/cm^3 for primary FIs and ~0.9 g/cm^3 for secondary FIs.*

The fluids are not completely NaCl-free, but fluid density has nevertheless been determined using pressure contours for the system CO_2 in the low temperature range. CO_2 vapour-liquid separations at 8.5-13 °C for primary inclusions and 7-12 °C for secondary inclusions (Table 5.3) correspond to density ranges of 0.82-0.85 g/cm^3 for the CO_2 component in primary fluids, and a slightly higher range of 0.83-0.87 g/cm^3 for secondary fluids (Figure 6.10).

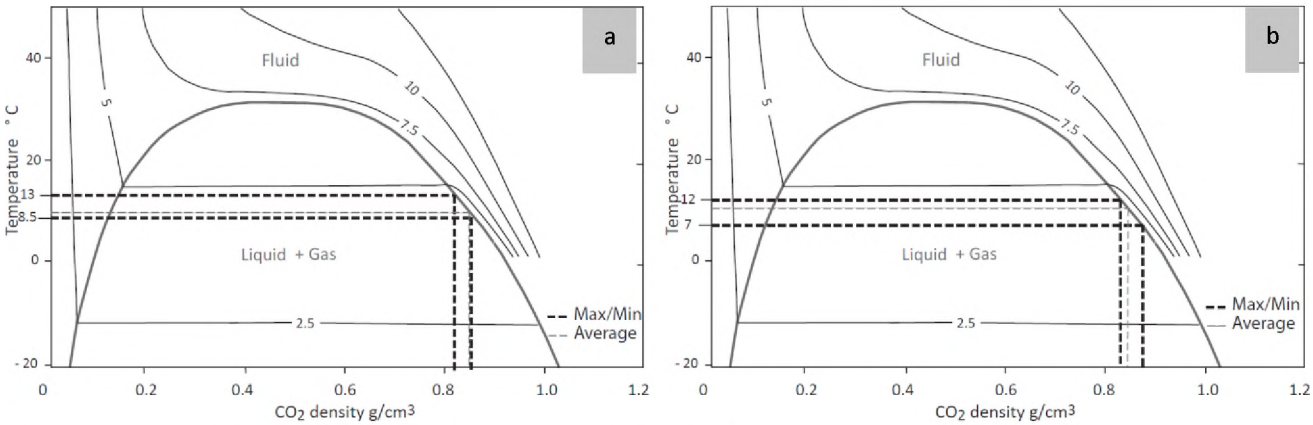

***Figure 6.10**: Temperature – Density plot for the system CO_2, showing pressure contours and phase boundaries (modified after Roedder, 1984). a) For primary fluids in normal fault samples, vapour-liquid separation between 8.5 and 13 °C suggests CO_2 density of 0.82-0.85 g/cm^3. b) For secondary fluids, vapour-liquid separation occurs between 7 and 12°C. This corresponds to a slightly higher CO_2 density range of 0.83-0.87 g/cm^3.*

For primary inclusions, the maximum T_h of 296 °C and CO_2 density of ~0.85 g/cm^3 corresponds to ~190 MPa. In secondary fluids, the maximum T_h of 198 °C and CO_2 density of ~0.85 g/cm^3 suggest a pressure of fluid capture of ~140 MPa (Figure 6.11). Hence the pressures determined with this method for normal faults are somewhat higher for primary and secondary fluids compared to those determined for thrust faults.

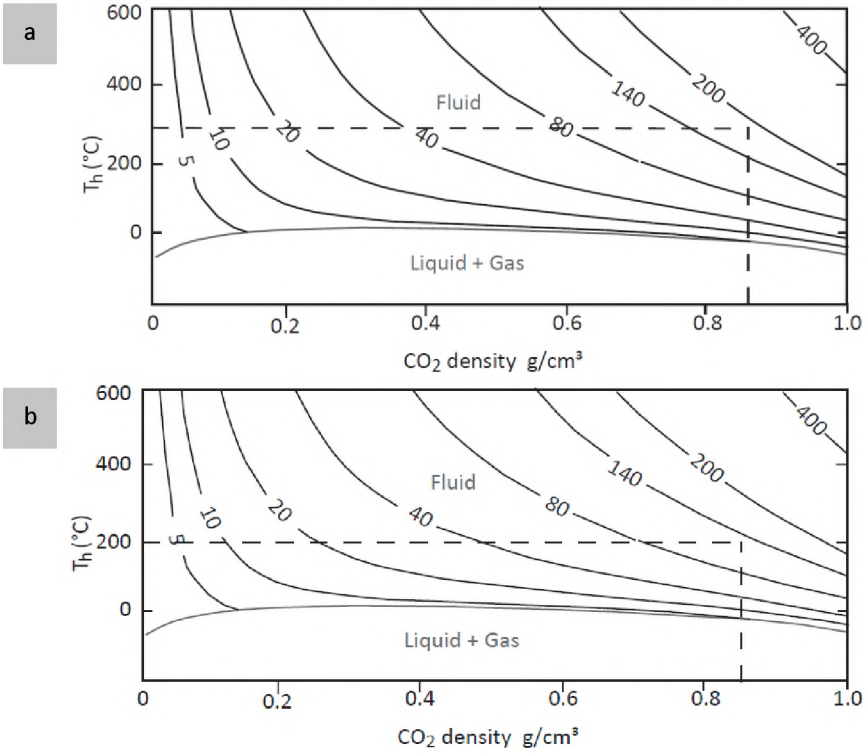

***Figure 6.11**: Pressure contours of CO_2 fluid, dependent on T_h and density (modified after Roedder, 1984). The maximum T_h and average density in normal faults corresponds to fluid pressures of a) ~170 MPa for primary inclusions in normal faults, and b) ~140 MPa for secondary inclusions.*

The lack of cogenetic CO_2-bearing and CO_2-free fluids in normal faults places limitations on the use of isochore intersections for determining P-T trapping conditions. Instead, trapping conditions can be estimated using the intersections of CO_2-bearing isochores with a geothermal gradient of 46 °C/km (Figure 6.12). The 46 °C gradient is the estimate from Büttner et al. (2016), and corresponds to the conditions worked out for cogenetic fluids in thrust faults. Two isochores can be produced for normal faults – one for the lower density fluids (0.75 g/cm^3), and one for the higher density fluids (0.85 g/cm^3). The intersections of these isochores yield a P-T estimate of ~150-190 MPa and ~260-340 °C for primary inclusions (Figure 6.12 a). For secondary inclusions, an isochore for the average density of all secondary fluids intersects the 46 °C/km gradient at ~100 MPa and ~180 °C (Figure 6.12 b).

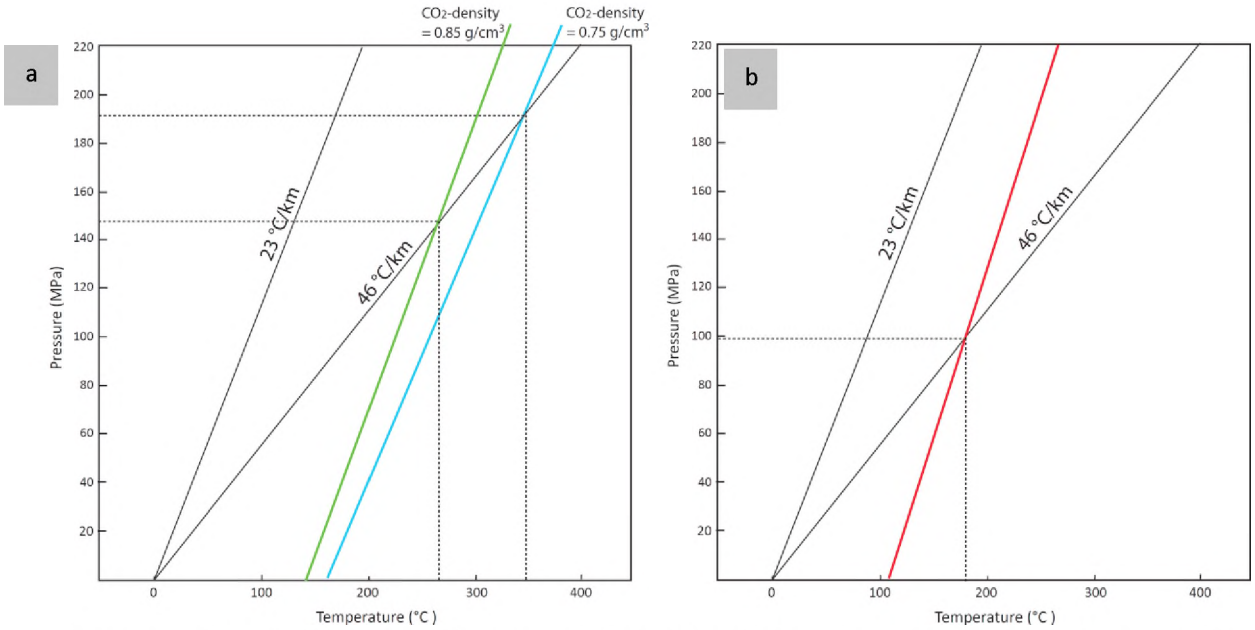

***Figure 6.12**: Iso-density (isochore) lines for H_2O-NaCl-CO_2-CH_4 inclusions in normal fault samples (modified after Kalyuzhnyi and Koltun, 1953; Roedder, 1984). Geothermal gradients of 23 °C/km (e.g. Allen and Allen, 1990) and 46 °C/km (Büttner, et al. 2016) have been added for comparison. a) High density (green) and low density (blue) isochores for primary inclusions yield P-T ranges of ~150-190 MPa and ~260-300 °C. b) The average density for secondary fluids produces an isochore (red) which intersects the 46 °C/km geothermal gradient at ~100 MPa and ~180 °C.*

Pressure of entrapment can also be inferred from the CH_4 Raman peak position for primary and secondary inclusion fluids. A peak position of 2915 cm^{-1} and 2913 cm^{-1} for primary and secondary fluids respectively correlates to 33 MPa for primary fluids and 66 MPa for secondary fluids (Figure 6.13, modified after Theiu et al., 2000). This pressure is significantly lower than the pressure obtained from the pressure contours for CO_2 fluid based on T_h and CO_2 density (190 MPa and 140 MPa for primary and secondary inclusions respectively; Figure 6.11). Given that the T_h-CO_2 density data set for normal faults is much larger than the Raman data set, and that the low pressures would imply an extremely high geothermal gradient (>80 °C/km at ~300 °C T_t), the CH_4 Raman peaks are not considered to reflect the true pressure of fluid capture. That the CO_2 fluid pressure contours (Figure 6.11) provide a more likely pressure estimate may also be supported by the results from thrust faults in the same region (Meiringspoort transect; Table 5.3). The approximate pressure for fluid capture in normal faults was most likely ~150-190 MPa for primary inclusions and ~100-140 MPa for secondary inclusions.

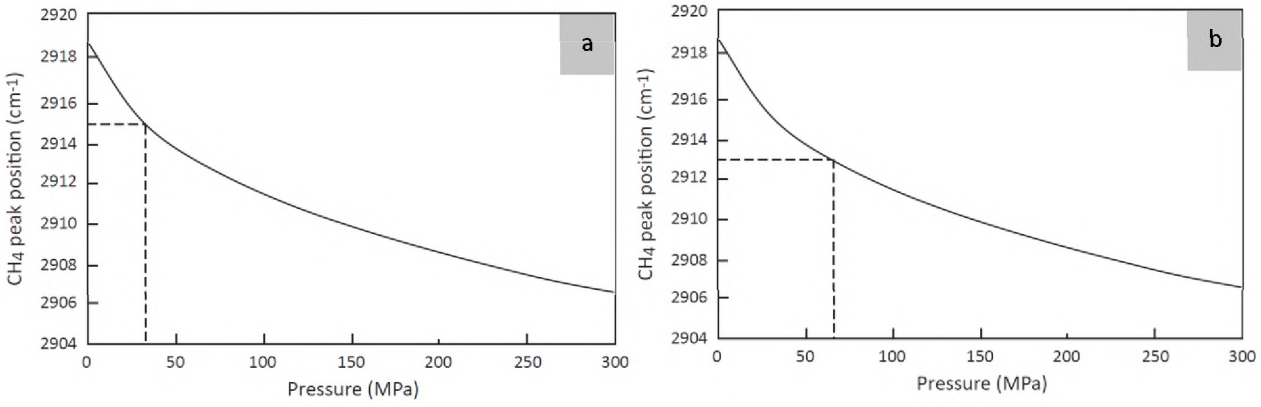

***Figure 6.13**: The Raman peak position plotted against pressure (modified after Seitz et al., 1993 and Theiu et al., 2000). The average peak positions in normal fault samples for a) primary and b) secondary inclusions show pressures of ~33 MPa and ~66 MPa respectively.*

6.4 Oblique- and strike-slip faults (H_2O-NaCl-CO_2)

Only primary inclusions, containing H_2O-NaCl-CO_2, were analysed in oblique- and strike-slip fault samples. Secondary inclusions are not large enough to be analysed thermometrically. The results and evaluations of microthermometric data for oblique- and strike-slip faults are summarised in Table 6.4.

Table 6.4: Summary of evaluation of microthermometric data for oblique- and strike-slip faults. These were determined with the FLUIDS software (Bakker, 2003).

		Primary FIs
Type		H_2O-NaCl-CO_2
Average Salinity (wt% NaCl equivalent)		3.3
Average bulk fluid composition	$X(H_2O)$	0.951498
	$X(Na^+/Cl^-)$	0.009885
	$X(CO_2)$	0.028733
Average fluid density (g/cm^3)		0.95

From the NaCl saturation diagram, the H_2O fluid density can be determined as 0.9-0.97 g/cm^3, with an average of 0.94 g/cm^3 (Figure 6.14). Density determined on FLUIDs software (Bakker, 2003) are in the same range, with an average of 0.95 g/cm^3 (Table 6.4). Phase separation of CO_2 ($T_h(CO_2)$) occurs between 8 and 14 °C, which corresponds to a CO_2 density of 0.82-0.86 g/cm^3 (Figure 6.15).

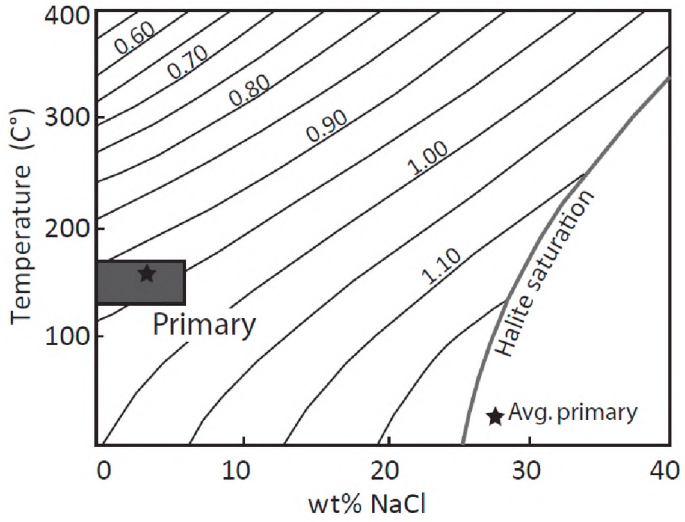

***Figure 6.14**: Density contours for a vapour-saturated saline fluid in the system H_2O-NaCl, depending on temperature of homogenisation and salinity (modified after Bodnar, 1983; Roedder, 1984), for strike-slip fault samples. A salinity of ≤6 wt% NaCl equivalent and a T_h range of 130-170 °C corresponds to fluid density of 0.90-0.97 g/cm^3 for primary fluids, with an average of 0.94 g/cm^3.*

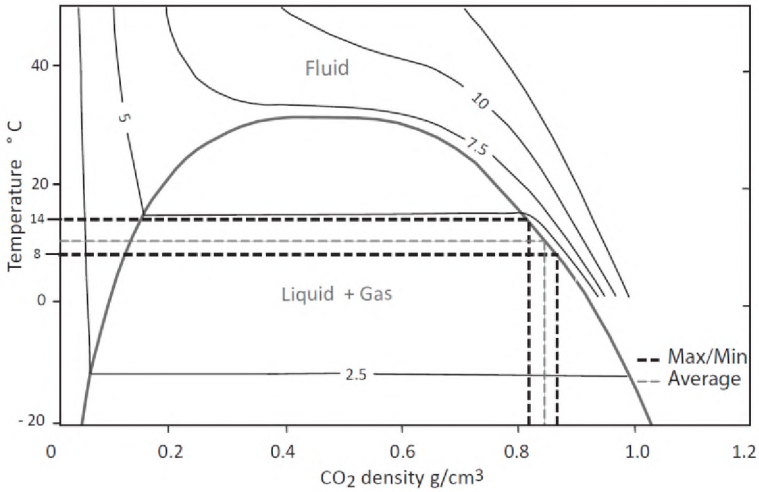

***Figure 6.15**: Temperature – Density plot for the system CO_2, showing pressure contours and phase boundaries (modified after Roedder, 1984). Although this system is intended for NaCl-free fluids, it has been applied here to NaCl-bearing CO_2 fluids. For primary fluids in strike-slip fault samples, vapour-liquid separation occurs between 8 and 14°C. This corresponds to a CO_2 density of 0.82-0.86 g/cm³.*

From the CO_2 density, and the maximum T_h of 170 °C (Table 5.4), the pressure of fluid capture determined from CO_2 pressure contours is about ~100 MPa for the formation of strike-slip faults (Figure 6.16).

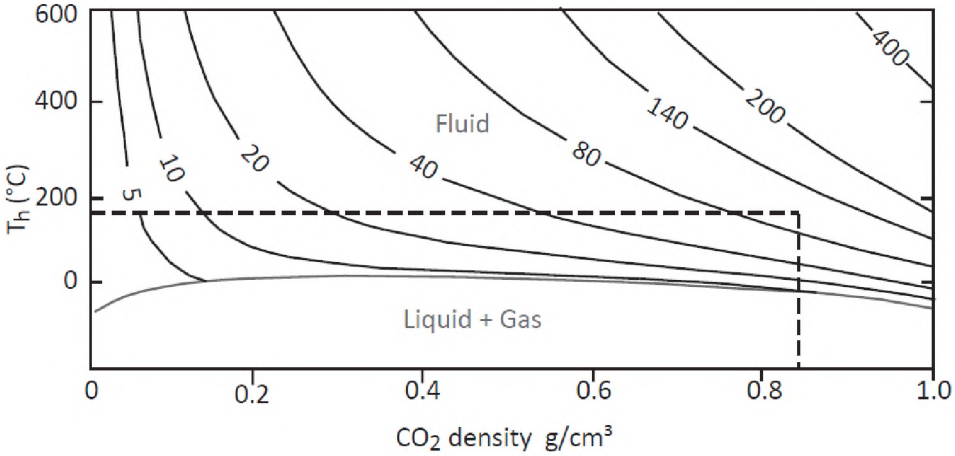

***Figure 6.16**: Pressure contours of CO_2 fluid, dependant on T_h and density (modified after Roedder, 1984). The maximum T_h and average density in normal faults corresponds to fluid pressures of ~100 MPa for primary inclusions in strike-slip faults.*

An isochore diagram can be plotted for primary fluids only. As with normal faults, the lack of cogenetic CO_2-bearing and CO_2-free fluids in strike-slip faults places a limitation on the use of isochores to determine trapping conditions. Instead, trapping conditions can be estimated using the intersections of CO_2-bearing isochores with a geothermal gradient of 46 °C/km (Figure 6.17), the geothermal estimate from Büttner et al. (2016) which corresponds to the conditions worked out for cogenetic fluids in thrust faults. The resulting field of P-T conditions of entrapment show a pressure range of ~135-142 MPa and a temperature interval of ~250-260 °C (Figure 6.17).

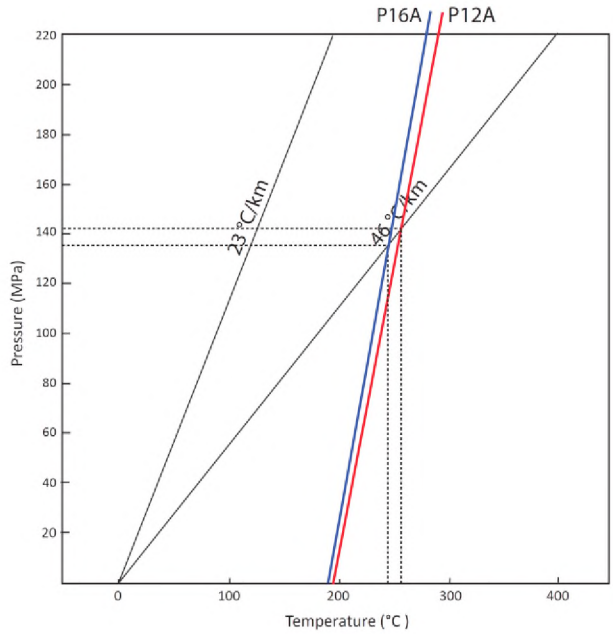

***Figure 6.17**: Iso-density (isochore) lines for H_2O-NaCl-CO_2 inclusions in strike-slip fault samples (modified after Kalyuzhnyi and Koltun, 1953; Roedder, 1984). Geothermal gradients of 23 °C/km (e.g. Allen and Allen, 1990) and 46 °C/km (Büttner, et al. 2016) have been added for comparison. Isochore for sample P12A (red) and sample P16A (blue) intersect the 46 °C/km geotherm at ~135-142 MPa and ~250-260 °C.*

6.5 Tension gash samples

There are two types of primary inclusions in tension gash samples (H_2O-NaCl and H_2O-NaCl-CO_2-CH_4) and two types of secondary inclusions (H_2O-NaCl and H_2O-NaCl-CO_2). The CO_2-CH_4-bearing primary inclusions and CO_2-bearing secondary inclusions are from only one sample, P5B, from the Outeniqua Pass. Table 6.5 summarises the results and evaluations of microthermometric data for tension gash samples (except for the average bulk fluid composition of CH_4-bearing fluids, which was not calculated).

Table 6.5: Summary of evaluation of microthermometric data for tension gashes. These have been determined graphically and using FLUIDS software (Bakker, 2003).

		Primary FIs		**Secondary FIs**	
Type		H_2O-NaCl	H_2O-NaCl-CO_2-CH_4	H_2O-NaCl	H_2O-NaCl-CO_2
Average salinity (wt% NaCl equivalent)		2.0	2.5	1.1	2.1
Average bulk fluid composition	X(H_2O)	0.987383		0.993309	0.957424
	X(Na^+/Cl^-)	0.006309		0.003346	0.006332
	X(CO_2)	NA		NA	0.029912
Average fluid density (g/cm^3)		0.82 & 0.90	0.83	0.92	0.94

6.5.1 H_2O-NaCl inclusions

From 49 readings in three tension gash samples, the salinity for primary H_2O-NaCl inclusions is in the range 0-4 wt% NaCl equivalent, with an average of 2.0 wt% (Table 6.5). Secondary inclusion salinity ranges from 0 to 2.5 wt% NaCl equivalent (calculated from 10 readings in one sample, with an average of 1.1 wt% NaCl equivalent).

From these salinities, and the T_h values for H_2O-NaCl inclusions in tension gashes, the fluid density can be determined as 0.75-0.85 g/cm^3 (de Vlugt; sample P16B; average: 0.82 g/cm^3) and 0.85-0.95 g/cm^3 (all other samples/areas; average: 0.9 g/cm^3) for primary inclusions, and 0.9-0.93 g/cm^3 for secondary inclusions (average = 0.92 g/cm^3; Figure 6.16). These figures are similar to those calculated with the FLUIDS software (Bakker, 2003). The salinity in the de Vlugt sample is in the same range as seen in other tension gashes; the lower density is determined because of the higher T_h readings in this sample P16B (Figure 6.18 and Table 5.5).

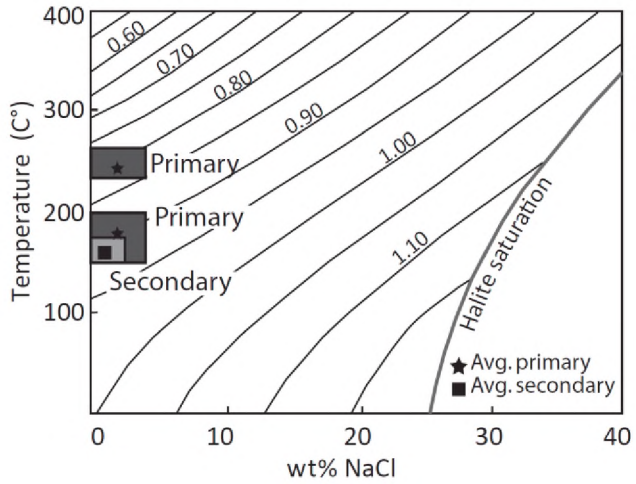

***Figure 6.18**: Density contours for a vapour-saturated saline fluid in the system H_2O-NaCl in tension gashes, depending on temperature of homogenisation and salinity (modified after Bodnar, 1983; Roedder, 1984). A salinity of ≤4wt% NaCl equivalent and a T_h ranges of 155-190 °C and 235-265 °C (sample P16B; de Vlugt section) correspond to fluid density of 0.75-0.85 g/cm^3 and 0.85-0.95g/cm^3 for primary fluids. A lower salinity of ≤2.5 wt% NaCl eq., and a narrower T_h range of 150-175 °C for secondary fluids shows a fluid density of 0.9-0.93 g/cm^3 (all other tension gashes except sample P16B). The averages are ~0.82 and ~0.9 g/cm^3 for primary FIs, and ~ 0.92 g/cm^3 for secondary FIs.*

6.5.2 H_2O-NaCl-CO_2 and H_2O-NaCl-CO_2-CH_4 inclusions

These types of inclusions come from one sample (P5B) in the Outeniqua Range. There are 35 readings for primary inclusions and five readings for the less abundant secondary inclusions. Phase separation ($T_h(CO_2)$) of CO_2 vapour and liquid occurs between 9-14 °C for primary FIs and between 10-12 °C for secondary FIs. From pressure contours for the low-temperature CO_2 system, a fluid density of 0.82-0.86 g/cm^3 (average = 0.83 g/cm^3) for primary fluids, and 0.83-0.85 g/cm^3 (average = 0.84 g/cm^3) for secondary fluids can be determined (Figure 6.19). FLUIDS software (Bakker, 2003) yielded a higher average density (0.94 g/cm^3) for the secondary CO_2-bearing fluids. For the purposes of further calculations, the FLUIDS results are used (Table 6.5).

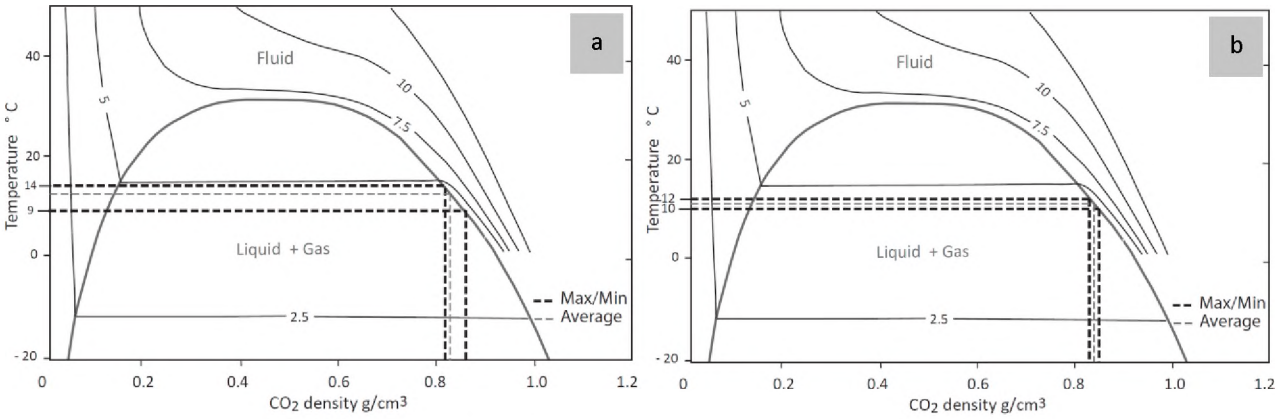

***Figure 6.19**: Temperature – Density plot for the system CO_2, showing pressure contours and phase boundaries (modified after Roedder, 1984). Although this system is intended for NaCl-free fluids, it has been applied here to NaCl-bearing CO_2 fluids. a) For primary fluids in tension gash samples, vapour-liquid separation between 9 and 14 °C suggests CO_2 density of 0.82-0.86 g/cm³. b) For secondary fluids, vapour-liquid separation occurs between 10 and 12°C. This corresponds to a narrower range of 0.83-0.85 g/cm³ for CO_2 density. The averages are 0.82 and 0.84 g/cm³ for primary and secondary inclusions respectively.*

The lack of cogenetic CO_2-bearing and CO_2-free fluids in tension gashes places a limitation on the use of isochores to determine trapping conditions. Instead, possible conditions have been worked out using intersections of non-cogenetic fluid isochores (Figure 6.20). The primary fluid isochores intersect at ~170 MPa and ~270 °C. The secondary fluid isochores intersect at ~160 MPa and ~280 °C, although it must be noted that the isochore intersect at a high angle, and there is therefore a high margin of error. As with thrust faults, these possible trapping conditions fall very close to the maximum geothermal gradient of 46 °C/km.

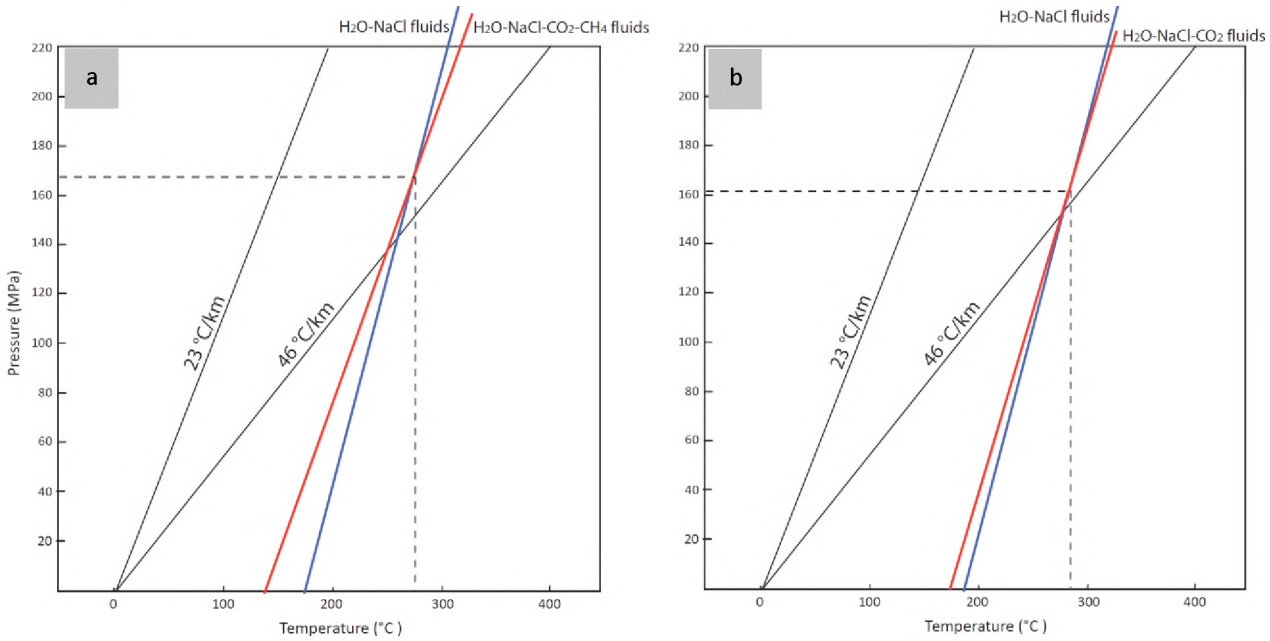

***Figure 6.20**: Iso-density (isochore) lines for H_2O-NaCl (blue) and H_2O-NaCl-CO_2(-CH_4) (red) inclusions in tension gash samples (modified after Kalyuzhnyi and Koltun, 1953; Roedder, 1984). Geothermal gradients of 23 °C/km (e.g. Allen and Allen, 1990) and 46 °C/km (Büttner, et al. 2016) have been added for comparison. a) The isochores for primary fluids intersect at ~170 MPa and ~270 °C. b) The isochores for secondary fluids intersect at ~160 MPa and ~280 °C.*

CO_2 density, together with the maximum observed T_h (290 °C for H_2O-NaCl-CO_2-CH_4 primary inclusions and 215 °C for H_2O-NaCl-CO_2 secondary inclusions) yields fluid pressures of ~160 MPa for primary fluids and ~130 MPa for secondary fluids as maximum P_t (Figure 6.21).

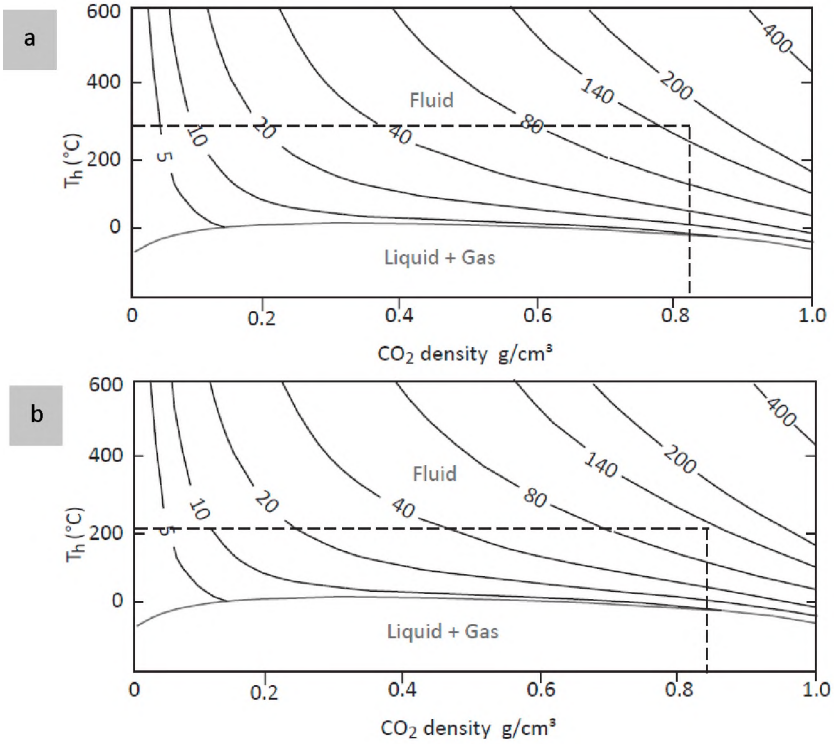

***Figure 6.21**: Pressure contours of CO_2 fluid, dependent on T_h and density (modified after Roedder, 1984). The maximum T_h and average CO_2 density in tension gashes corresponds to fluid pressures of a) ~160 MPa for primary inclusions in tension gashes, and b) ~130 MPa for secondary inclusions in sample P5B (Outeniqua Range).*

Pressure of entrapment can also be inferred from the CH_4 Raman peak position for primary inclusion fluids. An average peak position of 2914 cm^{-1} correlates to 47 MPa for primary fluids (Figure 6.22). As was the case for normal fault samples, this pressure is significantly lower than the pressure obtained from the pressure contours for CO_2 fluid based on T_h and CO_2 density (~160 MPa; Figure 6.21). Given that the T_h-CO_2 density data set for tension gash samples provides more realistic results and is much larger than that of the CH_4 Raman data, it is unlikely that the pressure results from the CH_4 Raman peak position are reliable.

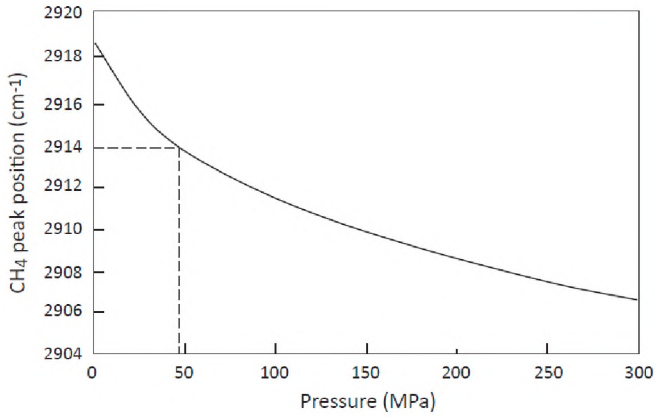

***Figure 6.22**: The Raman peak position plotted against pressure for tension gash sample P5B (modified after Seitz et al., 1993 and Theiu et al., 2000). The average peak positions in the tension gash sample P5B is 2914 cm^{-1}, which correlates to 47 MPa for the pressure of entrapment.*

6.6 Folded veins (H_2O-NaCl)

Only primary inclusions containing H_2O-NaCl were analysed in folded vein samples. Table 6.6 summarises the results and evaluations of microthermometric data from Chapter 5.

Table 6.6: Summary of evaluation of microthermometric data for fold samples, calculated with FLUIDS software (Bakker, 2003).

		Primary FIs
Type		H_2O-NaCl
Average Salinity (wt% NaCl equivalent)		3.4
Average bulk fluid composition	$X(H_2O)$	0.978839
	$X(Na^+/Cl^-)$	0.010581
Average fluid density (g/cm^3)		0.94

The salinity is ≤5 wt% NaCl equivalent (equation 1), with an average of 3.4 wt%. (n=22; sample P18A; Table 6.6). Based on this salinity range, the fluid density can be determined as 0.88-0.96 g/cm^3, with an average of ~0.94 g/cm^3 (Figure 6.23). These values are consistent with those found with FLUIDS software (Bakker, 2003). T_h ranges from 150 to 180 °C (Table 5.6). A temperature correction for low-saline fluids (Roedder, 1984 Figure 6.24) suggests a temperature correction of ~140 °C, which suggests a trapping temperature of 290-320 °C.

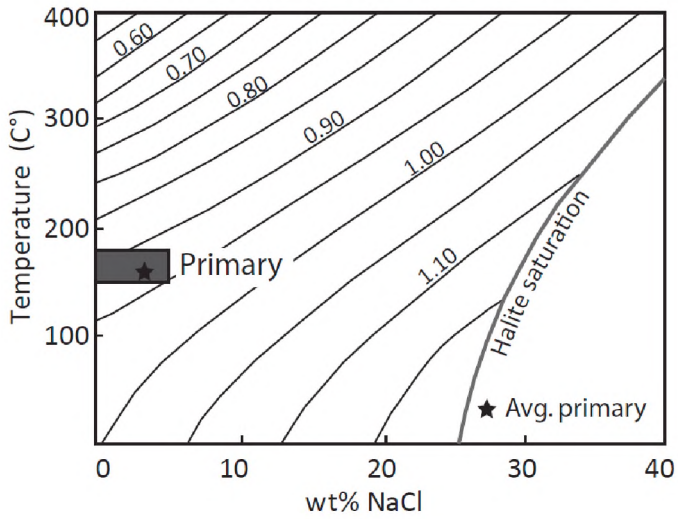

***Figure 6.23**: Density contours for a vapour-saturated saline fluid in the system H_2O-NaCl, depending on temperature of homogenisation and salinity (modified after Bodnar, 1983; Roedder, 1984), for the folded vein sample. A salinity of ≤5wt% NaCl equivalent and a T_h range of 150-180 °C corresponds to a fluid density of 0.87-0.95 g/cm^3 for primary fluids. The average density is ~0.94 g/cm^3.*

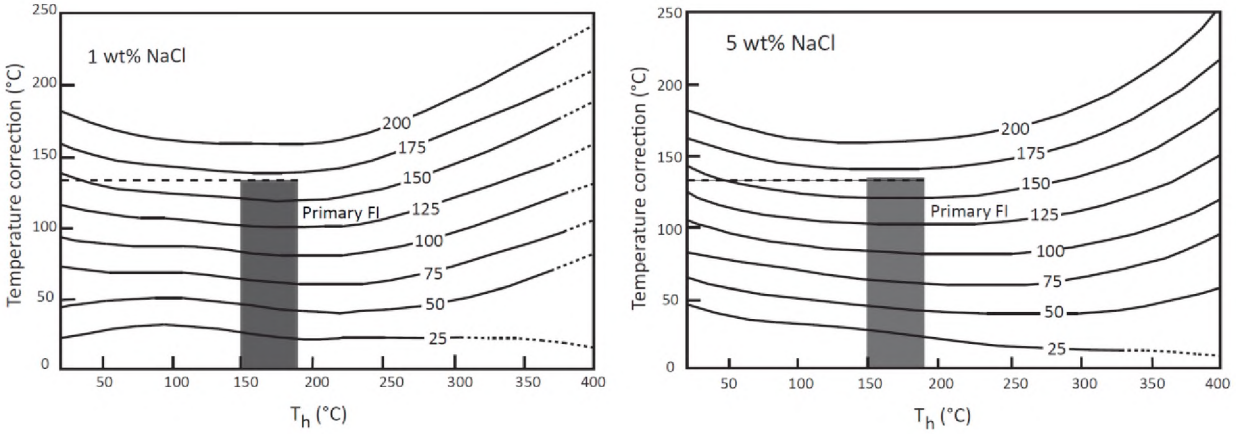

***Figure 6.24**: T_h temperature correction for saline hydrous fluids in fold sample P18A. Pressure contours are given in MPa (modified after Roedder, 1984). The temperature correction is ~140 °C for primary fluids, for both 1 wt% and 5 wt% NaCl equivalent.*

In absence of CO_2 in the fluids, the pressure of trapping can only be inferred from the H_2O-NaCl isochore. Due to its steep slope and its position, the 0.93 g/cm^3 isochore reaches temperatures exceeding 300 °C only at pressures above ~220 MPa (Figure 6.25). About 290-300 °C are the minimum of effective quartz plasticity and recrystallization (Voll, 1976), which allows folding of quartz-rich rocks, such as the folded hydrothermal veins. It appears therefore possible that fluid capturing, and hence vein formation in sample P18A, might have taken place at conditions that also would have allowed subsequent folding of the veins. The folding of the veins is the deformation event that marks the maximum temperature seen in the material sampled for this study.

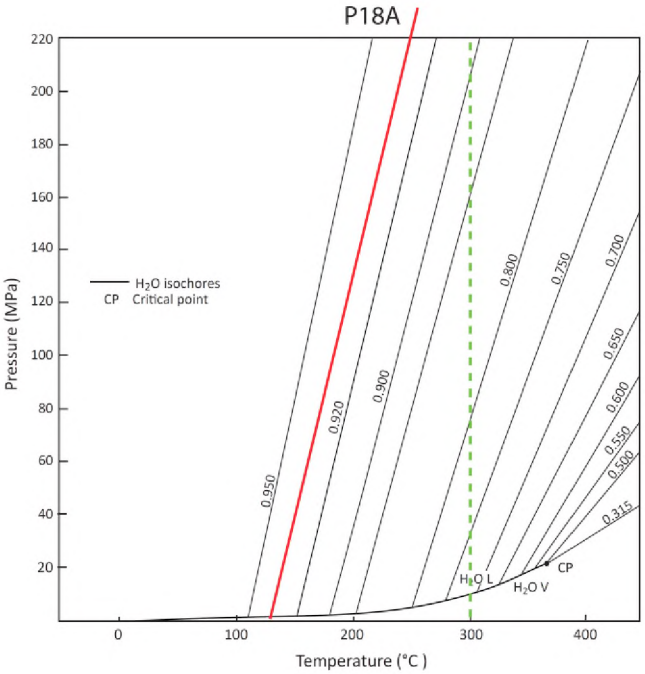

***Figure 6.25**: H_2O iso-density (isochore) lines for H_2O-NaCl inclusions in tension gash samples (modified after Kalyuzhnyi and Koltun, 1953; Roedder, 1984). The 0.93 g/cm^3 isochore for fold sample P18A (red) reaches temperatures exceeding 300 °C at pressures exceeding 220 MPa.*

6.7 Summary

The salinity for primary and secondary fluids in all structures is effectively constant, with all fluids having a maximum salinity between 2.5 and 6 wt% NaCl equivalent. Fluid density is also roughly constant across all structures. Primary H_2O-NaCl inclusions have a (very) slightly lower fluid density (0.85-0.95 g/cm^3) than secondary H_2O-NaCl inclusions (0.90-0.95 g/cm^3). Similarly, CO_2 fluid density is fairly constant in primary and secondary inclusions across all structures (0.81-0.87 g/cm^3).

Pressure and temperature of trapping for primary fluids in thrust and reverse faults are 170 – 175 MPa and 240 – 300 °C. Strike-slip faults have lower P-T conditions of ~135-140 MPa and ~250 °C. Tension gashes (~170 MPa; ~270 °C) have similar trapping P-T conditions to thrust and reverse faults, while normal fault trapping conditions (~190 MPa; ~300 °C) are somewhat higher than thrust and reverse faults.

7. DISCUSSION

The Cape Supergroup (CSG; Figure 7.1) represents approximately 8-10 km of stratigraphy, and consists of clastic sedimentary rocks of the Table Mountain Group (~4500 m), the Bokkeveld Group (~3000 m) and the Witteberg Group (~1700 m; Thamm & Johnson, 2006). The lowermost Table Mountain Group was deposited from Early Ordovician to Early Devonian periods, between ~480-390 Ma (Thamm & Johnson, 2006). The Devonian Bokkeveld Group was deposited between ~390-350 Ma, and deposition of the uppermost Witteberg Group took place from the Late Devonian to Early Carboniferous Periods, between ~350-335 Ma (Thamm & Johnson, 2006). The Karoo Supergroup unconformably overlies the CSG and was deposited between ~325-180 Ma (Johnson et al., 2006).

From the recrystallization of hydraulic quartz (Voll, 1976), as well as the presence of phyllite in the study areas, we know that the maximum temperatures reached during the Cape Orogeny in the currently exposed levels of the crust must have exceeded 300 °C, as also suggested by Frimmel et al., (2001). Hansma et al., (2016) used white mica for age dating in places, but such metamorphic white mica is rare in the Cape Fold Belt. Temperatures are therefore unlikely to have significantly exceeded ~440 °C, which would have led to more abundant white mica growth in pelitic rocks (Simpson et al., 2000).

The samples which were used for P-T estimations in this study come predominantly from the Table Mountain Group (Figure 7.1). The exceptions are P17 (not used for microthermometry), P18 (fold sample used for microthermometry), and P19 (one thrust sample and one tension gash sample used for microthermometry).

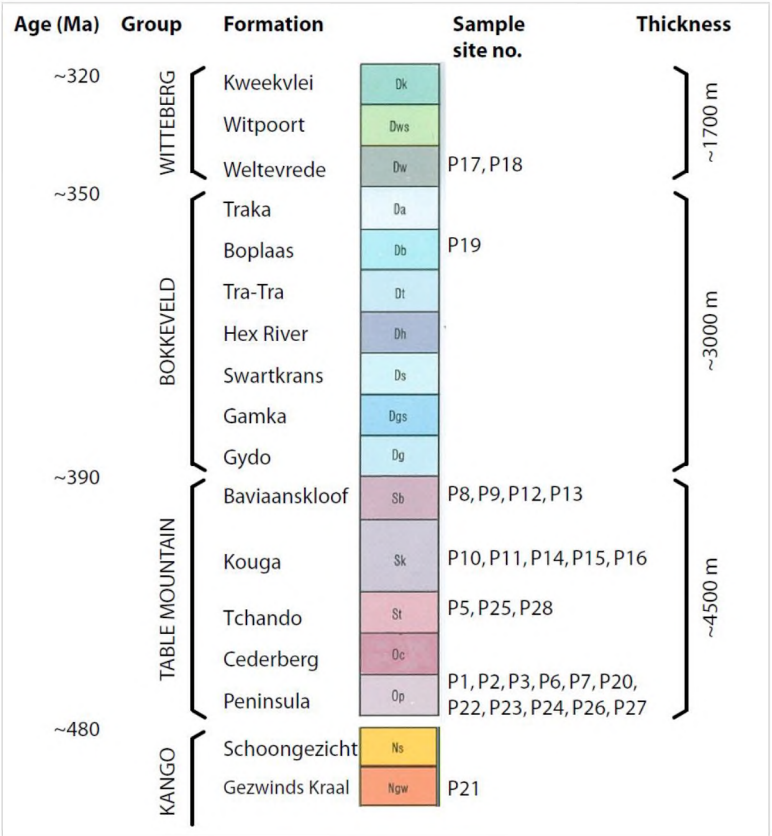

Figure 7.1: *Stratigraphic profile of the formations within the Cape Supergroup and the uppermost formations of the Kango Inlier, showing the deposition age and thickness of each group, and sample sites from each formation (modified after Council for Geoscience, 1979).*

Primary fluids from thrust and reverse fault samples from the Table Mountain Group show trapping conditions of ~170-175 MPa and ~240-300 °C. Strike-slip faults show slightly lower trapping P-T ranges (250-260 °C; ~140 MPa). Normal fault samples, also taken from the Table Mountain Group, show P-T conditions of ~190 MPa and ~300 °C (slightly higher than thrust and reverse faults). The thrust sample from the Boplaas Formation (P19A, Bokkeveld Group) shows minimum trapping pressure and temperature of ~200 MPa and ~≥300 °C, while the fold sample (P18A) from the Weltevrede Formation in the Witteberg Group shows trapping conditions of ~160 MPa and ~300 °C. These results indicate that initial quartz precipitation took place under sub- to lower greenschist facies conditions.

Plastic deformation, including recrystallization and the formation of foam textures in vein quartz of thrusts (section 4.1, Figure 4.1 a), reverse faults (section 4.2, Figure 4.4), oblique-slip faults (section 4.4, Figure 4.8 a & b), tension gashes (section 4.5, Figure 4.10), and folds (section 4.6, Figure 4.12) indicate that after the precipitation of vein quartz, and hence after the formation of the faults, temperatures must have been well into the greenschist facies for enough time to facilitate static recrystallization (Voll, 1976).

This overprint of veins at temperatures higher than their sub-greenschist facies formation conditions indicates that temperatures increased subsequent to hydraulic fracturing and thrust slip. The kinematics might still have been contractional (i.e. thrusting), but there is no evidence of further fluid influx, dilation and precipitation of new vein quartz during or after recrystallization. Increasing temperatures suggest that thrust slip in the lower CFB (e.g. Peninsula Formation) took place, or at least started, on the prograde P-T path.

Strike-slip faulting occurred at the lowest P-T conditions. Recrystallisation of vein quartz along strike-slip faults rules out the possibility that they could have occurred late on the retrograde path. Instead, strike-slip faulting probably occurred early on along the prograde path as a result of crustal shortening, before thrusting occurred.

Normal faults formed at slightly higher P-T conditions to those of thrust and reverse faults, and therefore must have formed close to peak conditions, or at the beginning of the retrograde path. It is generally agreed that normal faults in the CFB are associated with the break-up of Gondwana in the late Jurassic and Cretaceous (Watkeys, 2006), ~100 million years after the contractional deformation of the CFB (Hansma et al., 2016). However, the relationship of the normal faults analysed in this study with the break-up of Gondwana would only be possible if the greenschist facies temperatures indicated by FIs and by ductile overprint textures in vein quartz had persisted well into the Mesozoic, which is not particularly likely. A more likely scenario is that these normal faults are related to late-orogenic extension and formed at or shortly after the thermal peak, after contractional faulting and folding had thickened the crust in the CFB.

Timing of deformation events

Fluid inclusions from contractional structures at the base of the Table Mountain Group in the lower CFB record P-T conditions in sub- to lower greenschist facies (~170-175 MPa; ~240-300 °C), implying a depth of formation of ~6800 m depth (assuming an average density of ~2600 kg/m^3 for the overlying rock column).

The proposed thickness of the CSG of ~9200 m (Figure 7.1; Thamm & Johnson, 2006) would have been sufficient to exert the required pressure (~170 MPa) of the analysed faults that were located at the bottom of the CSG. However, the sampling sites in the upper Table Mountain Group were overlain by approximately only 4700-5000 m thick CSG rocks (Thamm & Johnson, 2006), which requires a further ~1800-2100 m of overburden (corresponding to ~40 MPa) in order to reach the calculated pressure conditions.

This missing load could be explained in three ways. (i) Assuming faulting at ~170 MPa in more or less horizontally oriented and undeformed crust, an additional 1800-2100 m of CSG sedimentary rocks would be required on top of the unconformity along the CSG/Karoo Supergroup boundary. These rocks would have to be deposited after ~335 Ma, the age of the uppermost preserved CSG rocks (Tankard et al., 2009), but eroded again *after faulting* but *before* the deposition of Karoo Supergroup sediments (~302-288 Ma, Bangert et al., 1999). (ii) A second possibility would be that faulting occurred at a time when ~1600 m of Karoo Supergroup rocks would have provided additional 40 MPa pressure on the faulting site. This would approximately correspond to the thickness of the Dwyka Group, Ripon and some Fort Brown Formation sediments in the adjacent part of the Karoo Basin (profile C of Johnson et al., 2006). This would somewhat predate the growth of white mica at ~276-261 Ma (Hansma et al., 2016; Tankard et al., 2009). (iii) Possibly, at the time of hydraulic faulting, the CGS was already was tectonically thickened, accounting for the 40 MPa gap between the estimated pressure during faulting and the pressure exerted by the known overlying CSG. On the basis of the current data all three scenarios appear to be possible. Problematic, however, is that there are no precise data for the timing of deposition of the CSG and the Karoo SG, and the precise thicknesses of their various formations.

Hansma et al. (2016) proposed ~276-261 Ma as the age for deformation in the CFB. Since this age is based on growth of muscovite, the highest grade metamorphic phase in the CFB, it would also be the age of the thermal peak in the CFB. A younger age at ~254.6-248 Ma may either be cooling or a second deformation age (section 1.2.3, pg. 5). By 276 Ma, ~4000 m of the overlying Karoo Supergroup had already been deposited on top of the CSG. Together with the overlying ~5000 m of the Bokkeveld and Witteberg Groups, the uppermost Table Mountain Group would have been exposed to minimum pressures of ~240 MPa. Hence, prograde faults formed at ~170 MPa must be considerably older. The depth of ~6800 m required to yield the calculated P-T conditions of 170-175 MPa (in thrust faults in the Table Mountain Group) was reached at approximately 335 Ma (Tankard et al., 2009). At this time, deposition of the Witteberg Group was coming to an end, and still further deposits would have to be accumulated to reach ~6800 m thickness overlying the Table Mountain Group. The time to deposit these sediments, or, alternatively the time required for crustal thickening to reach 170 MPa at the faulting level, would have to be subtracted from 335 Ma.

This time of 335 Ma predates mica growth at the proposed thermal peak (~276-261 Ma, Hansma et al., 2016) by about 60 million years. Since the vein quartz in all fault structures formed on the prograde P-T path, and is overprinted later at higher greenschist facies (regional peak) temperatures, the onset of deformation forming hydraulic thrust faults in the lower parts of the CSG may be bracketed by 335 Ma and the thermal peak at ~276-261 Ma. In order to allow for additional deposition or thickening to increase the pressure at fault sites by ~40 MPa, the estimate of 335 Ma is likely to be too high. A younger age, but older than

the CSG-Karoo Supergroup unconformity (302-288 Ma; Bangert et al., 1999), might be more realistic.

The fold sample (P18A) from the Witteberg Group records greenschist facies conditions of fluid influx, precipitation of vein quartz, and subsequent deformation during folding. This is in agreement with formation and deformation close to the thermal peak, postdating the formation of syntectonic veins along the thrusts in the Peninsula Formation. Formation and deformation of sample P18A may correlate in time with deformation at the thermal peak (~276-261 Ma, according to Hansma et al., 2016). This vein formation, subsequent folding and recrystallization might be coeval with the ductile overprint in prograde thrust-bound veins that led to the recrystallization of vein quartz.

The P-T conditions recorded for sample P19A from a flat-ramp structure in the Boplaas Formation (Figure 7.1) are problematic. The homogenisation temperature for FIs in this sample is similar to those seen in other thrusts, but P_t and T_t are slightly higher (~200 MPa and ~≥300 °C). However, the stratigraphic position of P19A high up in the Bokkeveld Group should have caused a lower pressure of vein formation, if that vein was a prograde structure. The intense recrystallization of this vein is in agreement with the significant displacement at greenschist facies temperatures along this structure (Figure 3.14 & Figure 4.2 c). It is possible that more CSG rocks existed above the Witteberg Group that were eroded before the deposition of the Karoo Supergroup sediments began. It may also be that thrusting had already increased the pressure on Bokkeveld Group rocks at locality P19, and that the age of this thrust is younger and displacement is not prograde but closer to the thermal peak. At this time, several thousand meters of Karoo deposits would have provided higher pressure.

The high P-T values for fluid precipitation along the normal faults (P23A and 24A, from the Meiringspoort section; Figure 3.11) are not in agreement with their generation during the breakup of Gondwana, at a time postdating the thermal peak by >100 million years. A relationship between normal faults in the CFB and Gondwana breakup has been repeatedly proposed in the literature (e.g. Watkeys, 2006; Tankard et al., 2009). At this time, the crust should have cooled down and the Swartberg Range should have been exhumed to shallow crustal levels. Instead, the pressure and temperature obtained from FI microthermometry (~190 MPa, ~300 °C) suggest a formation at about 7700 m depth at a high geothermal gradient of ~38 °C/km. This high geothermal gradient is in broad agreement with that determined for other faults, and also with the geothermal gradient determined for hydraulic faults in the Grahamstown area at the eastern end of the CFB (Büttner et al., 2016). It is therefore plausible that the normal faults formed in a context of the Cape Orogeny, and are not related to the context of late-Mesozoic Gondwana breakup. Fluid temperatures and subsequent recrystallization suggest that extensional kinematics occurred close to or at the thermal peak, at the end of crustal contraction and at a time before the crust cooled down to sub-greenschist facies temperatures.

In a similar study based on fluid inclusions in hydraulic quartz veins from the Witteberg Group in the eastern CFB (~400 km east of the structures examined in the current study), Büttner et al. (2016) argue that deformation in the upper Witteberg Group at the eastern end of the CFB could not have occurred in the Middle Permian (276-261 Ma; Hansma et al., 2016), because overburden at that time would not have been thick enough for the P-T conditions calculated for faulting in upper Witteberg Group rocks. The hydraulic structures

near Grahamstown formed in the latest stages of, or postdate, the large-scale regional folding of the CSG. Large parts of the Karoo Supergroup must have been deposited at the time of displacement. The faults examined by Büttner et al. (2016) developed in the upper Witteberg Group, significantly higher in the CSG stratigraphy than the structures examined here. This suggests that there are not only stratigraphic variations in the timing of hydraulic faulting within the Cape Supergroup, but also variations along strike of the orogen. In addition, and considering the fault in the Boplaas Formation from the Meiringspoort section (sample 19A), there might also be variations in the sequence and absolute timing of deformation processes between the Swartberg Range and the regions further south in the CFB.

The geothermal gradients seen in practically all samples in the range of 38-46 °C/km are significantly higher than expected for a fold-and-thrust belt (~23 °C/km; Allen & Allen, 1990). The proposed geothermal gradients are based on the assumption that the fluids captured in fluid inclusions were at ambient temperature. If these fluids were sourced at deeper levels of the crust and transported very quickly to shallower levels, they might have been hotter than the host rock. For instance, a geothermal gradient of 23 °C/km at 5500 m depth (~145 MPa), would produce host rock temperatures of about 125 °C, which is about 100 °C colder than the observed fluid temperature. At a gradient of ~23 °C/km, the temperature of the fluids would require a depth of >10 000 m. Such a vertical distance between fluid source and host rock appears too large to allow fluid transport without cooling. The crust of the CFB also did not contain large heat sources (such as magma chambers) that could have provided hot fluids at shallow crustal level. It is therefore likely that the high regional geothermal gradients in the range of 38-46 °C/km are realistic. Of the numerous tectonic models that have been suggested for the formation of the CFB, a transpression model or an Andean-type subduction and foreland basin model account best for the overall characteristics of the CFB (Booth, 2011). If the CFB formed in a tectonic setting of a transpression or foreland system, some additional process must have increased the geothermal gradient during deformation to reach the high geothermal gradients deduced in the current study.

8. CONCLUSION

One of the biggest obstacles in reconstructing the tectonic history of the Cape Fold Belt (CFB) has been the uncertainty of the true age of the Cape Orogeny. Results from the current study have helped to limit the time window for hydraulic fracturing in at least the lower, southern part of the CFB. Microthermobarometric evidence suggests that the hydraulic deformation events that led to the formation of the CFB faults probably started in the Late Carboniferous, before the erosion of the CSG to the level of the unconformity below the Karoo sediments. Deformation continued towards the thermal peak in the Late Permian (276-261 Ma), and towards the retrograde evolution. At the time of the peak much of the Karoo Supergroup had been deposited and the folding and faulting of the lower Karoo Supergroup attests to the ongoing tectonics of the Cape event.

The onset of prograde hydraulic faulting may predate the thermal peak by several tens of million years. The regional folding, evidently in the plastic field of quartzite, may correlate in time and temperature with the recrystallization of vein quartz that is observed in most samples. Foam textures indicate that the temperature increased to conditions well in the greenschist facies. The retrograde P-T evolution is not well constrained in the hydraulic faults. The capture of secondary fluids at 200-230 °C and 105-120 MPa is not bound to the formation of macro-structures and may be related to only minor deformation in the presence of retrograde fluids. The abundant brittle faults in the CFB that do not show vein quartz may be the main retrograde tectonic record of the Cape Orogeny.

The relative age of hydraulic faults is not entirely clear. Strike-slip faults show the lowest P-T conditions of primary fluid capture (~250 °C, ~140 MPa) but the recrystallization of vein quartz indicates faulting prior to the thermal peak. Hence strike-slip faults may have been the first faults to form. Thrust faults are also prograde, but somewhat higher in pressure and temperature. The normal faults show the highest fluid pressures and temperatures and may have formed close to the thermal peak in the lower greenschist facies, perhaps at temperatures of >300 °C and ~200 MPa (Figure 6.12). The recrystallization of vein quartz may have happened at similar P-T conditions at the beginning of the retrograde P-T path in the Cape Orogen. Hansma et al.'s (2016) muscovite ages date this stage.

Büttner el al. (2016) argued that hydraulic faulting in the upper Witteberg Group in the eastern CFB could not have occurred before the thermal peak suggested by Hansma et al. (2016), but rather formed on a retrograde path near the end of, or postdating, the large-scale regional folding of the CSG. There must, therefore, be variations in hydraulic fracturing not only stratigraphically, but also along strike of the orogen between the central part of the CFB and its eastern wing.

The geothermal gradients from fluid inclusion samples, in the range of ~44 °C/km, are significantly higher than expected for a foreland system. There must, therefore, have been some additional process which increased the geothermal gradient during deformation, but the nature of this process is unclear.

References

Allen, P.A. & Allen, J.R., 1990. Basin Analysis – principles and applications. Blackwell Scientific Publications, London, UK, 450pp.

Bakker R.J., 2003. Package FLUIDS 1. Computer programs for analysis of fluid inclusion data and for modelling bulk fluid properties. Chemical Geology, 194, 3-23.

Bangert, B., Stollhofen, H., Lorenz, V. & Armstrong, R., 1999. The geochronology and significance of ash-fall tuffs in the glaciogenic Carboniferous-Permian Dwyka Group of Namibia and South Africa. Journal of African Earth Sciences, 29(1), 33-49.

Bodnar, R.J., 1993. Revised equation and table for determining the freezing point depression of H_2O-NaCl solutions. Geochimica et Cosmochimica Acta , 57, 683-684.

Bodnar, R.J., 2003. Reequilibration of Fluid Inclusions. In Sampson, I., Anderson, A. & Marshall, D. (eds.), Fluid Inclusions: Analysis and Interpretation. Vancouver: Mineralogical Association Canada, 213-230.

Booth, P.W.K., 1996. The relationship between folding and thrusting in the Floriskraal Formation (upper Witteberg Group), Steytlerville, Eastern Cape. South African Journal of Geology, 99, 235–243.

Booth, P.W.K., 2011. Stratigraphic, structural and tectonic enigmas associated with the Cape Fold Belt: Challenges for future research. South African Journal of Geology, 114, 235-248.

Booth, P.W.K. & Shone, R.W., 1992. Structure of the Table Mountain Group in the Port Elizabeth area. South African Journal of Geology, 95, 29–33.

Booth, P.W.K. & Shone, R.W., 2002. A review of thrust faulting in the Eastern Cape Fold Belt, South Africa, and the implications for current lithostratigraphic interpretation of the Cape Supergroup. Journal of African Earth Sciences, 34, 179-190.

Booth, P.W.K., Brunsdon, G. & Shone, R.W., 2004. A Duplex Model for the Eastern Cape Fold Belt? Evidence from the Palaeozoic Witterberg and Bokkeveld Groups (Cape Supergroup), Near Steytlerville, South Africa. Gondwana Research, 7 (1), 211-222.

Büttner, S.H., Reid, W.K. & Erasmus, R., 2016. Late Permian tectonics and fluid influx during the Cape Orogeny: evidence from fault-bound quartz veins in the Cape Supergroup, South Africa. South African Journal of Geology, 119 (2), 379-398.

Council for Geoscience, 1979. 1:250 000 Geological Series, 3322 Oudtshoorn. Council for Geoscience, Pretoria.

De Beer, C.H., 1992. Structural evolution of the Cape Fold Belt syntaxis and its influence on syntectonic sedimentation in the SW Karoo Basin. In: de Wit, M. J. & Ransome, I. G. D. (eds.), Inversion tectonics of the Cape Fold Belt, Karoo and Cretaceous Basins of South Africa. Rotterdam: Balkema, 197-206.

De Beer, C.H., 1995. Fold interference from simultaneous shortening in different directions: the Cape Fold Belt syntaxis. Journal of African Earth Sciences, 21, 157-169.

de Wit, M.J., Booth, P.W.K., Shone, R.W. & Bronn, P., 1998. A field guide through the Cape Fold Belt, Gondwana, Conference, University of Cape Town, Cape Town, 187pp.

Diamond, L.W., 2003. Glossary: Terms and symbols used in fluid inclusion studies. In Sampson, I., Anderson, A. & Marshall, D. (eds.), Fluid Inclusions: Analysis and Interpretation. Vancouver: Mineralogical Association of Canada, 365-374.

Fagareng, Å., 2012. A note on folding mechanisms in the Cape Fold Belt, South Africa. South African Journal of Geology, 115(2), 137-144.

Frimmel, H.E., Folling, P.G. & Diamond, R., 2001. Metamorphism of the Permo-Triassic Cape Fold Belt and its basement, South Africa. Mineralogy and Petrology, 73, 325-346.

Günther, D., Audétat, A., Frischknecht, R. & Heinrich, C.A., 1998. Quantitative analysis of major, minor and trace elements in fluid inclusions using laser ablation–inductively coupled plasma mass spectrometry. Journal of Analytical Atomic Spectrometry, 13, 263-270.

Hälbich, I.W., Fitch, F.J. & Miller, J.A., 1983. Dating the Cape orogeny. In: Söhnge, A. P. G. & Hälbich, I. W. (eds.), Geodynamics of the Cape Fold Belt. Special publication of the Geological Society of South Africa, 149-164.

Hansma, J., Tohver, E., Schrank, C., Jourdan, F., Adams, D., 2016. The timing of the Cape Orogeny: New $^{40}Ar/^{39}Ar$ age constraints on deformation and cooling of the Cape Fold Belt, South Africa. Gondwana Research, 32, 122-137.

Hobbs, B.E., Means, W.D., Williams, P.F., 1976. An Outline of Structural Geology. New York: John Wiley & Sons, 512pp.

Johnson, M.R., van Vuuren, C.J., Visser, J.N.J., Cole, D.I., Wickens, H.de V., Christie, A.D.M., Roberts, D.L. & Brandl, G., 2006. Sedimentary rocks of the Karoo Supergroup. In: Johnson, M.R. Anhaeusser C.R. & Thomas R.J (eds.) The Geology of South Africa. Geological Society of South Africa/Council for Geoscience, 461-499.

Lock, B.E., 1978. The Cape Fold Belt of South Africa; tectonic control of sedimentation. Preceedings of the Geologists' Association, 89(4), 263-281.

Mernagh, T.P. & Wilde, A.R., 1989. The use of the laser Raman microprobe for the determination of salinity in fluid inclusions. Geochimica et Cosmochimica Acta, 53, 765-771.

Newton, A.R., Shone, R.W. & Booth, P.W.K., 2006. The Cape Fold Belt. In: Johnson, M.R. Anhaeusser C.R. & Thomas R.J (eds.) The Geology of South Africa. Geological Society of South Africa/Council for Geoscience, 521-530.

Passchier, C.W., & Trouw, R.A.J., 1998. Microtectonics. Berlin:Springer, 287pp.

Paton, D.A., Macdonald, D.I.M. & Underhill, J.R., 2006. Applicability of thin or thick skinned structural models in a region of multiple inversion episodes; southern South Africa. Journal of Structural Geology, 28, 1933-1947.

Roedder, E., 1984. Fluid Inclusions. Washington, D.C.: Mineralogical Society of America, 644pp.

Schmidt-Mumm, A., 2008. Introduction to Fluid Inclusion Research, Short course handbook, Adalaide University, 57pp.

Seitz, J.C., Pasteris, J.D. and Chou, I.M., 1993. Raman spectroscopic characterization of gas mixtures. I. Quantitative composition and pressure determination of CH_4, N_2, and their mixtures. American Journal of Science, 293, 297-321.

Shelley, D., 1993. Igneous and metamorphic rocks under the microscope. London: Chapman & Hall, 446pp.

Shone, R.W. & Booth, P.W.K., 2005. The Cape Basin, South Africa: A review. Journal of African Earth Sciences, 43, 196-210.

Simpson, G.D.H., Thompson, A.B. & Connolly, J.A.D., 2000. Phase relations, singularities and thermobarometry of metamorphic assemblages containing phengite, chlorite, biotite and K-feldspar, quartz and H_2O. Contributions to Mineralogy and Petrology, 139, 555-569.

Tankard, A., Welsink, H., Aukes, P., Newton, A.R. & Stettler, E., 2009. Tectonic evolution of the Cape and Karoo basins of South Africa. Marine and Petroleum Geology, 26, 1379-1412.

Tankard, A.J., Jackson, M.P.A., Eriksson, K.A., Hobday, D.K., Hunter, D.R. & Minter, W.E.L., 1982. Crustal Evolution of Southern Africa: 3.8 Billion Years of Earth History. New York: Springer-Verlag, 523pp.

Thamm, A.G. & Johnson, M.R., 2006. The Cape Supergroup. In: Johnson, M.R. Anhaeusser C.R. & Thomas R.J (eds.) The Geology of South Africa. Geological Society of South Africa/Council for Geoscience, 443-460.

Theiu, V., Subramanian, S., Cologate, S.O. & Sloan, E.D, jr., 2000. High-pressure optical cell for hydrate measurements using Raman spectroscopy. In: Holder, G.D. and Bishnoi, P.R. (eds.) 2000. Gas Hydrates Challenges for the Future. New York Academy of Sciences, 912, 983-992.

Thomas, R.J., von Veh, M.W. & McCourt, S., 1993. The tectonic evolution of southern Africa: an overview. Journal of African Earth Sciences, 16, 5-24.

Vernon, R.H., 2004. A Practical Guide to Rock Microstructure. Cambridge: Cambridge University Press, 594pp.

Voll, G., 1976. Recrystallisation of quartz, biotite and feldspars from Erstfeld to the Leventina Nappe, Swiss Alps, and its geological significance. Schweizerische Mineralogische und Petrographische Mitteilungen, 56, 641-647.

Watkeys, M.K., 2006. The break-up of Gondwana: A South African perspective. In: Johnson, M.R. Anhaeusser C. R. & Thomas R.J (eds.) The Geology of South Africa. Geological Society of South Africa/Council for Geoscience, 531-539.

APPENDIX A: SUMMARY OF FINAL MELTING TEMPERATURES

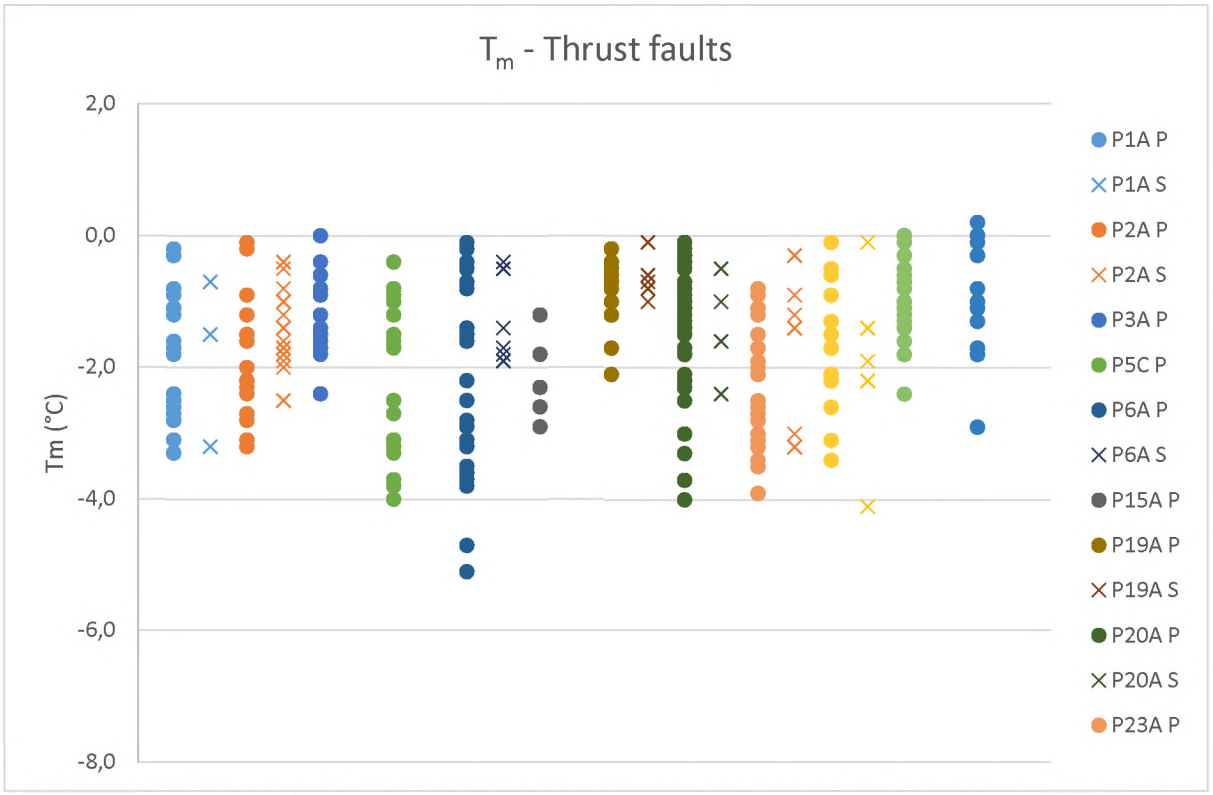

***Figure A1**: Temperature of final melting in primary (P) and secondary (S) fluids from thrust fault samples.*

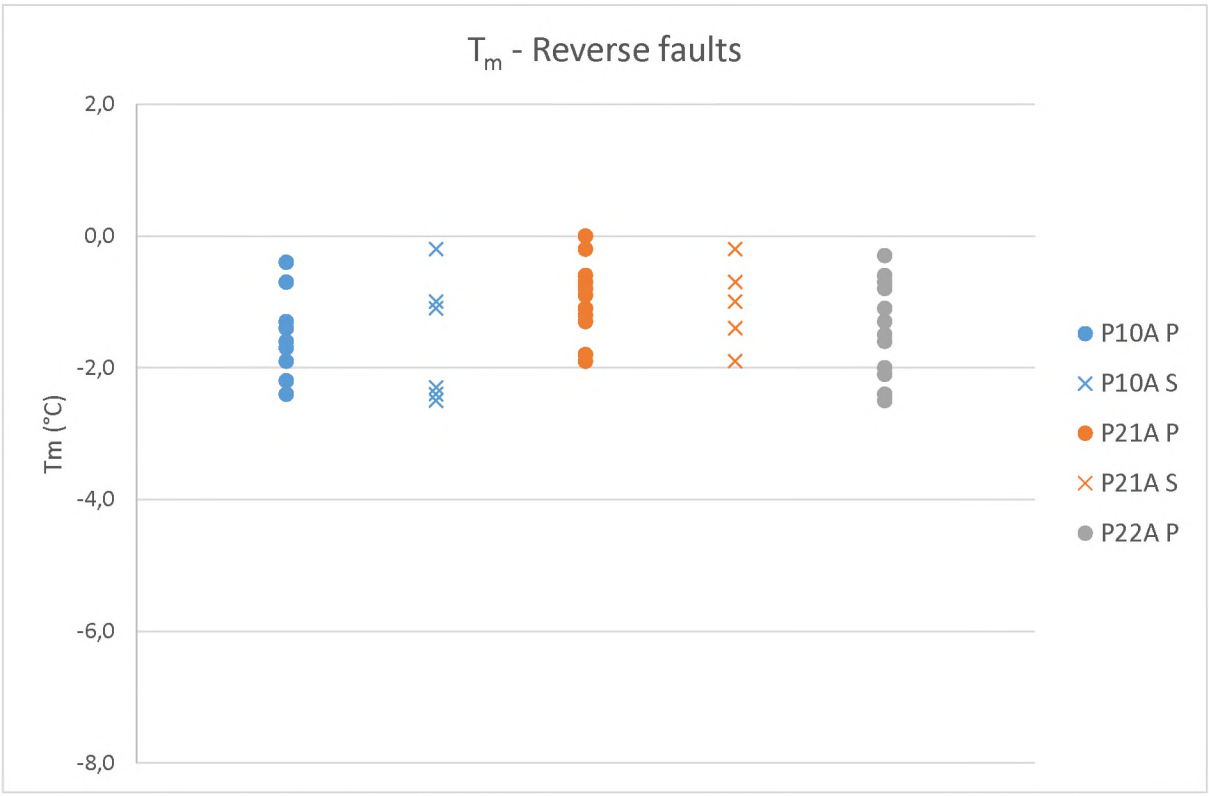

***Figure A2**: Temperature of final melting in primary (P) and secondary (S) fluids from reverse fault samples.*

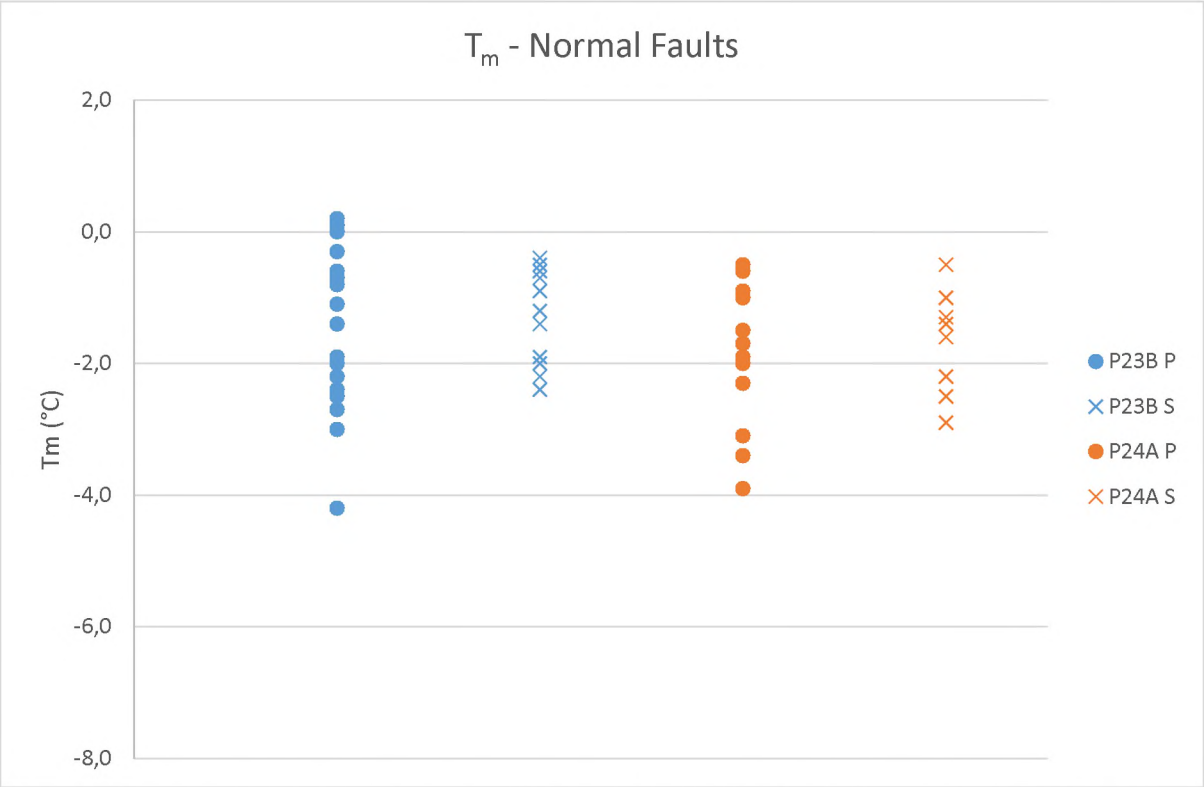

***Figure A3**: Temperature of final melting in primary (P) and secondary (S) fluids from normal fault samples.*

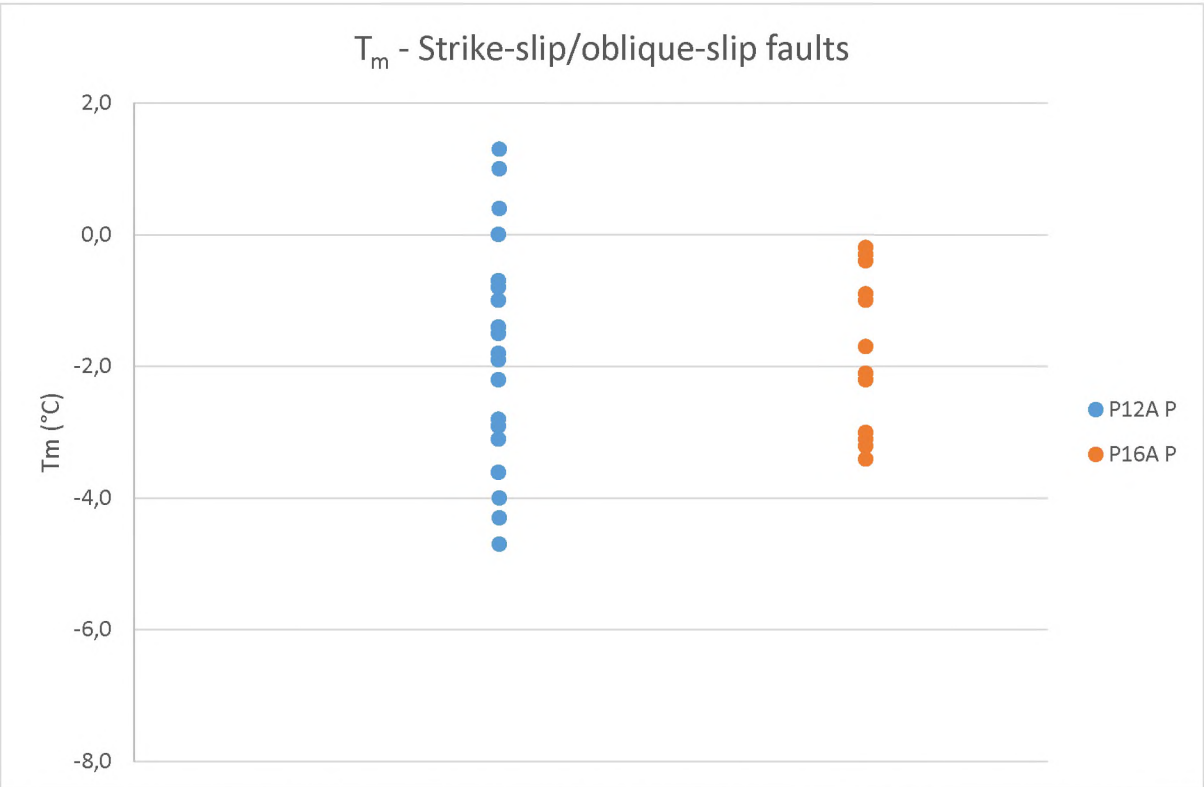

***Figure A4**: Temperature of final melting in primary (P) fluids from oblique- and strike-slip samples fault samples.*

***Figure A5**: Temperature of final melting in primary (P) and secondary (S) fluids from tension gash samples.*

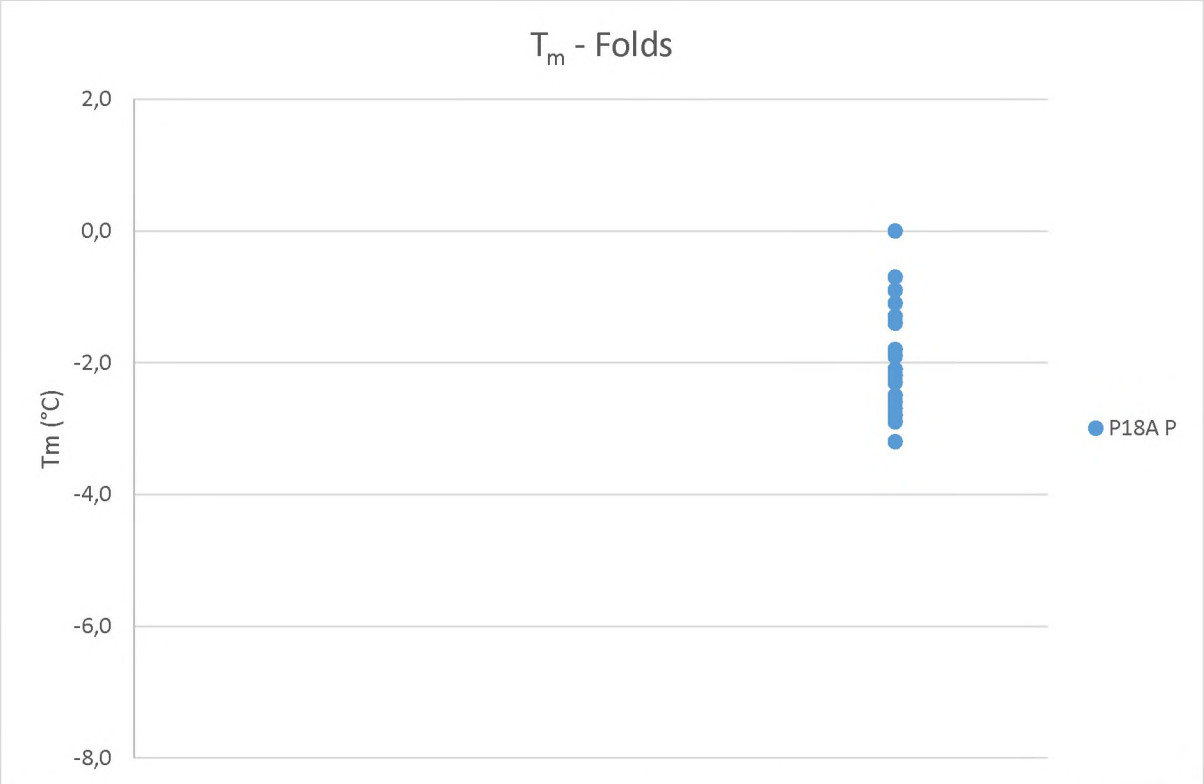

***Figure A6**: Temperature of final melting in primary (P) fluids from fold samples.*

APPENDIX B: SUMMARY OF HOMOGENISATION TEMPERATURES

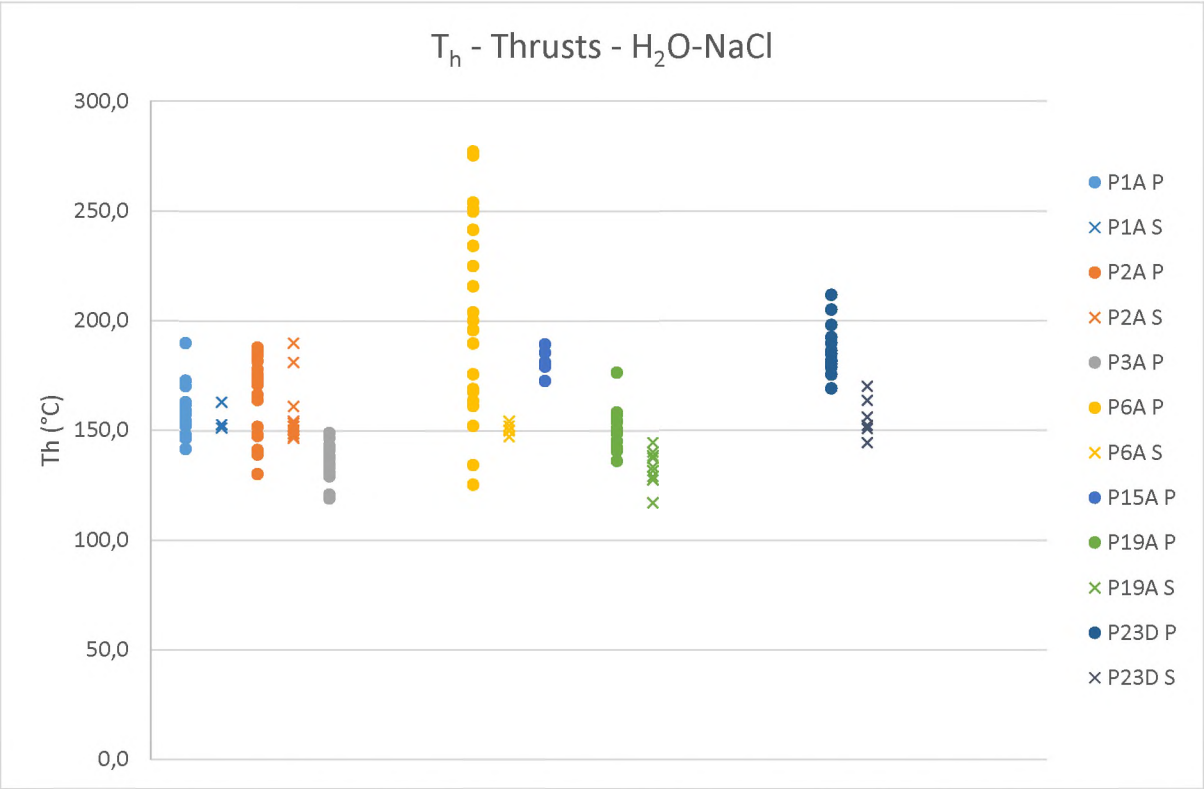

***Figure B1**: Temperature of homogenisation in primary (P) and secondary (S) H_2O-NaCl fluids from thrust fault samples.*

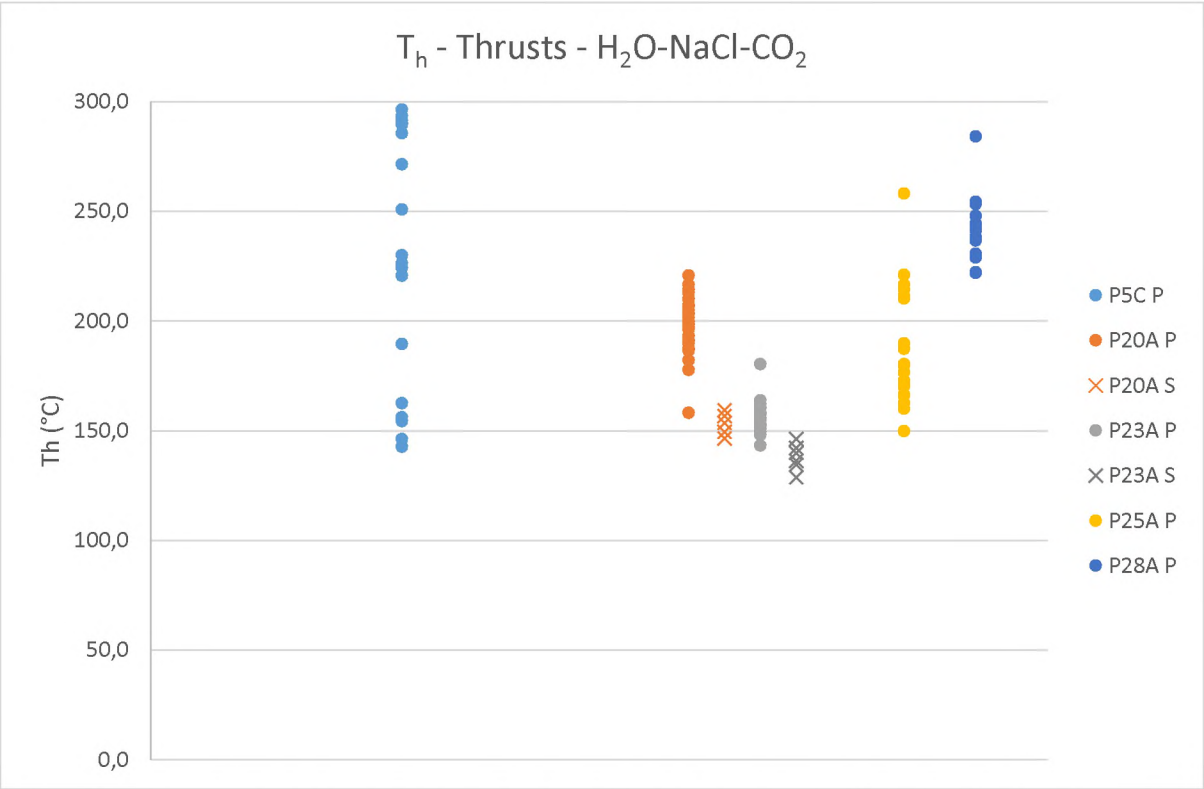

***Figure B2**: Temperature of homogenisation in primary (P) and secondary (S) H_2O-NaCl-CO_2 fluids from thrust fault samples.*

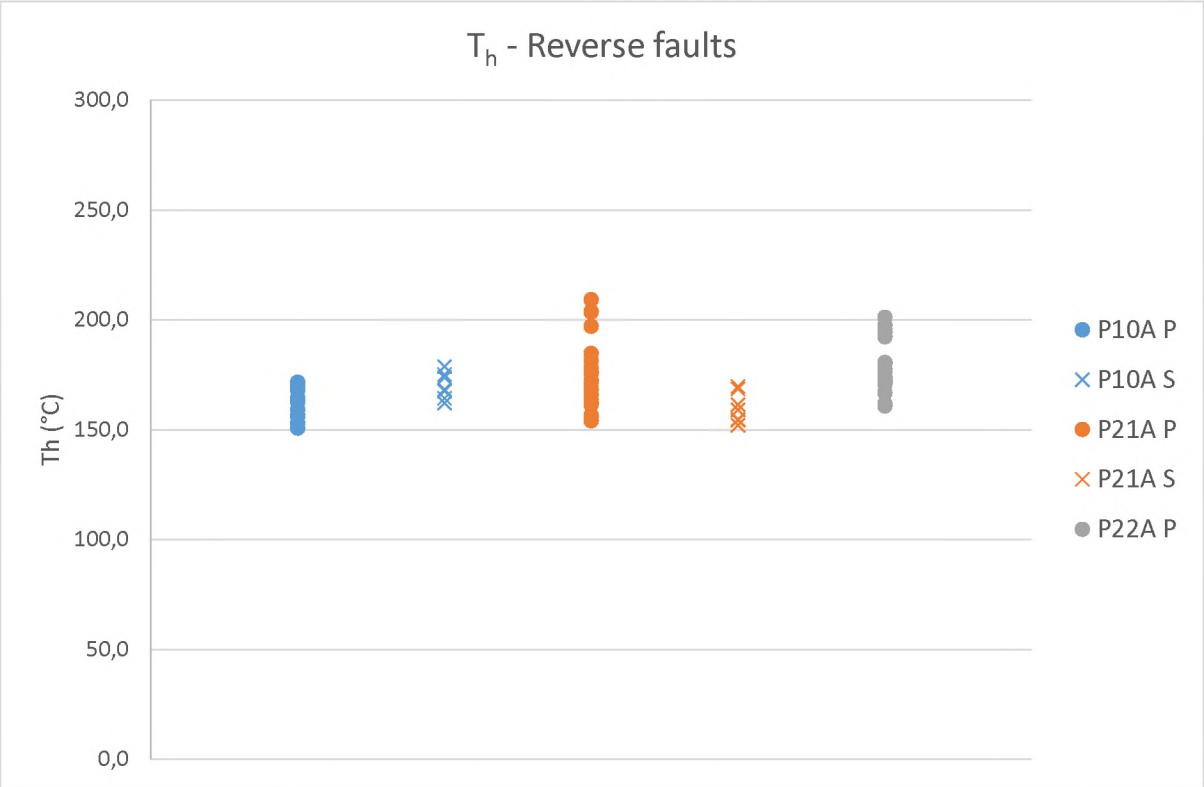

***Figure B3**: Temperature of homogenisation in primary (P) and secondary (S) fluids from reverse fault samples.*

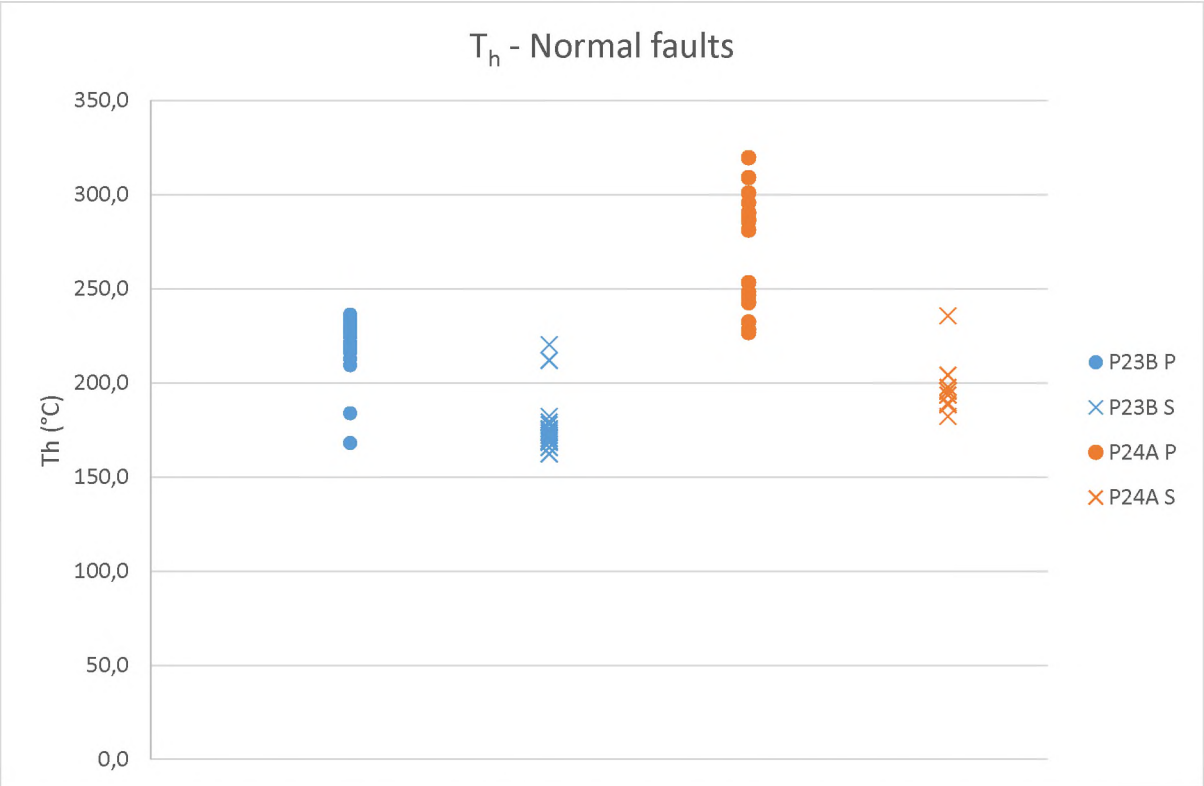

***Figure B4**: Temperature of homogenisation in primary (P) and secondary (S) fluids from normal fault samples.*

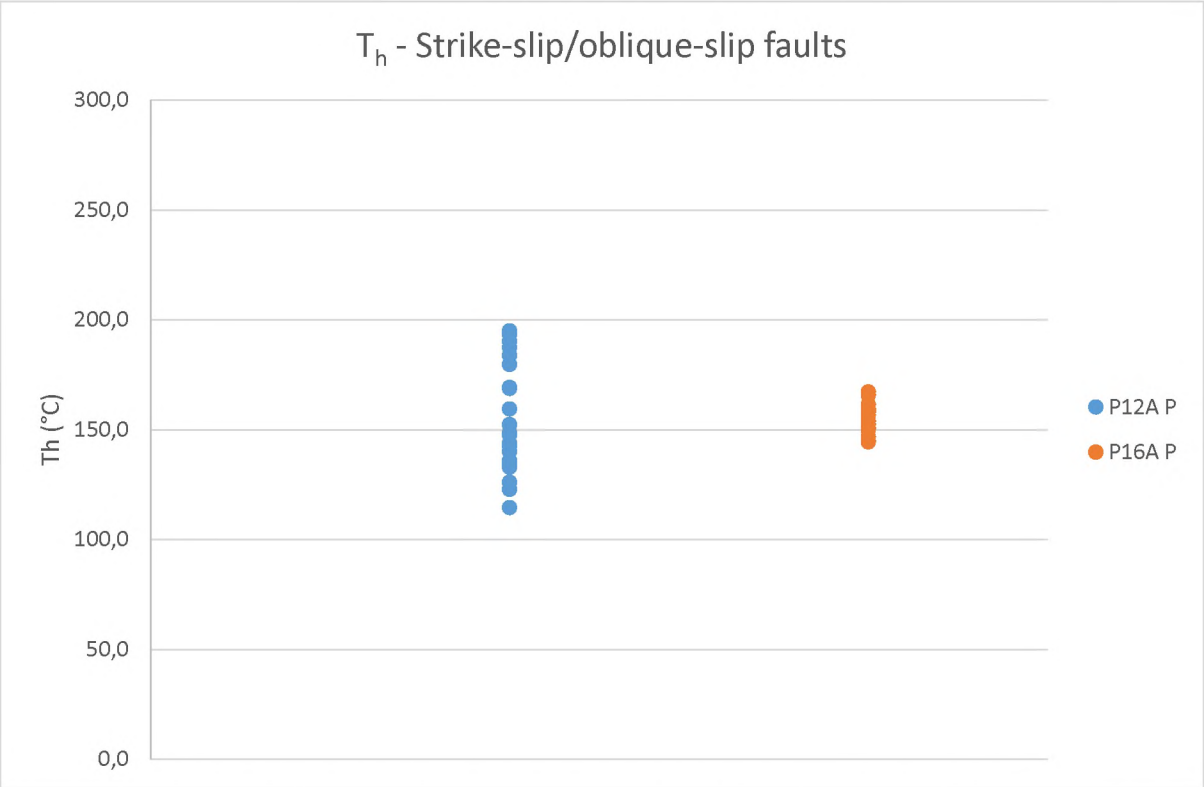

***Figure B5**: Temperature of homogenisation in primary (P) fluids from oblique- and strike-slip fault samples.*

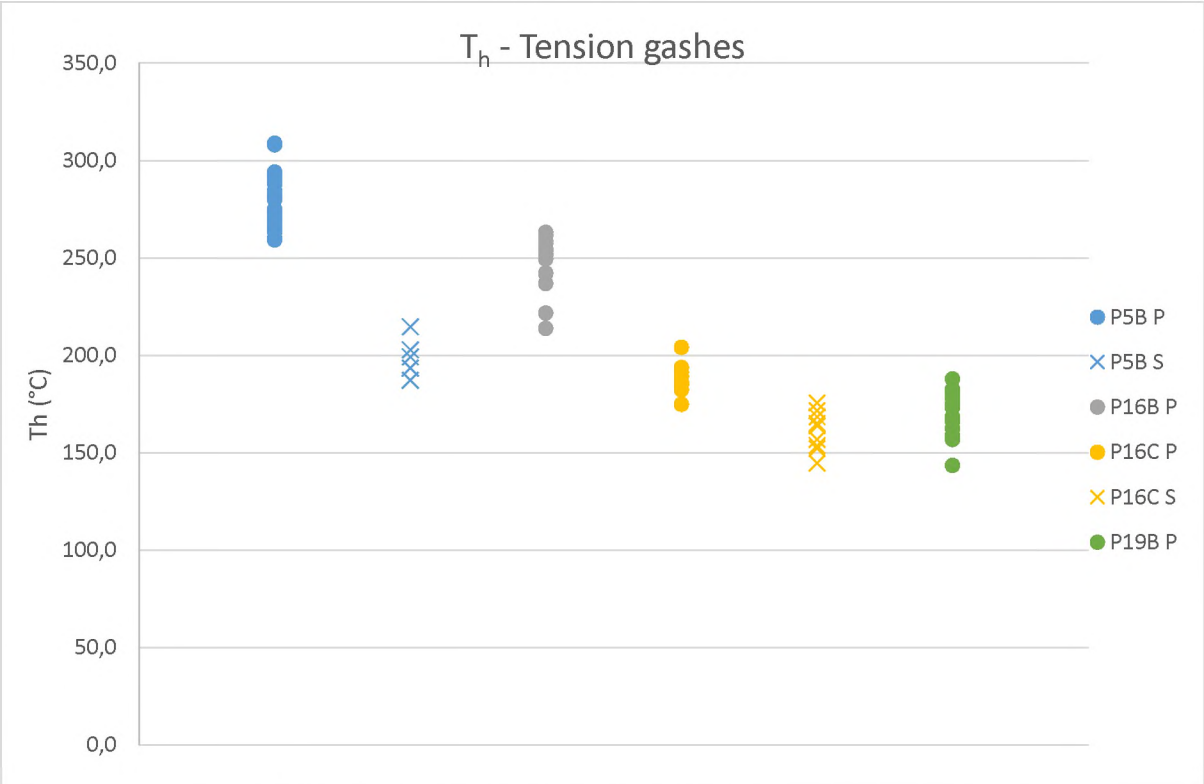

***Figure B6**: Temperature of homogenisation in primary (P) and secondary (S) fluids from tension gash samples.*

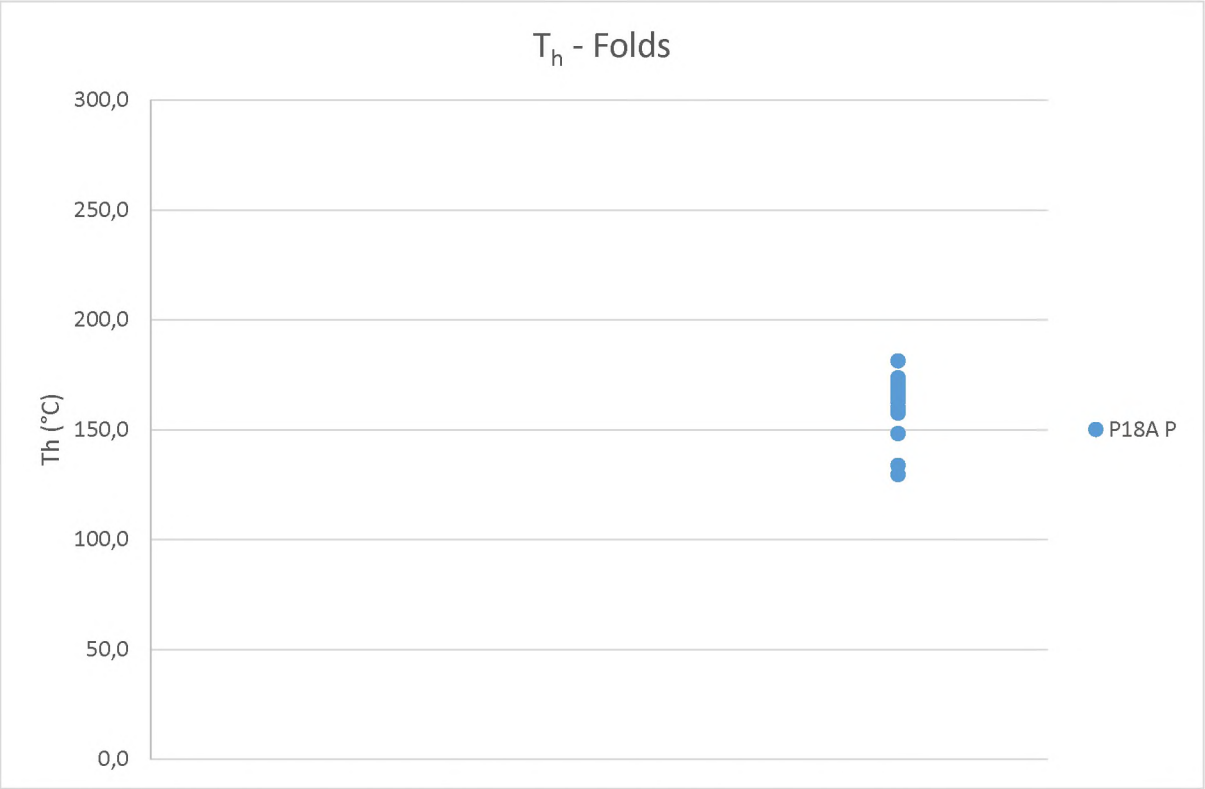

***Figure B7**: Temperature of homogenisation in primary (P) fluids from fold samples.*

APPENDIX C: SUMMARY OF MICROTHERMOMETRY RESULTS FOR PRIMARY FLUIDS

Table C1: Summary of microthermometry results for primary fluids in each structure. Average values are given in brackets.

		Fluid	Thrusts	Reverse	Normal	Strike-slip	Tension gashes	Folds
T_h (°C)	According to heating experiments	H_2O-NaCl	130-190 (160)	150-210 (173)	No FIs	No FIs	155-195 (176) & 235-265 (250)	150-180 (162)
		H_2O-NaCl-CO_2	140-240 (198)	No FIs	No FIs	130-170 (155)	No FIs	No FIs
		H_2O-NaCl-CO_2-CH_4	No FIs	No FIs	210-250 (229) & 280-300 (290)	No FIs	260-290 (277)	No FIs
Salinity (wt% NaCl equivalent)	According to equation 1	H_2O-NaCl	≤6 (2,8)	≤4 (2,3)	No FIs	No FIs	≤4 (2,0)	≤5 (3,4)
		H_2O-NaCl-CO_2	≤6 (2,7)	No FIs	No FIs	≤6 (3,3)	No FIs	No FIs
		H_2O-NaCl-CO_2-CH_4	No FIs	No FIs	≤6 (2,7)	No FIs	≤6 (2,5)	No FIs
H_2O Density (g/cm3)	According to FLUIDS (Bakker, 2003)	H_2O-NaCl	0,87-0,97 (0,92)	0,85-0,95 (0,92)	No FIs	No FIs	0,75-0,85 (0,82) & 0,85-0,95 (0,9)	0,87-0,95 (0,94)
		H_2O-NaCl-CO_2	NA	No FIs	No FIs	0,9-0,97 (0,95)	No FIs	No FIs
		H_2O-NaCl-CO_2-CH_4	No FIs	No FIs	0,7-0,8 (0,75) & 0,78-0,9 (0,85)	No FIs	0,78-0,85 (0,83)	No FIs
CO_2 Density (g/cm3)	According to pressure contours for CO_2 in low T range	H_2O-NaCl	NA	NA	NA	NA	NA	NA
		H_2O-NaCl-CO_2	0,79-0,93 (0,88)	No FIs	No FIs	0,82-0,86 (0,84)	No FIs	No FIs
		H_2O-NaCl-CO_2-CH_4	No FIs	No FIs	0,82-0,85 (0,84)	No FIs	0,82-0,86 (0,82)	No FIs
Pressure of trapping (MPa)	According to isochore diagrams	H_2O-NaCl	~175	~175	No FIs	No FIs	~170	>300
		H_2O-NaCl-CO_2		No FIs	No FIs	~135-142		No FIs
		H_2O-NaCl-CO_2-CH_4	No FIs	No FIs	~150-190	No FIs		No FIs
	According to CO_2 pressure contours	H_2O-NaCl	NA	NA	No FIs	No FIs	NA	NA
		H_2O-NaCl-CO_2	~170	No FIs	No FIs	~100	No FIs	No FIs
		H_2O-NaCl-CO_2-CH_4	No FIs	NA	~170	No FIs	~160	No FIs
	According to CH_4 peak position	H_2O-NaCl	NA	NA	NA	NA	NA	NA
		H_2O-NaCl-CO_2	NA	NA	NA	NA	NA	No FIs
		H_2O-NaCl-CO_2-CH_4	No FIs	No FIs	33	No FIs	47	No FIs
Temperature of trapping (T_T;°C)	According to isochore diagrams	H_2O-NaCl	~300	~300	No FIs	No FIs	~270	>220
		H_2O-NaCl-CO_2		No FIs	No FIs	~250-260		No FIs
		H_2O-NaCl-CO_2-CH_4	No FIs	No FIs	~260-300	No FIs		No FIs

APPENDIX D: SUMMARY OF MICROTHERMOMETRY RESULTS FOR PRIMARY FLUIDS

***Table D1**: Summary of microthermometry results for secondary fluids in each structure. Average values are given in brackets.*

		Fluid	Thrusts	Reverse	Normal	Strike-slip	Tension gashes	Folds
T_h (°C)	According to heating experiments	H_2O-NaCl	145-170 (152)	160-180 (171)	No FIs	No FIs	150-175 (162,0)	No FIs
		H_2O-NaCl-CO_2	No FIs	150-170 (160)	No FIs	No FIs	180-220 (200,0)	No FIs
		H_2O-NaCl-CO_2-CH_4	No FIs	No FIs	160-200 (184)	No FIs	No FIs	No FIs
Salinity (wt% NaCl equivalent)	According to equation	H_2O-NaCl	≤5 (2,2)	≤4 (2,9)	No FIs	No FIs	≤2,5 (1,1)	No FIs
		H_2O-NaCl-CO_2	≤5 (2,6)	≤3 (1,8)	No FIs	No FIs	≤3,5 (2,1)	No FIs
		H_2O-NaCl-CO_2-CH_4	No FIs	No FIs	≤5 (2,1)	No FIs	No FIs	No FIs
H_2O Density (g/cm3)	According to FLUIDS (Bakker, 2003)	H_2O-NaCl	0,9-0,95 (0,94)	0,9-0,93 (0,92)	No FIs	No FIs	0,9-0,93 (0,92)	No FIs
		H_2O-NaCl-CO_2	0,94	0,9-0,93 (0,91)	No FIs	No FIs	0,94	No FIs
		H_2O-NaCl-CO_2-CH_4	No FIs	No FIs	0,86-0,95 (0,9)	No FIs	No FIs	No FIs
CO_2 Density (g/cm3)	According to pressure contours for CO_2 in low T range	H_2O-NaCl	NA	NA	NA	NA	NA	NA
		H_2O-NaCl-CO_2	0,95	0,81-0,85 (0,83)	No FIs	No FIs	0,83-0,85 (0,84)	No FIs
		H_2O-NaCl-CO_2-CH_4	No FIs	No FIs	0,83-0,87 (0,85)	No FIs	No FIs	No FIs
Pressure of trapping (MPa)	According to isochore diagrams	H_2O-NaCl	~105	100-170 (120)	No FIs	No FIs	~160	No FIs
		H_2O-NaCl-CO_2			No FIs	No FIs		No FIs
		H_2O-NaCl-CO_2-CH_4	No FIs	No FIs	~100	No FIs	No FIs	No FIs
	According to CO_2 pressure contours	H_2O-NaCl	NA	NA	No FIs	No FIs	NA	No FIs
		H_2O-NaCl-CO_2	~120	90	No FIs	No FIs	~130	No FIs
		H_2O-NaCl-CO_2-CH_4	No FIs	No FIs	140	No FIs	No FIs	No FIs
	According to CH4 peak position	H_2O-NaCl	NA	NA	No FIs	No FIs	NA	No FIs
		H_2O-NaCl-CO_2	NA	NA	No FIs	No FIs	NA	No FIs
		H_2O-NaCl-CO_2-CH_4	No FIs	No FIs	66	No FIs	No FIs	No FIs
Temperature of trapping (T_T;°C)	According to isochore diagrams	H_2O-NaCl	~230	180-260 (210)	No FIs	No FIs	~280	No FIs
		H_2O-NaCl-CO_2			No FIs	No FIs		No FIs
		H_2O-NaCl-CO_2-CH_4	No FIs	No FIs	~180	No FIs	No FIs	No FIs

APPENDIX E: SUMMARY OF ANALYSED SAMPLES

***Table E1**: Summary of analysed samples, showing the location (transect), the structural setting of the sample, and the formation the sample was taken from. The orientation of the fault surface and lineations are given where applicable.*

Transect	Sample	Structural Setting	Formation	Fault surface orientation	Lineation
Outeniqua Range	P1A	Thrust	Peninsula	220/14; 210/15	194/15; 210/14
	P2A	Thrust	Peninsula	195/41; 194/24	174/38; 200/23
	P3A	Thrust	Peninsula	185/35; 208/30	212/32; 201/30
	P5B	Tension Gash	Tchando	NA	
	P5C	Thrust	Tchando	188/36	210/32
	P6A	Thrust	Peninsula	179/49	232/30
De Vlugt to Uniondale	P10A	Reverse Fault	Kouga	021/59; 022/52; 021/56	028/52; 011/54
	P12A	Strike-slip/oblique slip fault	Baviaanskloof	152/47	239/15
	P15A	Thrust	Kouga	166/30	210/24
	P16A	Thrust	Kouga	174/27	215/21
	P16B	Tension Gash	Kouga	NA	NA
	P16C	Tension Gash	Kouga	NA	NA
Meiringspoort	P18A	Folded vein (hinge)	Weltevrede	NA	NA
	P19A	Thrust	Boplaas	155/18	177/16
	P19B	Tension Gash	Boplaas	NA	
	P20A	Thrust		238/17	234/17 (~dip-slip)
	P21A	Reverse Fault	Kango inlier phyllites	NA	
	P22A	Reverse Fault	Peninsula	014/70	042/66
	P23A (i)	Thrust	Peninsula	066/10	023/09
	P23B (ii)	Normal Fault	Peninsula	184/70; 188/84;	184/70 (dip slip); 190/83
	P23D (iii)	Thrust	Peninsula	sub-horizontal	026/05; 024/11; 020/15
	P24A	Normal Fault	Peninsula	186/70	224/66
	P25A	Thrust	Tchando	220/08	189/03
Swartberg Pass	P28A	Thrust	Tchando	107/25; 132/17	167/10; 162/10